Energy Island North Sea

Metocean Assessment

Part C: Data Analyses – Wind Farm Area

Metocean site conditions for FEED of the offshore wind farms

Report
IO number: 4500087261

2023-08-09

Prepared for Energinet Eltransmission A/S

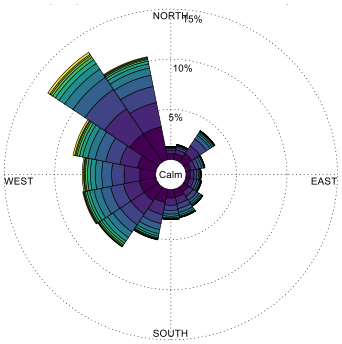

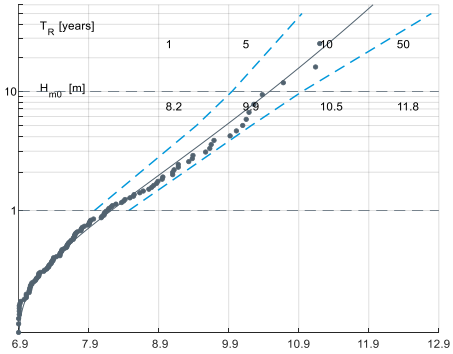

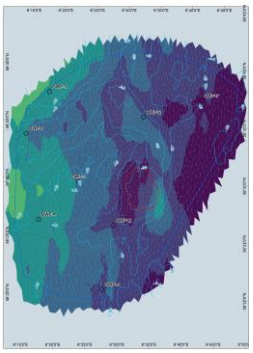

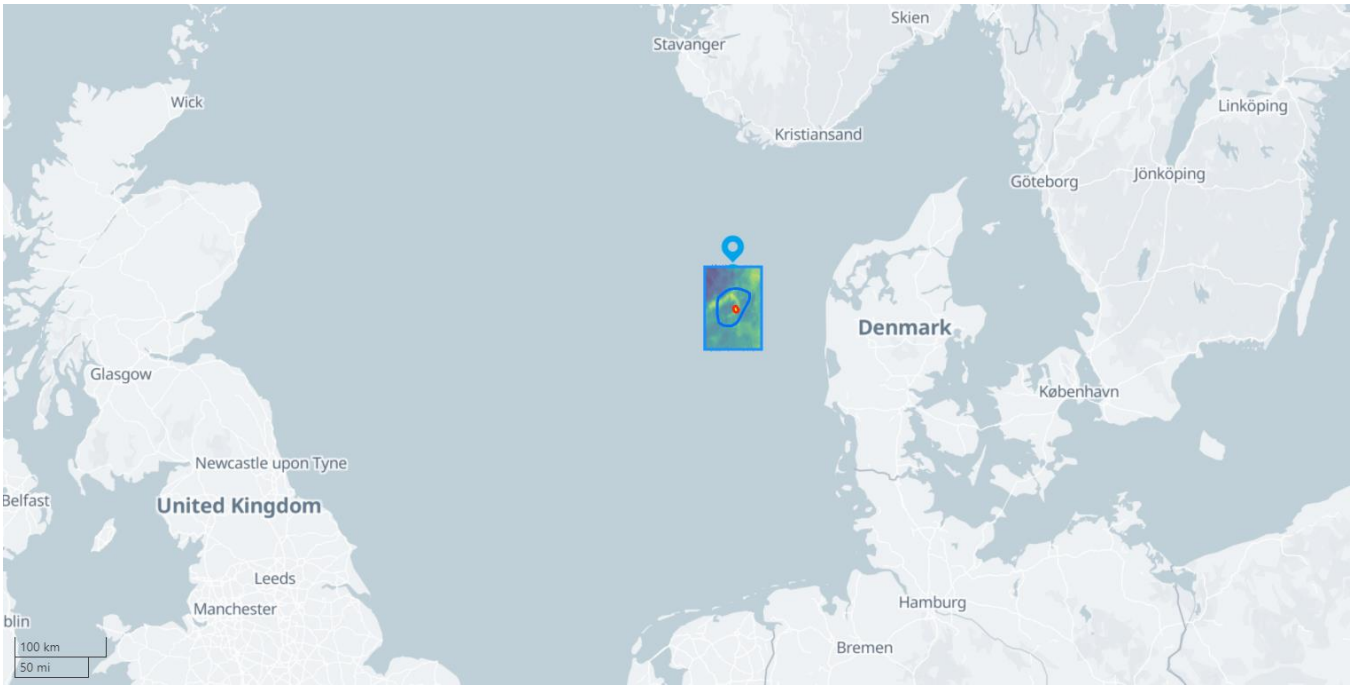

Energy Island North Sea

Metocean Assessment
Part C: Data Analyses – Wind Farm Area
Metocean site conditions for FEED of the offshore wind farms

Report
IO number: 4500087261

Prepared for: Energinet Eltransmission A/S
Represented by Mr Kim Parsberg Jakobsen

Contact person: Patrick Dich Grode, pdg@dhihroup.com, +45 4516 9070
Project Manager: Patrick Dich Grode
Quality Supervisor: Ameya Sathe
Author: Patrick Dich Grode

Project No.: 11828428
Approved by: Jesper Ulrik Fuchs

Revision:	Date:	Description:
1.2	2023-08-09	Final report including final comments from the certifier. Appendix A attachments removed and provided as separate files.
1.1	2023-07-17	Final report including final comments from the certifier.
1.0	2023-07-13	Final report including final comments from client and certifier.
0.2	2023-06-30	Revised draft report including comments from client and certifier.
0.1	2023-04-27	Draft report issued for comments by client and certifier.

Classification: Confidential
File name: 11828428_DHI_EINS_Metocean_Part_C_Analyses_OWFs

DHI A/S • Agern Allé 5 • • DK-2970 Hørsholm • Denmark
Telephone: +45 4516 9200 • dhi@dhigroup.com • www.dhigroup.com • Company Reg. No.: 36466871

Contents

Nomenclature

Variable	Abbrev.	Unit
Atmosphere		
Wind speed @ 10 m height	WS_{10}	m/s
Wind direction @ 10 m height	WD_{10}	°N (clockwise from)
Air pressure @ mean sea level	P_{MSL}	hPa
Air temperature @ 2 m height	$T_{air,2m}$	°C
Relative humidity @ 2 m height	RH_{2m}	-
Downward solar radiation flux	SR	W/m^2
Ocean		
Water level	WL	mMSL
Current speed	CS	m/s
Current direction	CD	°N (clockwise to)
Water temperature	T_{water}	°C
Water Salinity	Salinity	-
Water density	ρ_{water}	Kg/m^3
Waves		
Significant wave height	H_{m0}	m
Peak wave period	T_p	s
Mean wave period	T_{01}	s
Zero-crossing wave period	T_{02}	s
Peak wave direction	PWD	°N (clockwise from)
Mean wave direction	MWD	°N (clockwise from)
Direction standard deviation	DSD	°

Executive Summary

Energinet Eltransmission A/S (Energinet) requested a metocean site conditions assessment to form part of the site conditions and to serve as the basis for the design of the Energy Island North Sea (EINS).

This study provides detailed metocean conditions for EINS and establishes a metocean database for the energy island and the related offshore wind farm (OWF) area development area around the island as shown in Figure 0.1.

Table 0.1 provides a summary of metocean guidelines, EVA methodology, and analyses of Part B (island area), and **Part C (OWF area, this report)**.

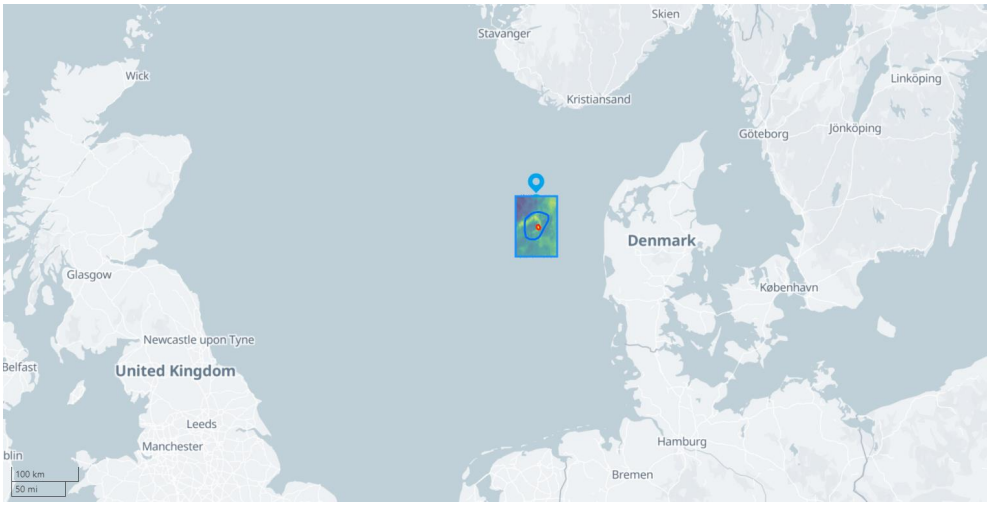

Figure 0.1 Location of the Energy Island North Sea, the related offshore wind farm development area, and measurement stations
The hindcast database (light blue polygon) entails: Waves: EINS-SW-CFSR, Ocean: EINS-SW-CFSR, Atmosphere: Global-AT-CFSR.

Table 0.1 Summary of metocean guidelines, EVA methodology, and analyses
Analyses concern normal and extreme conditions included at each analysis point. The Part A report, [1], forms the data basis for Part B (Island) and Part C (OWF) analysis reports.

Subject	**Part B (Island)** Points: EINS-1-5	**Part C (OWF)** Points: OWF-1-8
Extremes - methodology	J-EVA (directional)	T-EVA (omni only)
Analyses - Wind	✓	÷
Analyses - Water Level	✓	✓
Analyses - Current	✓	✓
Analyses - Waves	✓	✓
Wind-Wave misalignment	✓	✓
Other Metocean Conditions	✓	✓

Summary of data basis, Part A, [1]

All metocean hindcast model data covered the period 1979-01-01 to 2022-10-01 (43+ years) at 30-min interval. Wind and other atmospheric data were adopted from CFSR (rainfall data from ERA5), while a local hindcast 2D hydrodynamic model, HD_{EINS}, was set up to simulate water levels and currents, and a dedicated spectral wave model SW_{EINS}, was set up to simulate waves. 3D currents, water temperature and salinity were adopted from the DHI United Kingdom and North Sea 3-dimensional (HD_{UKNS3D}) hydrodynamic model.

The hindcast data was compared to a comprehensive set of local wind, water level, current, wave and CTD (sea temperature and salinity) measurements (2021-11-15 to 2022-11-15.) supplemented by long-term measurements from other stations in the North Sea and found to be accurate and applicable for assessments of normal and extreme metocean conditions at EINS.

Recommendations for wind profiles/averaging, current profiles, and short-term wave distributions were established based on the local measurements.

Sea level rise (SLR) was estimated at +0.8 m by the year 2113 (end of lifetime). It is recommended that designers consult Energinet for any given design requirements, to decide on the safety policy and procedure with respect to relevant climate change effects. A (potentially conservative) guideline on climate change effects on wind and waves is suggested in NORSOK, [2].

The metocean hindcast data developed for EINS covers the entire light blue polygon in Figure 0.1. It entailed all hindcast wave, ocean, and atmospheric variables and was provided to Energinet on a hard disk in MIKE dfs file formats. The dfs files can be read using either the Python MikeIO[1] or the DHI-MATLAB-Toolbox[2] open source libraries available at GitHub.

Normal conditions

At the EINS OWF area the mean wind speed is 8.8 m/ s and mean significant wave height is 1.9 – 2.0 m (see Figure 0.3) with peak wave periods most frequently between 4 – 8 s. The wave conditions are characterized by a mix of swell from the North Atlantic and local wind-sea predominantly from the west, with a dominance of extremes from the northwest, see Figure 0.2.

The tides are weak at OWF-3 with HAT = +0.35 mMSL and LAT = -0.30 mMSL, giving a total tidal envelope of 0.65 m. The highest and lowest total water levels in the hindcast period are +1.5 mMSL and -1.1 mMSL and occur during winter (Nov. – Feb.). The mean total current speed is 0.15 m/s dominated by residual (especially during extreme events).

[1] https://github.com/DHI/mikeio
[2] https://github.com/DHI/DHI-MATLAB-Toolbox

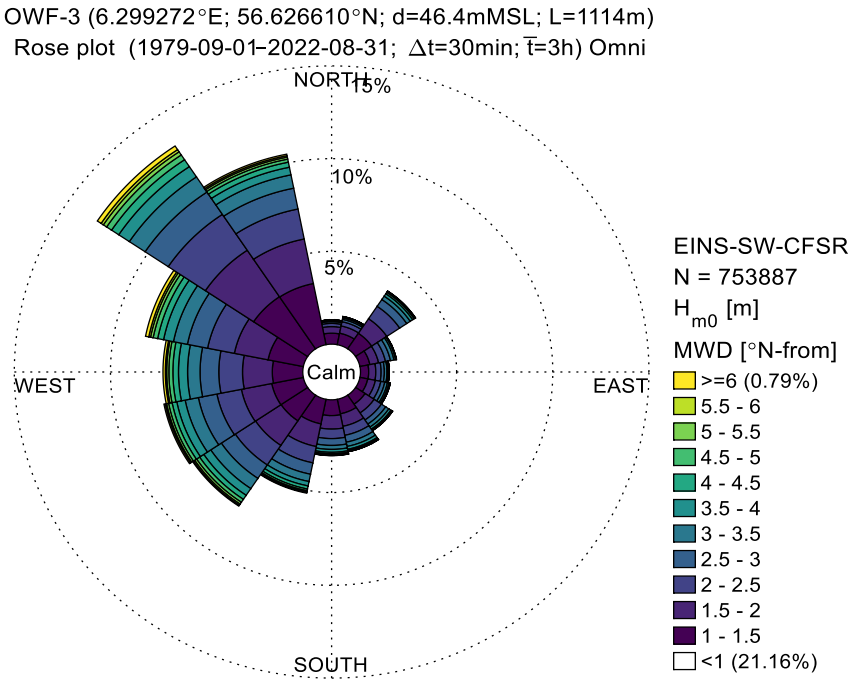

Figure 0.2 Wave rose at OWF-3

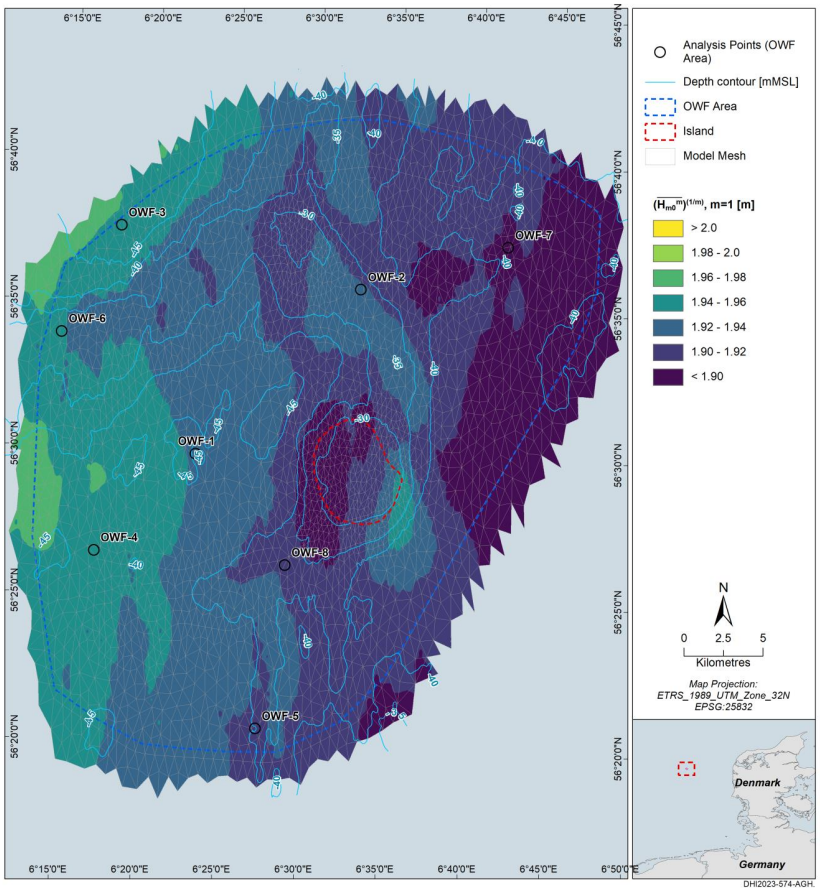

Figure 0.3 Spatial variation of $\overline{H_{m0}}$ across EINS OWF area

Extreme conditions

Extreme metocean conditions were established using Traditional Extreme Value Analysis (T-EVA) following the methodology and settings derived and described in Appendix B: Sensitivity of T-EVA to Distribution, Threshold, and Fitting.

The extreme values of the EINS OWF area are given for return periods of 1, 5, 10, and 50 years for waves (H_{m0}, H_{max}, and C_{max} including conditioned/joint variables), water level and currents at eight (8) analysis points (see Figure 2.1). Table 0.2 presents a summary of the 50-year omni-extreme values at all analysis points.

The water depth at the analysis points varies within 32 – 46 mMSL, which at the shallowest locations impacts (reduces) the wave heights.

The 50-year significant wave height, $H_{m0,50yr}$, varies within 10.9 – 11.9 m at the analysis points. The maximum wave height, H_{max}, is a factor 1.8 - 1.9 times H_{m0}, depending on local water depth. The 50-year maximum wave crest with respect to MSL (i.e., convoluted with the simultaneous water level), $C_{max,MSL}$, varies within 14.9 – 16.7 mMSL (note that higher H_{m0} occurs at other locations within the EINS OWF area, see maps in Section 6.2.5).

The 50-year total high and low water levels, HWL_{tot} and $LWL_{tot,}$ are within +1.9 mMSL and -1.2 mMSL, and the 50-year depth-averaged total current speed, $CS_{tot,50yr}$, varies within 0.9 – 1.1 m/s across the analysis points (note that higher CS occurs at other locations within the EINS OWF area, see maps in Section 5.2.3).

Table 0.2 Summary of the 50-year omni-extreme values at all analysis points

Results at OWF-3 are presented in the main body of this report, while results at all analysis points are given in the data reports attached to this report, see Appendix A: List of Data Reports.

Variable		50-year omni-extreme values at all analysis points							
Abbrev.	Unit	OWF-1	OWF-2	OWF-3	OWF-4	OWF-5	OWF-6	OWF-7	OWF-8
d	mMSL	45.1	32.2	46.4	42.5	39.7	32.7	40.1	36.9
HWL_{tot}	mMSL	1.77	1.74	1.67	1.78	1.87	1.71	1.77	1.83
LWL_{tot}	mMSL	-1.19	-1.16	-1.13	-1.19	1.23	-1.15	-1.17	-1.21
CS_{tot}	m/s	0.9	1.1	1.0	0.9	0.9	1.1	1.0	1.0
H_{m0}	m	11.2	11.9	11.8	11.2	10.9	11.6	10.9	10.9
$T_p\|H_{m0}$	s	15.8	16.4	16.2	16.0	15.5	16.5	15.7	15.6
H_{max}	m	21.2	21.2	22.4	21.0	20.5	21.0	20.7	20.4
T_{Hmax}	s	14.2	14.8	14.6	14.4	13.9	14.8	14.1	14.0
$C_{max,SWL}$	mSWL	13.6	15.5	14.4	13.7	13.5	15.0	13.5	13.7
$C_{max,MSL}$	mMSL	15.1	16.7	15.6	15.1	14.9	16.3	14.6	15.1

1 Introduction

This study provides detailed metocean conditions for the Energy Island North Sea (EINS) and establishes a metocean database for the island and the adjacent offshore wind farm (OWF) development area (see Figure 1.1).

Energinet Eltransmission A/S (Energinet) was instructed by the Danish Energy Agency (DEA) to initiate site investigations, including a metocean conditions assessment, to form part of the site conditions assessment and to serve as the basis for the design and construction of EINS and related OWF's. The study includes an assessment of climate change considering an 80-year lifetime.

Energinet commissioned DHI A/S (DHI) to provide this study with Scope of Work (SoW) defined in [3]. Later, the work was extended to cover also FEED level metocean conditions for the offshore wind farm area cf. scope in [4]. The study refers to the following common practices and guidelines:

- DNV-RP-C205, [5]
- IEC 61400-3-1, [6]

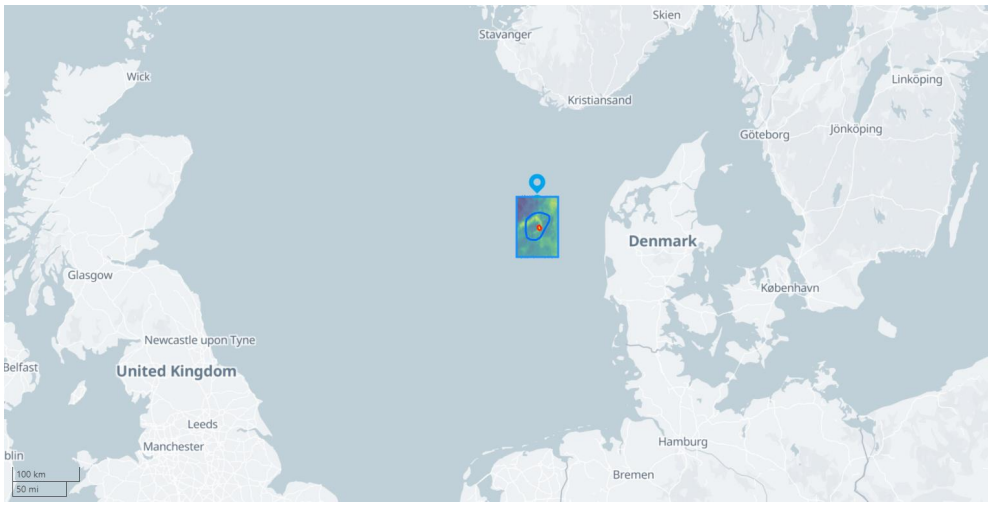

Figure 1.1 The location of the Energy Island North Sea (red dot), and related offshore wind farm development area (dark blue)
The hindcast database (light blue polygon) entails: Waves: *EINS-SW-CFSR*, Ocean: *EINS-SW-CFSR*, Atmosphere: *Global-AT-CFSR*.

The deliverables included time series data of hindcast metocean parameters, normal, extreme, and joint analyses at five (5) and eight (8) locations within the EINS and OWF areas respectively, a metocean database (see Figure 1.1), and four (4) separate reports:

- **Part A: Data Basis – Measurements and Models, [1]**
  Establishment of bathymetry, measurements and hindcast metocean data.
- **Part B: Data Analyses – Energy Island, [7]**
  Metocean site conditions for detailed design of the energy island.
- **Part C: Data Analyses – Wind Farm Area, [8]** (this report)
  FEED level metocean site conditions for the offshore wind farm area.
- **Part D: Data Basis – Hindcast Revalidation Note**, [9]

  Revalidation of the hindcast metocean data vs. extended measurements.

2 Analysis Points

This section presents the OWF points selected for analysis.

Figure 2.1 shows a map of the eight (8) analysis points and Table 2.1 presents the coordinates and water depths of the analysis points.

The analysis points were defined by Energinet considering the anticipated locations of the wind farms, and the spatial distribution of highest waves (see Section 6.2.5), strongest currents (see Section 5.2.3), and water depth (~30-45 mMSL). It is noted that higher waves and stronger currents occur at other locations within the EINS OWF area.

Results at **OWF-3**, the deepest location with the highest H_{max} (of the 8 points), is presented in the body of this report, while results at all locations are given in the data reports (listed in Appendix A: List of Data Reports) which are attached to this report.

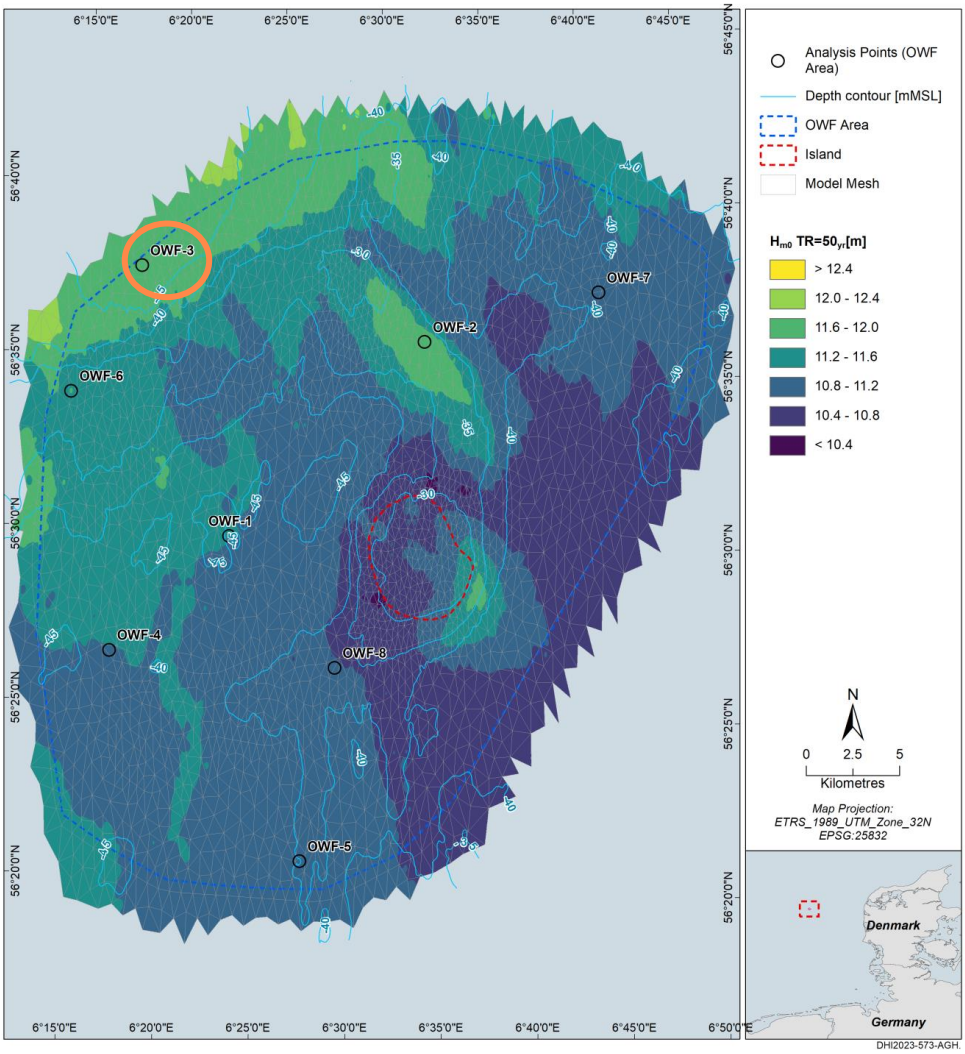

Figure 2.1 Map of the OWF area analysis points

Table 2.1 Coordinates and water depth of the OWF area analysis points

#	Name UK	Name DK	Longitude WGS84 [°E]	Latitude WGS84 [°N]	Depth, SW_{EINS} [mMSL]
1	OWF-1	HP-1	6.383875	56.498307	45.1
2	OWF-2	HP-2	6.547670	56.594867	32.2
3	OWF-3	HP-3	6.299272	56.626615	46.4
4	OWF-4	HP-4	6.283582	56.441426	42.5
5	OWF-5	HP-5	6.455368	56.343511	39.7
6	OWF-6	HP-6	6.241903	56.565019	32.7
7	OWF-7	HP-7	6.697654	56.621485	40.1
8	OWF-8	HP-8	6.479595	56.436893	36.9

3 Wind

This section presents a summary of the wind data basis established in [1], followed by a presentation of normal and extreme wind conditions.

Note that wind data is included only to assess the misalignment relative to waves (see Section 6.1.7). Other wind conditions are not addressed, cf. SoW [3].

The wind data was adopted from [2] and consisted of CFSR data during the period 1979 – 2022 (43.75 years). For convenience, we interpolated the CFSR data from its native resolution (~23 km and 1 hour) to the mesh and output time step of the wave model of this study (~400 m and 1800 s). The wind dataset is denoted EINS-AT-CFSR. Table 3.1 summarizes the metadata of the EINS-AT-CFSR dataset.

Table 3.1 Metadata of the EINS-AT-CFSR dataset
Time series data was provided to Energinet (.csv, .mat, .nc, .dfs0).

Name	Value
Dataset ID:	EINS-AT-CFSR
Start Date [UTC]:	1979-01-01 01:00:00
End Date [UTC]:	2022-09-30 23:30:00
Time Step [s]:	1800 (interpolated from 3600 s)
Cell Size [m]:	~800 (interpolated from ~23 km)

The CFRS wind is considered representative of a 2-hour averaging period, see [2], at 10 m height. Methods of converting to other temporal averages and heights are assessed for normal and extreme conditions respectively.

The wind analyses are presented in speed bins of 1.0 m/s and directional bins of 22.5° at 10 (and 30) m height. The direction is from where the wind is coming from. Table 3.2 presents the variables of the EINS-AT-CFSR dataset, including the bin sizes applied in figures and tables.

Table 3.2 Wind variables of the EINS-AT-CFSR dataset
The wind direction is from where the wind is blowing.

Variable name	Abbrev.	Unit	Bin size
Wind speed at 10 m height	WS_{10}	m/s	1.0
Wind direction at 10 m height	WD_{10}	°N-from	22.5

The wind analyses cover the data period 1979-09-01 – 2022-08-31 (43 years), a round number of years, which is preferrable for extreme value analyses (hence, to align with the common data period of waves etc.).

The main body of this report presents results at OWF-3 (the deepest location), while results at all analysis points are given in the data reports (listed in Table 11.1) which are attached to this report. The data reports contain all (scatter) tables and figures presented below.

3.1 Normal wind conditions

The normal wind conditions are presented in terms of:

- Time series
- Wind rose

3.1.1 Time series

Figure 3.1 show a time series of wind speed at OWF-3 during the 43 years hindcast period. The mean is 8.8 m/s, and max is 31.0 m/s.

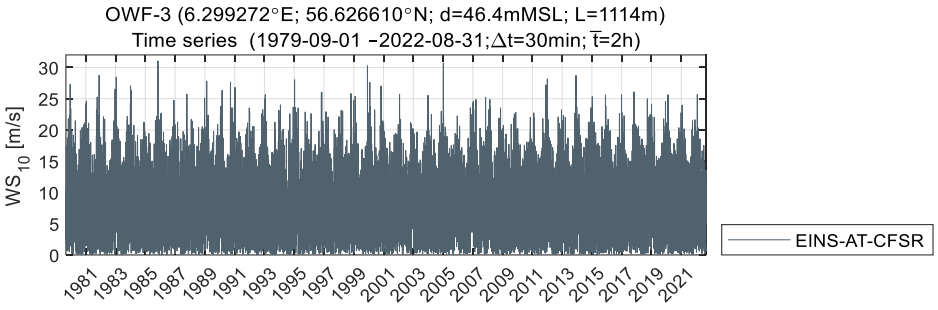

Figure 3.1 Time series of wind speed at OWF-3

3.1.2 Wind rose

Figure 3.2 shows a wind rose at OWF-3. As typical for the North Sea, wind occurs from all directions, but with a predominance from west, and least frequently from northeast.

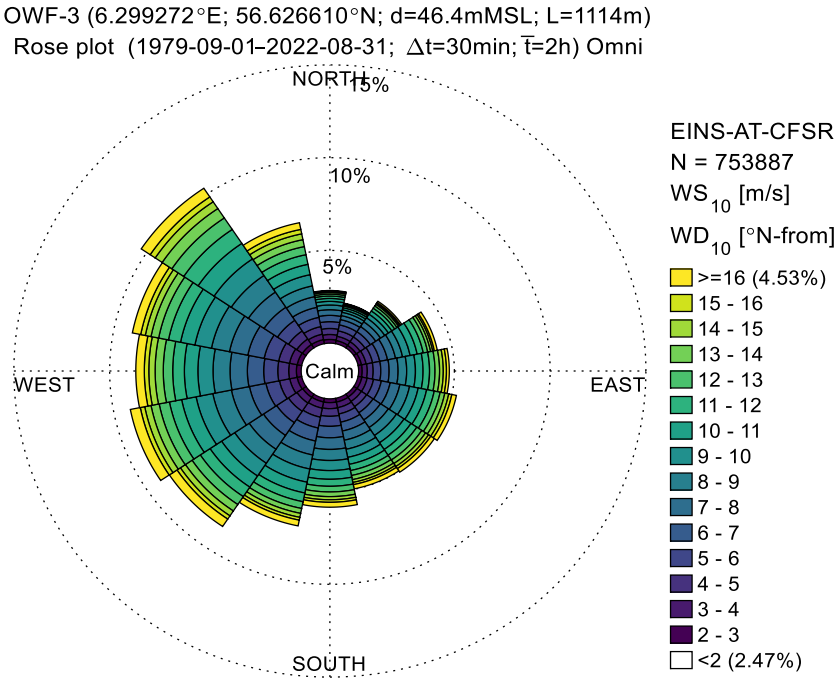

Figure 3.2 Wind rose at OWF-3

4 Water Level

This section presents a summary of the water level data basis established in [1], followed by a presentation of normal and extreme water level conditions.

The water level data was adopted from the hydrodynamic model forced by CFSR established for EINS (HD_{EINS}) in [2]. The water level consists of a tidal and a non-tidal (residual) component. The two components were separated by harmonic analysis (see Section 4.1.2). The water level dataset is denoted EINS-HD-CFSR. Table 4.1 summarises the metadata of the EINS-HD-CFSR dataset.

Table 4.1 Metadata of the EINS-HD-CFSR dataset
Time series data is provided to Energinet (.csv, .mat, .nc, and .dfs0).

Name	Value
Dataset ID:	EINS-HD-CFSR
Start Date [UTC]:	1979-01-01 01:00:00
End Date [UTC]:	2022-09-30 23:30:00
Time Step [s]:	1800
Cell Size [m]:	~800 (OWF area)

The water level data is relative to mean sea level (MSL).

The water level analyses are presented in bins of 0.1 m. Table 4.2 presents the water level variables of the EINS-HD-CFSR dataset, including the bin sizes applied in figures and tables throughout this report.

Table 4.2 Water level variables of the EINS-AT-CFSR dataset

Variable name	Abbrev.	Unit	Bin size
Water Level – Total	WL_{total}	mMSL	0.1
Water Level – Tide	WL_{tide}	mMSL	0.1
Water Level - Residual	$WL_{residual}$	m	0.1

The water level analyses cover the data period 1979-09-01 – 2022-08-31 (43 years), a round number of years, which is preferrable for extreme value analyses.

The main body of this report presents results at OWF-3 (the deepest location), while results at all analysis points are given in the data reports (listed in Table 11.1) which are attached to this report. The data reports contain all (scatter) tables and figures presented below.

4.1 Normal water level conditions

The normal water level conditions are presented in terms of:

- Time series
- Tidal levels
- Histogram
- Monthly statistics

4.1.1 Time series

Figure 4.1 shows a time series of water level at OWF-3 during the 43-year period, for total, tidal, and residual components. The 'de-tiding' of water level is explained in Section 4.1.2. The highest total and residual water levels are 1.54 mMSL and 1.52 m. The tidal levels are given in Section 4.1.2.

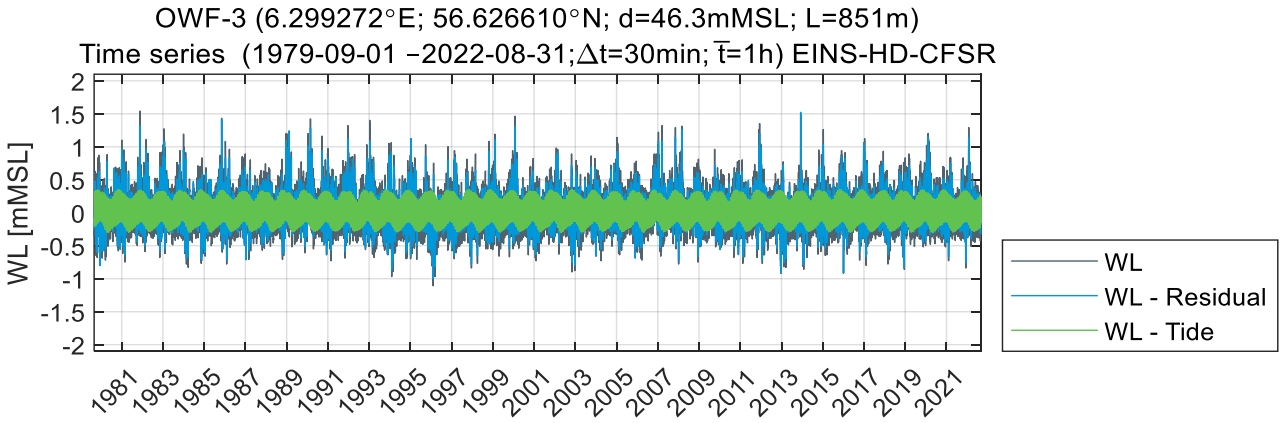

Figure 4.1 Time series of water level at OWF-3

4.1.2 Tidal levels

The tides are weak at EINS, but to quantify this, astronomical water levels (tidal levels) are provided below. The levels were calculated using harmonic analysis to separate the tidal and non-tidal (residual) components of the total water level time series from the hydrodynamic model (after subtracting the mean of the data).

Figure 4.1 shows the time series of the total, astronomical tidal and residual water level at OWF-3, while Table 4.3 summarises the astronomical water levels. The tide can be characterized as semi-diurnal (i.e., two high tides per day). The HAT is +0.35 mMSL and LAT -0.30 mMSL, giving a total tidal envelope of 0.65 m.

The harmonic analysis was conducted using the U-tide toolbox, [10], which is based on the IOS tidal analysis method by the Institute of Oceanographic Sciences as described in [11], and integrates the approaches defined in [12] and [13]. The residual water level was derived by subtracting the predicted tidal level from the total water level. The astronomical water levels are defined as (https://ntslf.org/tgi/definitions):

- HAT: Maximum predicted WL
- MHWS: Average of the two successive high waters reached during the 24 hours when the tidal range is at its greatest (spring tide)
- MHWN: Average of the two successive high waters reached during the 24 hours when the tidal range is at its lowest (neap tide)
- MLWN: Average of the two successive low waters reached during the 24 hours when the tidal range is at its lowest (neap tide)
- MLWS: Average of the two successive low waters reached during the 24 hours when the tidal range is at its greatest (spring tide)
- LAT: Minimum predicted WL

Table 4.3 Tidal levels at OWF-3

Tidal level	Abbreviation	Value	Unit
Highest astronomical tide	HAT	0.35	mMSL
Mean high water springs	MHWS	0.23	mMSL
Mean high water neaps	MHWN	0.12	mMSL
Mean sea level	MSL (z0)	0.00	mMSL
Mean low water neaps	MLWN	-0.12	mMSL
Mean low water springs	MLWS	-0.17	mMSL
Lowest astronomical tide	LAT	-0.30	mMSL

4.1.3 Histogram

Figure 4.2 shows a histogram of total water level at OWF-3.

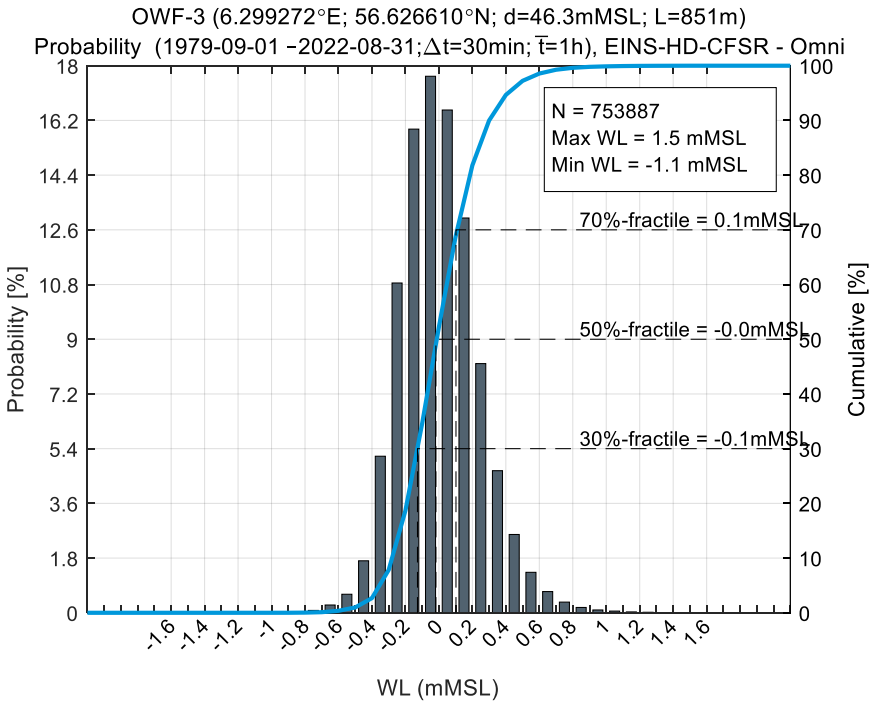

Figure 4.2 Histogram of total water level at OWF-3

4.1.4 Monthly statistics

Figure 4.3 shows monthly statistics of total water level at OWF-3. The monthly mean water level varies within ± 0.1 m during the year, being lowest in spring/summer and highest in winter. The highest (+1.5 mMSL), as well as the lowest (-1.1m MSL) water levels, occur during winter (Nov. to Feb.).

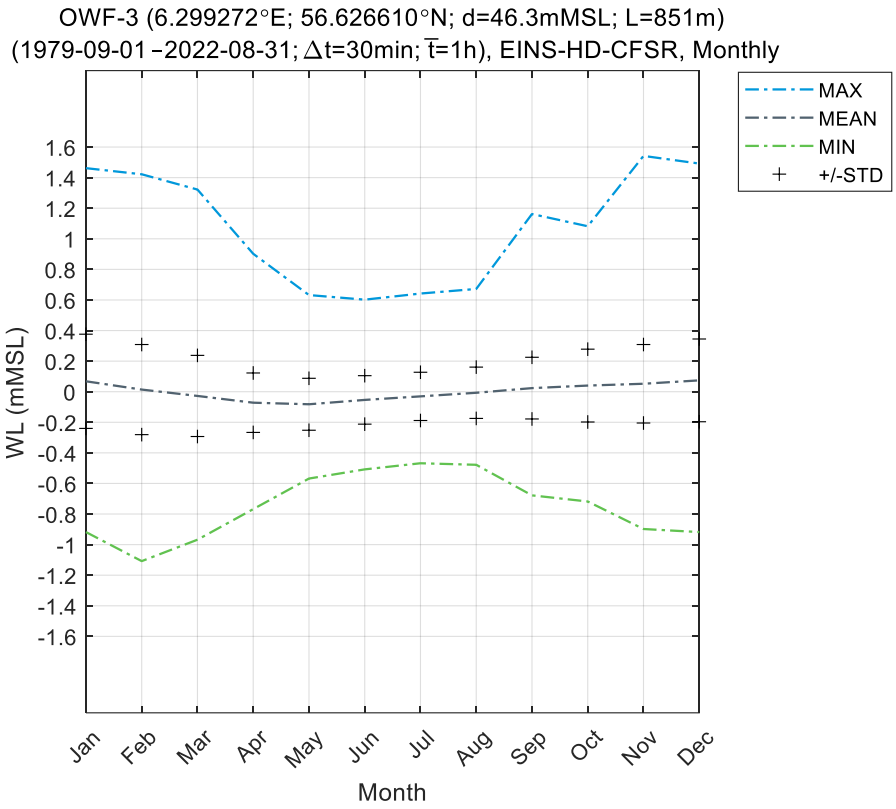

Figure 4.3 Monthly statistics of total water level at OWF-3

4.2 Extreme water level conditions

Extreme water level conditions were established using Traditional Extreme Value Analysis (T-EVA) following the methodology and settings derived and described in Appendix B: Sensitivity of T-EVA to Distribution, Threshold, and Fitting and Appendix C: T-EVA – Traditional EVA.

For water level, the exponential distribution fitted by least-square to the 215 (5x43) peak events separated by at least 36 hours is applied.

It is noted that the total water level is a combination of a deterministic tidal and stochastic residual water level. Therefore, EVA on the total water levels is, statistically speaking, not viable. However, at EINS, the extreme water levels are dominated by the residual, and hence, the significance of separating the two signals for EVA is negligible.

4.2.1 Extreme high water levels

Table 4.4 and Figure 4.4 present the extreme total high water level at OWF-3. The fitted distribution aligns very well to the hindcast data points, also at the tail, and all events are within the confidence levels, which gives confidence in the derived values. The 50-year total high water level is 1.67 ± 0.11 mMSL (the 2.5- and 97.5%-tile confidence levels).

Table 4.4 Extreme Total High Water Level at OWF-3

Return period, T_R [years]	$WL_{total,high}$ [mMSL]		
	2.5%-tile	Central estimate	97.5%-tile
1	1.00	1.03	1.06
5	1.23	1.30	1.36
10	1.33	1.41	1.48
50	1.55	1.67	1.77

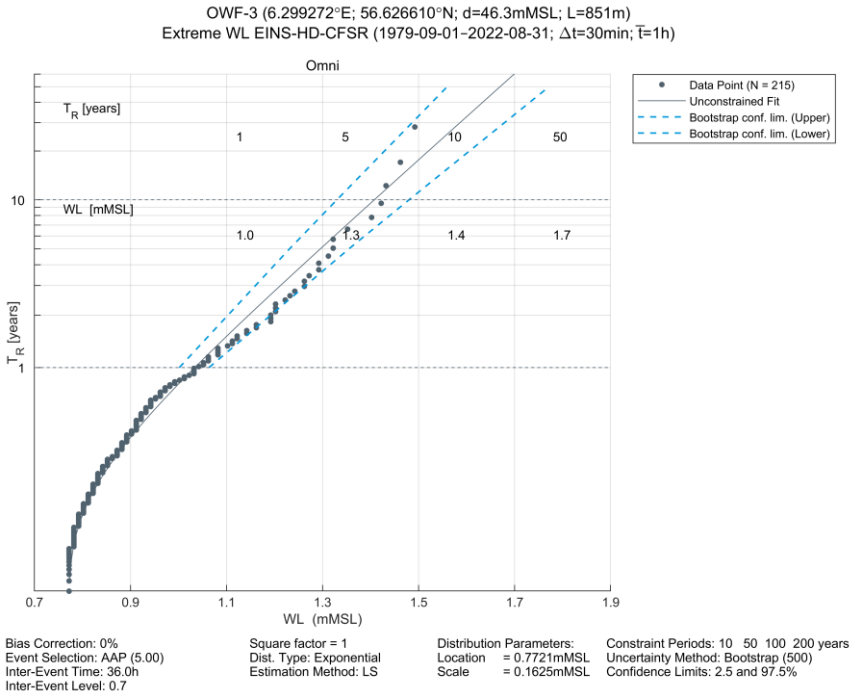

Figure 4.4 Extreme total High Water Level at OWF-3

4.2.2 Extreme low water levels

Table 4.5 and Figure 4.5 present the extreme total low water level at OWF-3. The fitted distribution aligns well to the hindcast data points, and most of the events are within the confidence levels, except at the tail where the distribution is slightly below (conservative) compared to the hindcast events. The 50-year total low water level is -1.13 ± 0.07 mMSL (the 2.5- and 97.5%-tile confidence levels).

Table 4.5 Extreme Total Low Water Level at OWF-3

Return period, T_R [years]	$WL_{total,low}$ [mMSL]		
	2.5%-tile	Central estimate	97.5%-tile
1	-0.70	-0.72	-0.74
5	-0.85	-0.89	-0.93
10	-0.92	-0.96	-1.01
50	-1.07	-1.13	-1.20

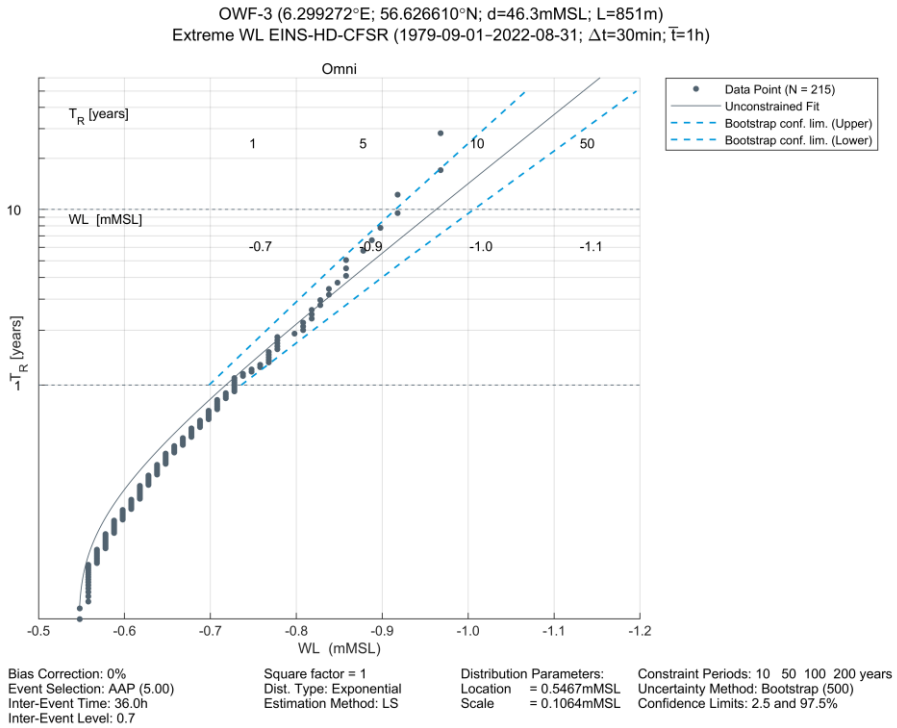

Figure 4.5 Extreme Total Low Water Level at OWF-3

5 Current

This section presents a summary of the current data basis established in [1], followed by a presentation of normal and extreme current conditions.

The current data is adopted from the hydrodynamic model forced by CFSR established for EINS (HD_{EINS}) [1]. The current consists of a tidal and a non-tidal (residual) component. The two components were separated by harmonic analysis (see Section 4.1.2). The current dataset is denoted EINS-HD-CFSR. Table 5.1 summarizes the metadata of the EINS-HD-CFSR dataset.

Table 5.1 Metadata of the EINS-HD-CFSR dataset.
Time series data is provided to Energinet (.csv, .mat, .nc, and .dfs0).

Name	Value
Dataset ID:	EINS-HD-CFSR
Start Date [UTC]:	1979-01-01 01:00:00
End Date [UTC]:	2022-09-30 23:30:00
Time Step [s]:	1800
Cell Size [m]:	~800 (OWF area)

The current data is considered representative of 1-hour average values of depth-average and is given at 30-min interval.

The current analyses are presented in speed bins of 0.05 m/s and directional bins of 22.5°. Table 5.2 presents the variables of the EINS-HD-CFSR dataset, including the bin sizes applied in figures and tables throughout this report.

Table 5.2 Current variables of the EINS-HD-CFSR dataset.
The current direction is to where the current is flowing.

Variable name	Abbrev.	Unit	Bin size
Current speed - Depth-average - Total	$CS_{avg,tot}$	m/s	0.05
Current direction - Depth-average - Total	$CD_{avg,tot}$	°N-to	22.5

The current analyses cover the data period 1979-09-01 – 2022-08-31 (43 years), a round number of years, which is preferrable for extreme value analyses.

The main body of this report presents results at OWF-3 (the deepest location), while results at all analysis points are given in the data reports (listed in Table 11.1) which are attached to this report. The data reports contain all (scatter) tables and figures presented below.

5.1 Normal current conditions

The normal current conditions are presented in terms of:

- Normal current profile
- Time series
- Current roses
- Histogram
- Monthly statistics
- Directional statistics
- Maps of mean current speed

5.1.1 Normal current profile

Current profiles are assessed in Section 5 of Part A, [1].

For normal (mean) conditions, it is recommended to apply a power profile with α = 1/7, cf. Section 4.1.4.2 in DNV RP-C205 [5], with the surface (z = 0) current speed estimated as 8/7 (1.14) times the depth-averaged current speed.

However, it is noted that individual current profiles deviate substantially from the (mean) power profile, and the (mean) normal current profile can therefore, not be applied to represent all single/individual current profiles.

5.1.2 Time series

Figure 5.1 shows a time series of current speed at OWF-3 during the 43 years hindcast period, for total, tidal, and residual. The 'de-tiding' of current speed follows the method given in Section 4.1.2 for water level. The highest total and residual current speeds are 1.04 and 0.95 m/s respectively.

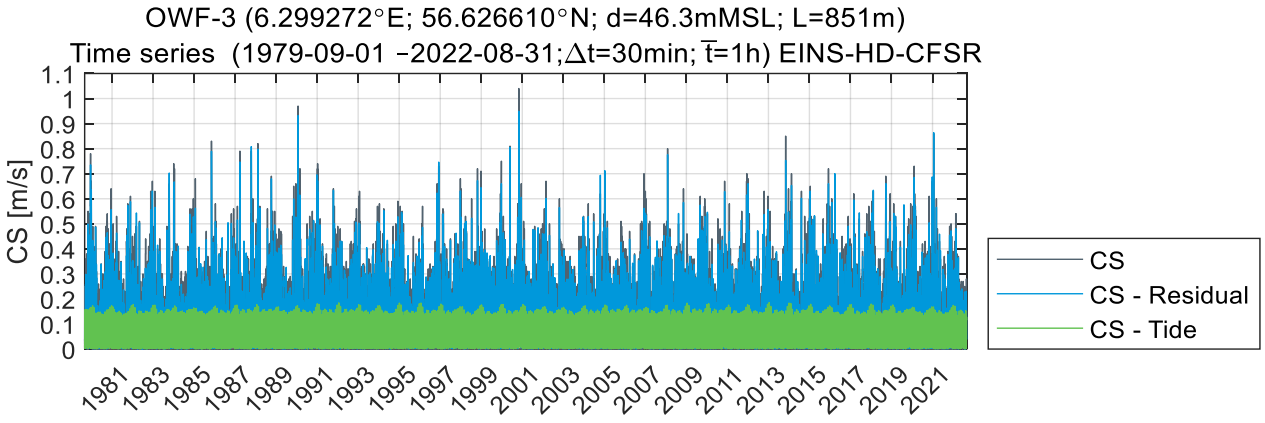

Figure 5.1 Time series of current speed at OWF-3.

5.1.3 Current roses

Figure 5.2, Figure 5.3, and Figure 5.4 show current roses for total, tidal, and residual conditions at OWF-3. The total rose shows currents predominantly towards northeast, which is due to the prevailing residual currents going towards the northeast. The tidal currents are very weak (< 0.15 m/s most of the time).

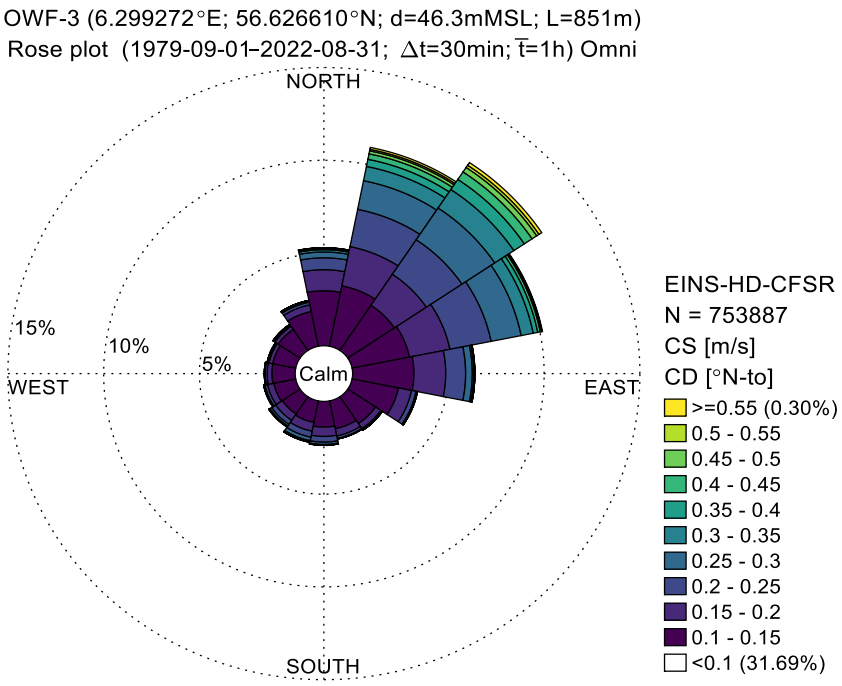

Figure 5.2 Total current rose at OWF-3

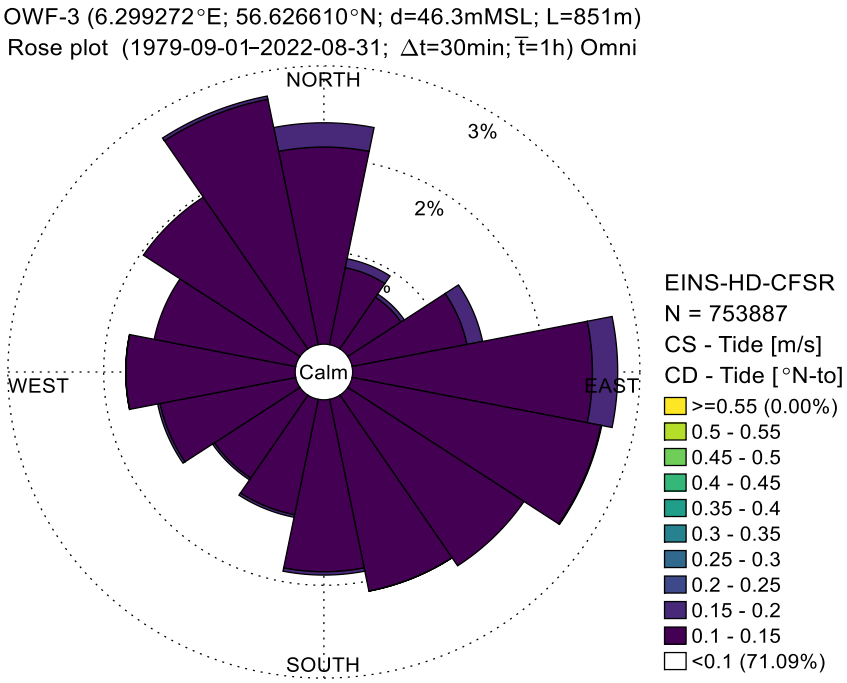

Figure 5.3 Tidal current rose at OWF-3

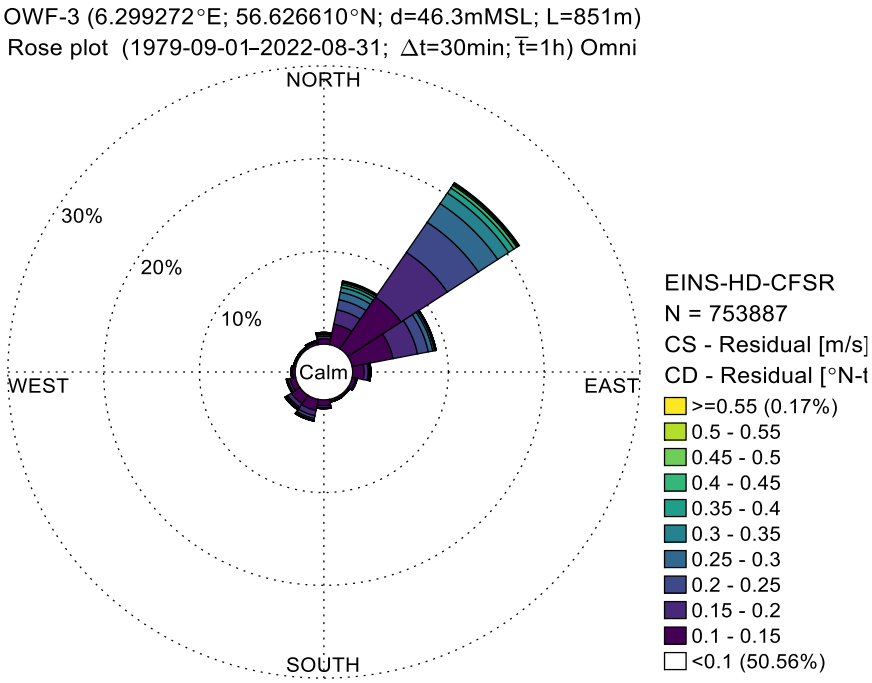

Figure 5.4 Residual current rose at OWF-3

5.1.4 Histogram

Figure 5.5 shows a histogram of current speed at OWF-3.

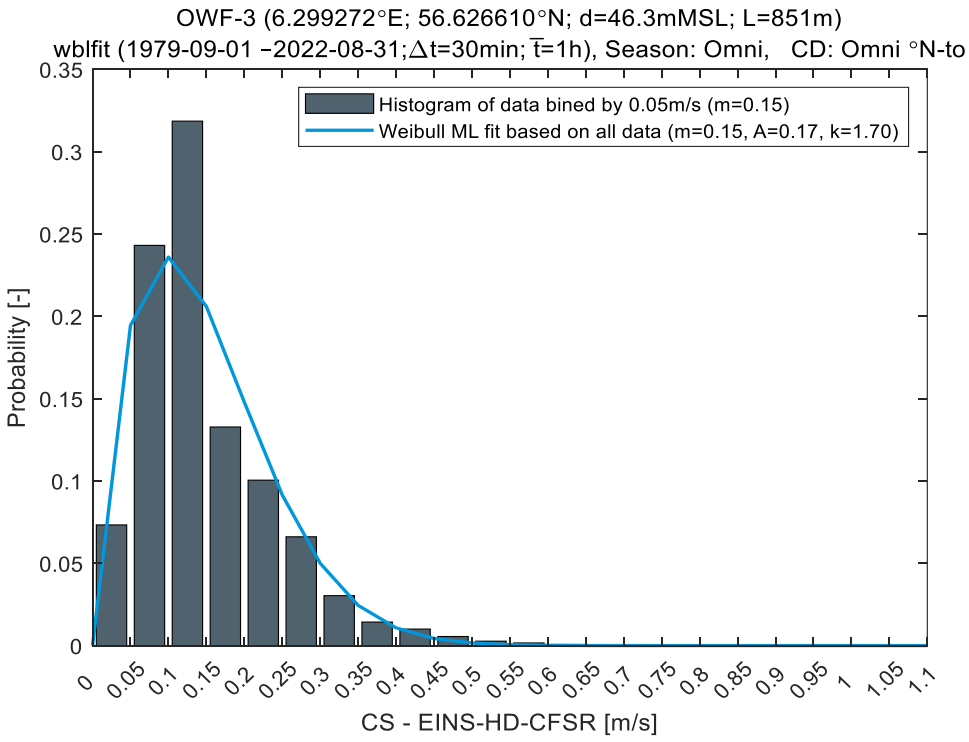

Figure 5.5 Histogram of current speed at OWF-3

5.1.5 Monthly statistics

Figure 5.6 shows monthly statistics of current speed at OWF-3. The monthly mean current speed varies within 0.15 - 0.2 m/s during the year, being weakest in summer and strongest in winter. The strongest current speeds (up to 1.04 m/s) occur during autumn - winter (Oct. – Jan.).

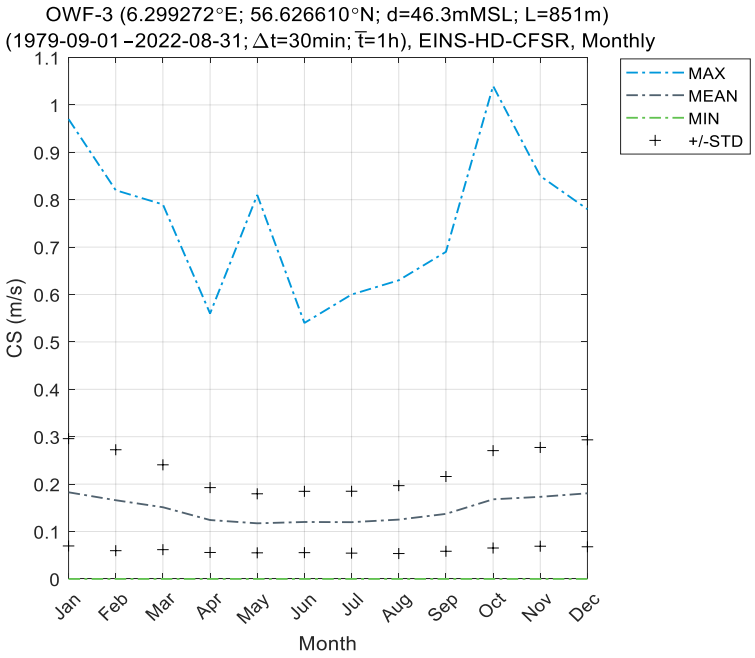

Figure 5.6 Monthly statistics of current speed at OWF-3.

5.1.6 Directional statistics

Figure 5.7 shows directional statistics of current speed at OWF-3. The mean current speed is strongest towards the northeast (45°) of about 0.22 m/s, and about 0.09 m/s for other directions. The strongest max current speeds occur towards the northeast and reach 1.04 m/s.

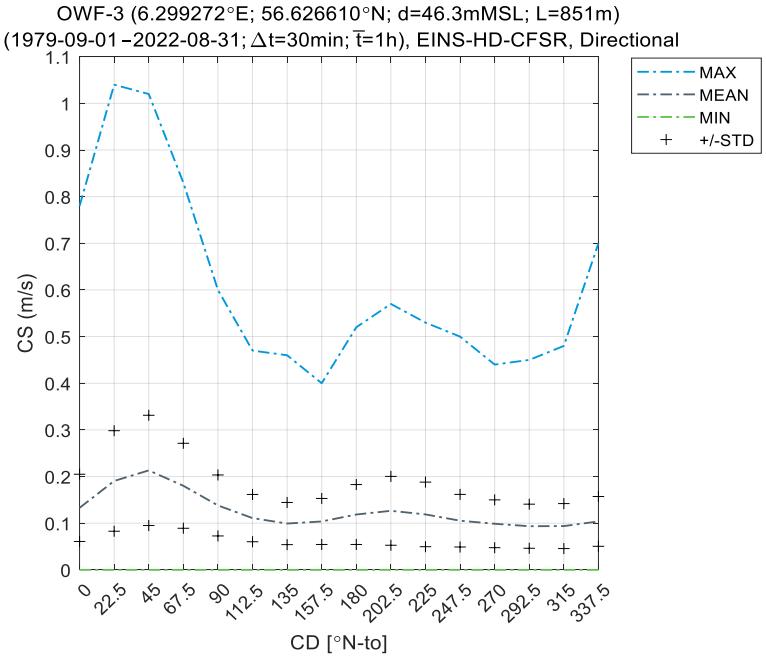

Figure 5.7 Directional statistics of current speed at OWF-3

5.1.7 Maps of mean current speed

Figure 5.8 presents the spatial variation across EINS OWF area of the mean total depth-averaged current speed. Mean values of CS_{tot} from the hindcast data at each mesh element are calculated and the variation is presented as contours. As seen, there is hardly any variation (0.17±0.07 m/s) across the EINS OWF area.

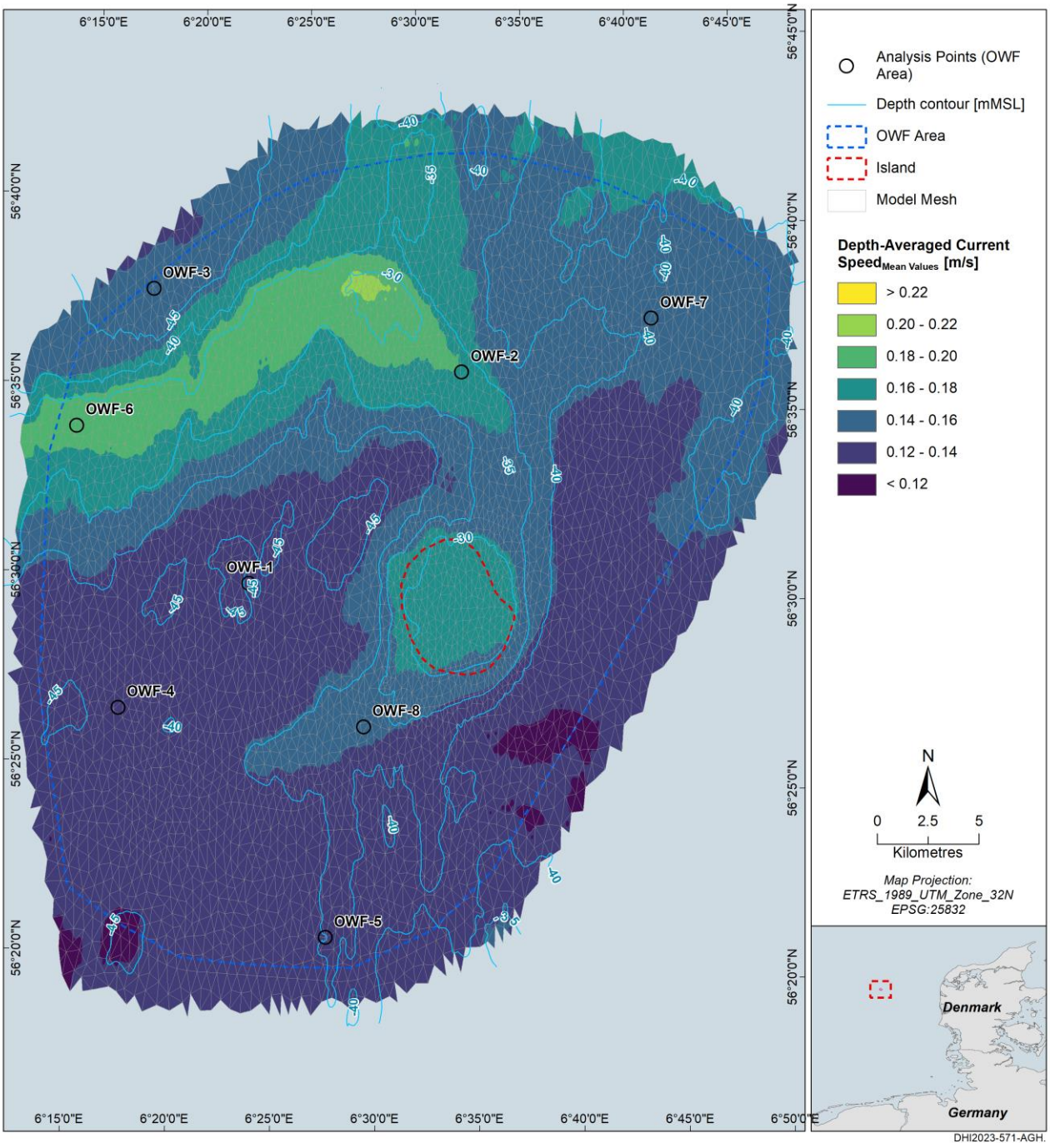

Figure 5.8 Spatial variation across EINS OWF area of the mean total depth-averaged current speed
The colour map shows the current speed, and the contours show the water depth.

5.2 Extreme current conditions

Extreme current conditions were established using Traditional Extreme Value Analysis (T-EVA) following the methodology and settings derived and described in Appendix B: Sensitivity of T-EVA to Distribution, Threshold, and Fitting and Appendix C: T-EVA – Traditional EVA.

For current speed the 2-p Weibull distribution fitted by least-square to the 129 (3x43) peak events separated by at least 36 hours is applied.

It is noted that the current is a combination of a deterministic tidal and stochastic residual water level. Therefore, EVA on the total current is, statistically speaking, not viable. However, at EINS, the extreme currents are dominated by the residual, and hence, the significance of separating the two signals for EVA is negligible.

5.2.1 Extreme current profile

Current profiles are assessed in Section 5 in Part A, [1]. A generally applicable and feasible current profile for currents during extreme events does not exist.

For extreme surface (z = 0 m) currents, it is recommended to apply a factor of 1.3 to convert the depth-average current speed to surface (z = 0 m). This is based on detailed assessment of measured and modelled 3D current data.

For extreme near-seabed (1 m above) currents, it is recommended to apply the power profile with $\alpha = 1/7$, cf. Section 4.1.4.2 in DNV RP-C205 [5], and the surface (z = 0) current speed estimated as 8/7 (1.14) times the depth-averaged current speed. This corresponds to a factor ranging from 0.65 at 25 m depth to a factor of 0.72 at 50 m depth.

5.2.2 Extreme total current speed

Table 5.3 and Figure 5.9 present the extreme total depth-averaged current speed at OWF-3.

The fitted distribution aligns very well to the hindcast data points, also at the tail, and all events are within the confidence levels, which gives confidence in the derived values. The 50-year total current speed is 1.0 ± 0.1 m/s (the 2.5- and 97.5%-tile confidence levels).

Table 5.4 and Table 5.5 present the extreme total surface and near-seabed current speed at OWF-3.

Table 5.3 Extreme total depth-averaged current speed at OWF-3

Return period, T_R [years]	$CS_{avg,tot}$ [m/s]		
	2.5%-tile	Central estimate	97.5%-tile
1	0.6	0.7	0.7
5	0.7	0.8	0.8
10	0.8	0.8	0.9
50	0.9	1.0	1.1

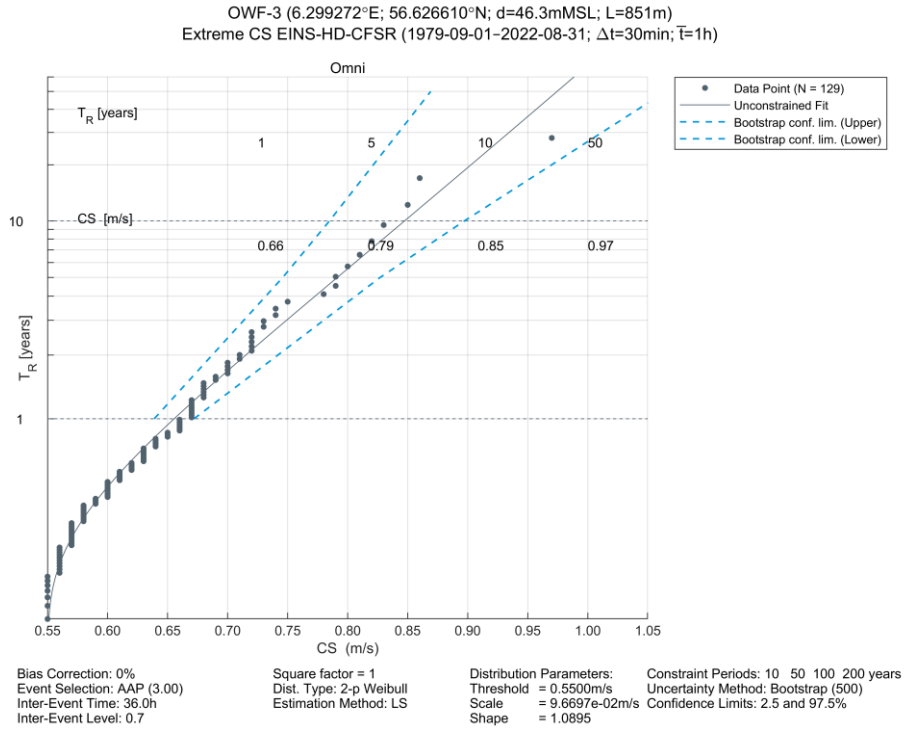

Figure 5.9 Extreme total depth-averaged current speed at OWF-3

Table 5.4 Extreme total near-seabed current speed at OWF-3

The extreme total near-seabed current speed (1 m above) is derived using the power profile with α = 1/7.

Return period, T_R [years]	$CS_{avg,bed}$ [m/s]		
	2.5%-tile	Central estimate	97.5%-tile
1	0.4	0.4	0.4
5	0.5	0.5	0.5
10	0.5	0.6	0.6
50	0.6	0.6	0.7

Table 5.5 Extreme total surface current speed at OWF-3

The extreme total surface current speed is taken as 1.3 times the depth-averaged total current speed.

Return period, T_R [years]	$CS_{avg,surf}$ [m/s]		
	2.5%-tile	Central estimate	97.5%-tile
1	0.8	0.9	0.9
5	1.0	1.0	1.1
10	1.0	1.1	1.2
50	1.1	1.3	1.4

5.2.3 Maps of extreme current speed

Figure 5.10 - Figure 5.11 present the spatial variation across EINS OWF area of total depth-averaged current speed for return periods of 1 and 50 years based on traditional extreme value analysis at each mesh element. The maximum CS_{tot} varies within about 1.05±0.25 m/s for the 100-year return period.

Note: The values within the island area (red dashed line) differ slightly from the values in Part B, [7], which are scaled according to J-EVA).

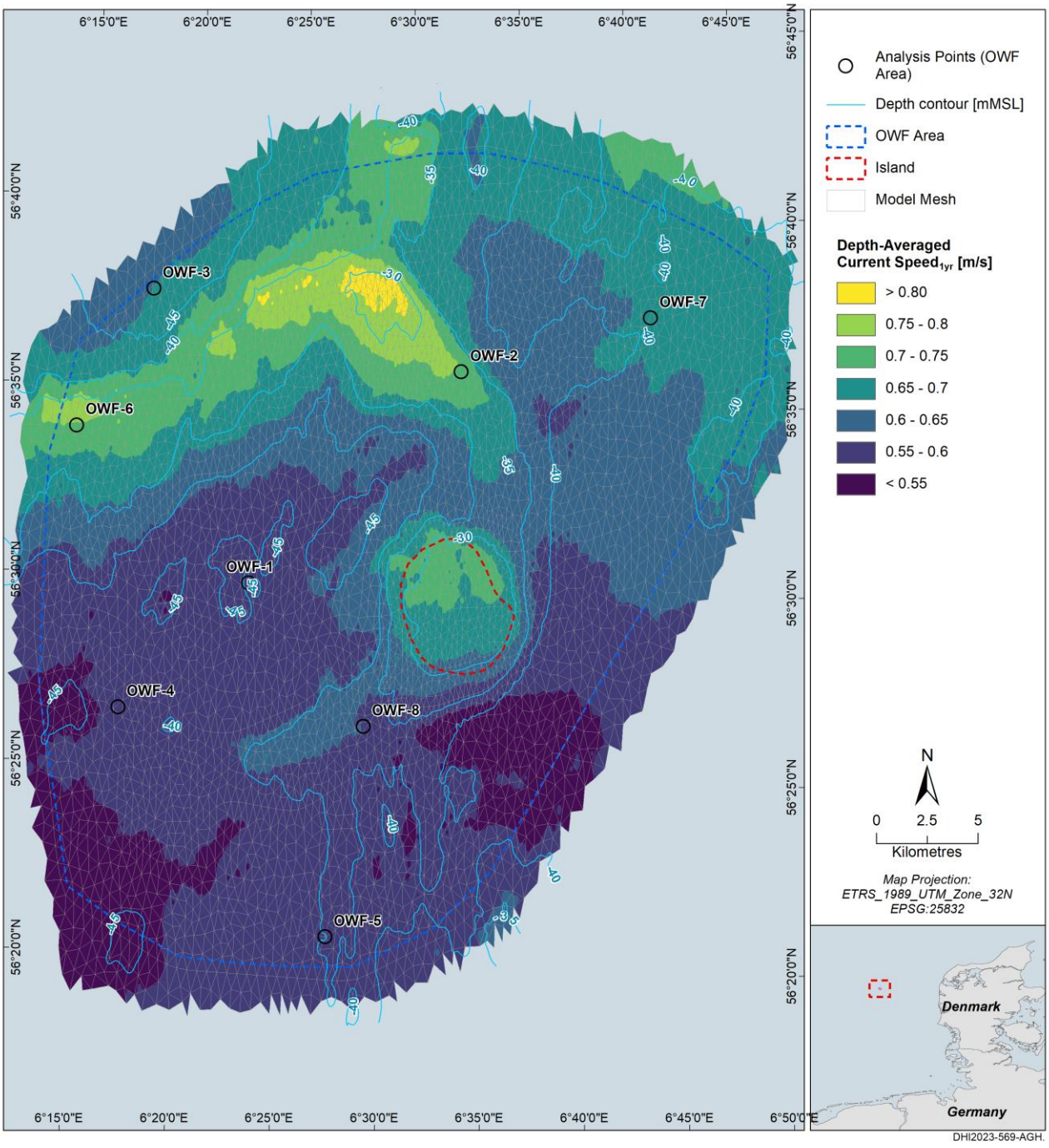

Figure 5.10 Spatial variation across EINS OWF area of total depth-averaged current speed for return period of 1 year
The colour map shows the current speed, and the contours show water depth.

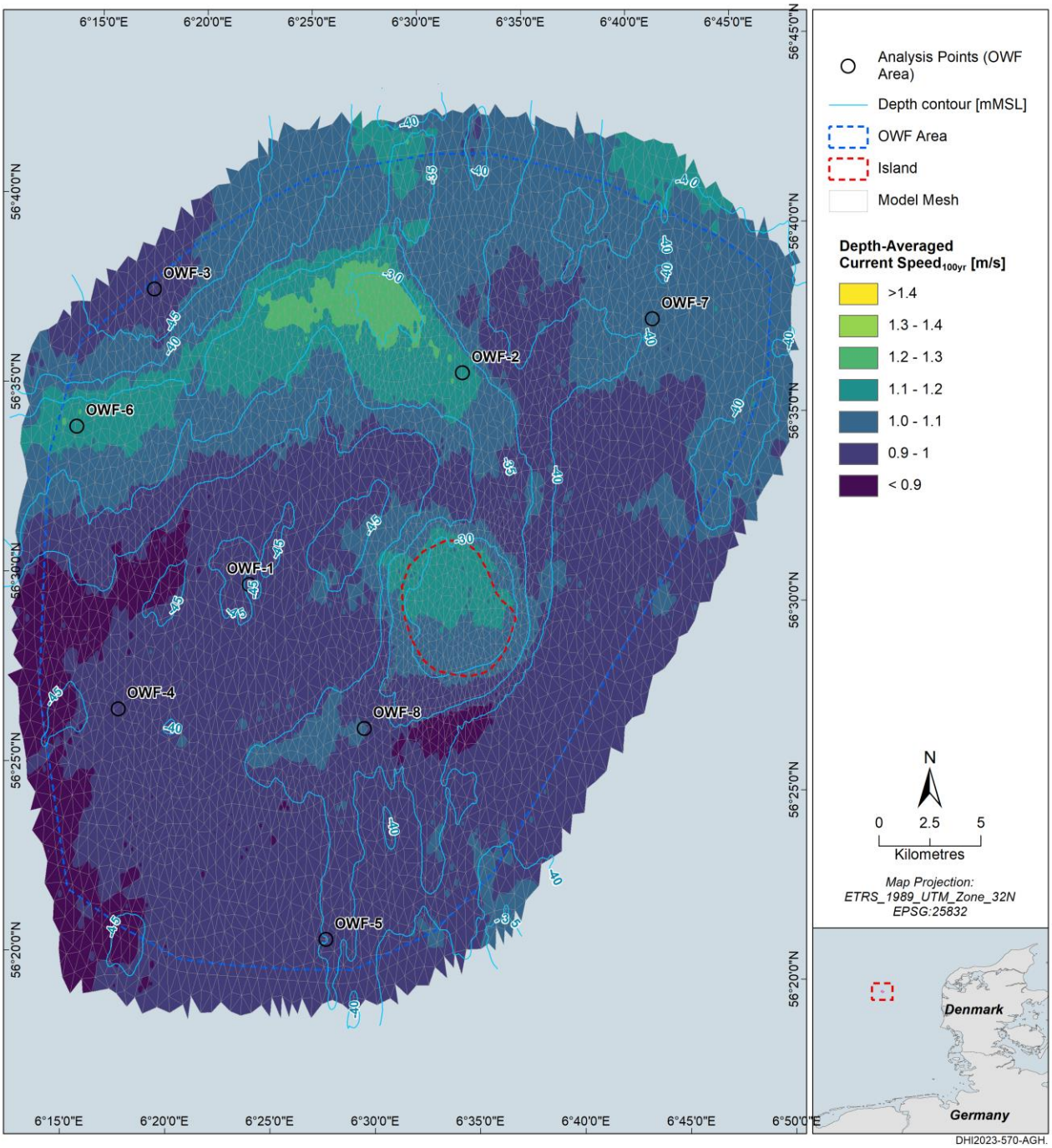

Figure 5.11 Spatial variation across EINS OWF area of total depth-averaged current speed for return period of 50 years

The colour map shows the current speed, and the contours show water depth.

6 Waves

This section presents a summary of the wave data basis established in [1], followed by a presentation of normal and extreme wave conditions.

The wave data is adopted from the spectra wave model forced by CFSR established for EINS (SW_{EINS}) in [2], containing total, wind-sea, and swell partition of the sea state (separated by the wave-age criterion as defined in Section 5.1 of [14]). The wave dataset is denoted EINS-SW-CFSR. Table 6.1 summarises the metadata of the EINS-SW-CFSR dataset.

Table 6.1 Metadata of the EINS-SW-CFSR dataset
Time series data is provided to Energinet (.csv, .mat, .nc, and .dfs0).

Name	Value
Dataset ID:	EINS-SW-CFSR
Start Date [UTC]:	1979-01-01 01:00:00
End Date [UTC]:	2022-09-30 23:30:00
Time Step [s]:	1800
Cell Size [m]:	~800 (OWF area)

The wave data is considered representative of 3-hour average sea state and is given at 30-min interval.

The wave analyses are presented in height bins of 0. 5 m, period bins of 0.5 s, and directional bins of 22.5°. Table 6.2 presents the variables of the EINS-SW-CFSR dataset, incl. the bin sizes applied in analyses throughout this report.

Table 6.2 Wave variables of the EINS-SW-CFSR dataset
The wave direction is from where the wave is coming.

Variable name	Abbrev.	Unit	Bin size
Significant wave height	H_{m0}	m	0.5
Peak wave period	T_p	s	0.5
Mean wave period	T_{01}	s	0.5
Zero-crossing wave period	T_{02}	s	0.5
Peak wave direction	PWD	°N (clockwise from)	22.5
Mean wave direction	MWD	°N (clockwise from)	22.5
Direction standard deviation	DSD	°	5

The wave analyses cover the data period 1979-09-01 – 2022-08-31 (43 years), a round number of years, which is preferrable for extreme value analyses.

The main body of this report presents results at OWF-3 (the deepest location), while results at all analysis points are given in the data reports (listed in Table 11.1) which are attached to this report. The data reports contain all (scatter) tables and figures presented below.

6.1 Normal wave conditions

The normal wave conditions are presented in terms of:

- Time series
- Wave rose
- Histogram
- Monthly statistics
- Directional statistics
- Scatter diagrams (H_{m0})
- Wind-wave misalignment
- Assessment of wave spectra, see Part A, [1].
- Maps of mean H_{m0}

6.1.1 Time series

Figure 6.1 show time series of the total, wind-sea, and swell partition of H_{m0}, T_p, and T_{02} at OWF-3 during the 43 years hindcast period. The mean is 1.96 m, and the maximum is 11.24 m (6th Nov. 1985).

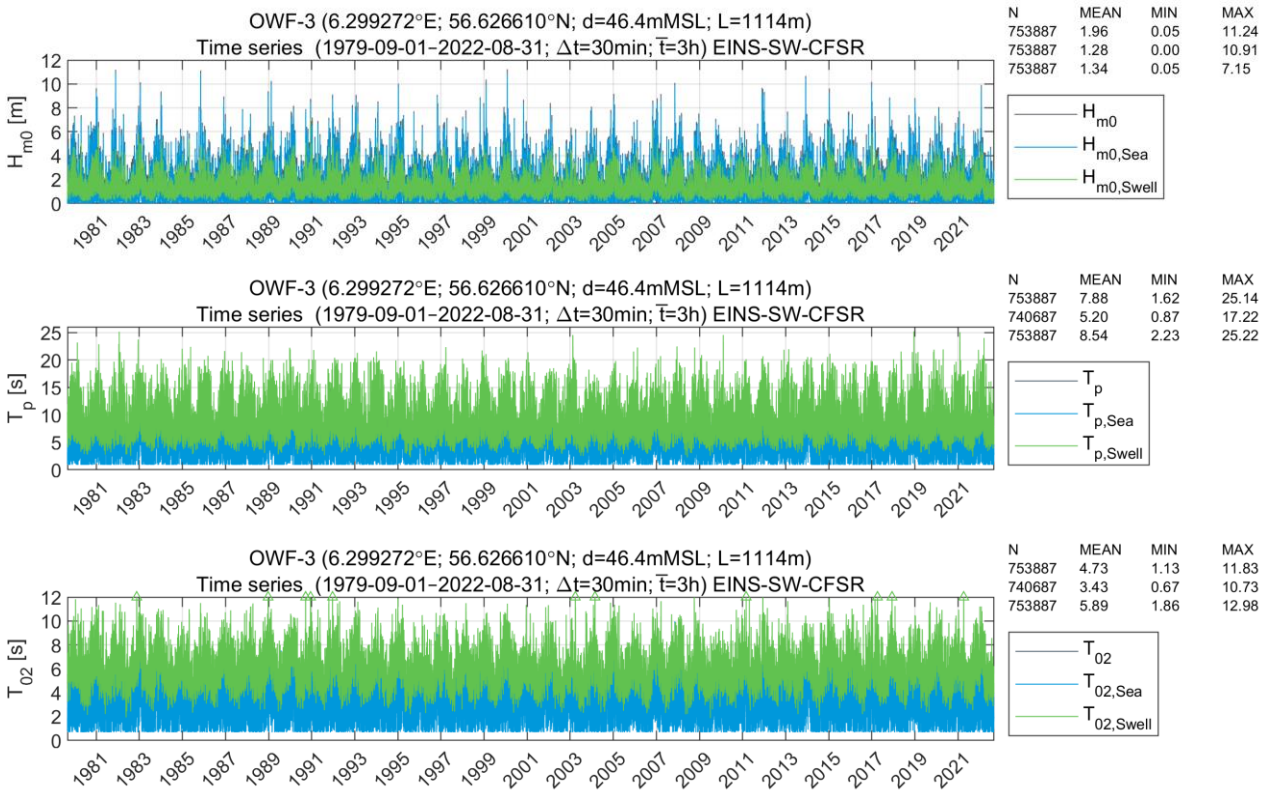

Figure 6.1 Time series of H_{m0}, T_p, and T_{02} at OWF-3

6.1.2 Wave roses

Figure 6.2 - Figure 6.4 shows wave roses at OWF-3 based on H_{m0} and MWD for total, wind-sea and swell respectively. As typical for the North Sea, the waves arrive primarily from the northwest, reflecting the direction that is open to the North Atlantic, and allows swell to enter the North Sea. Waves from easterly directions occur less than about 20% of the time.

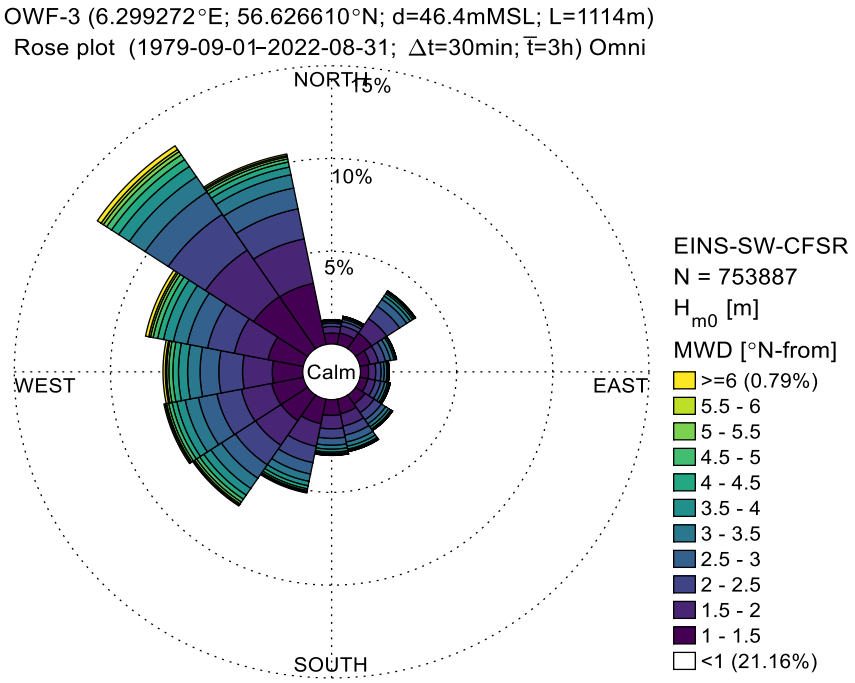

Figure 6.2 Wave rose at OWF-3; H_{m0} vs MWD – Total

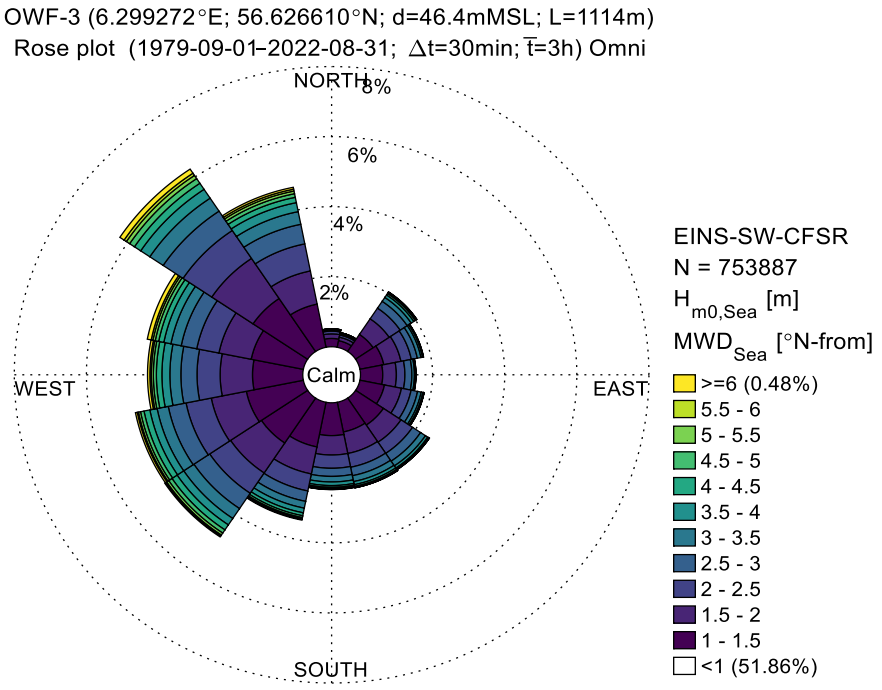

Figure 6.3 Wave rose at OWF-3; H_{m0} vs MWD – Wind-Sea

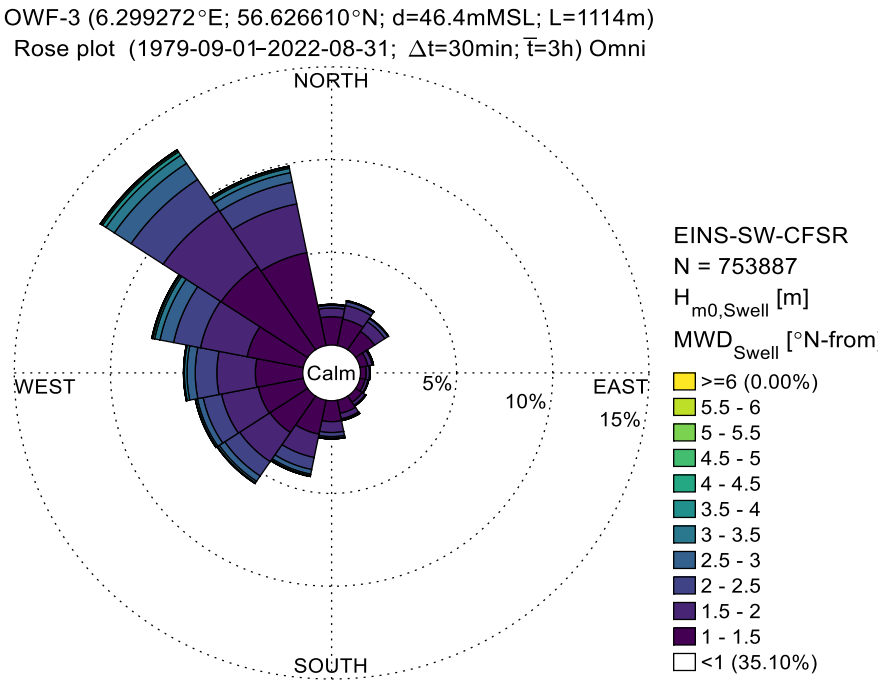

Figure 6.4 Wave rose at OWF-3; H_{m0} vs MWD – Swell

6.1.3 Histogram

Figure 6.5 shows a histogram of H_{m0} at OWF-3.

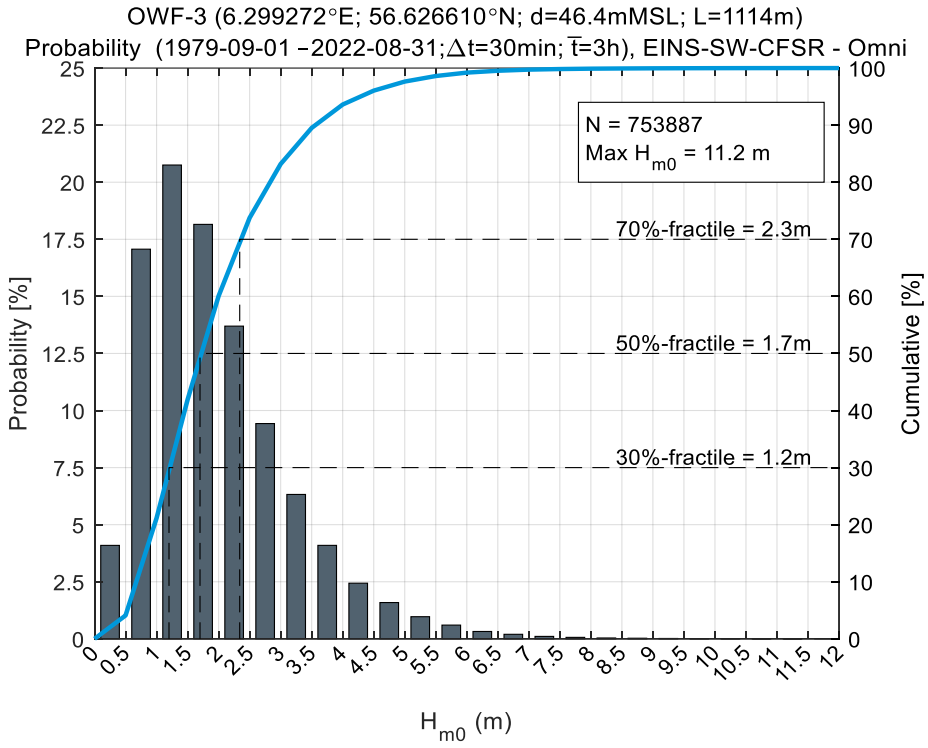

Figure 6.5 Histogram of H_{m0} at OWF-3

6.1.4 Monthly statistics

Figure 6.6 shows monthly statistics of significant wave height, H_{m0}, at OWF-3. The mean varies from 1.2 m during summer to 2.8 m during winter. The highest waves occurred during the months of Nov., Dec., and Jan.

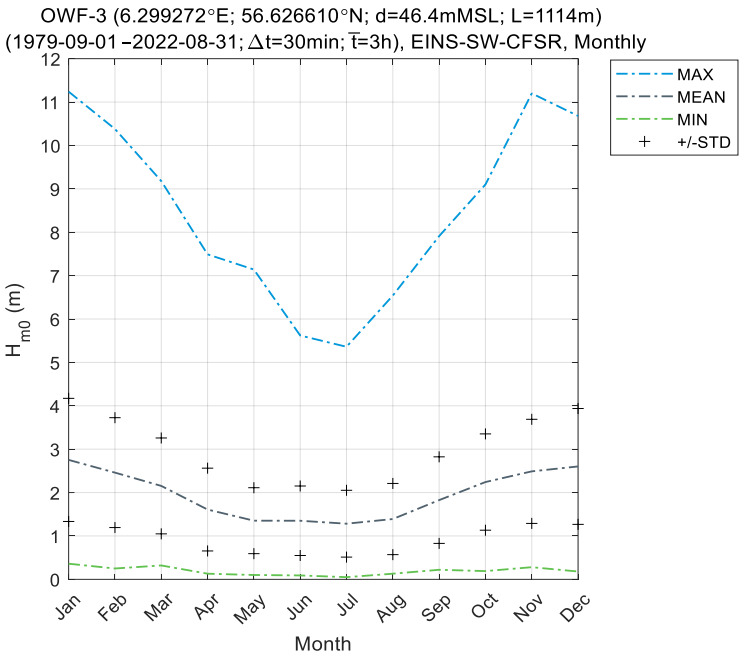

Figure 6.6 Monthly statistics of significant wave height at OWF-3

6.1.5 Directional statistics

Figure 6.7 shows directional statistics of significant wave height at OWF-3. The mean is highest from the northwest of about 2.1 m, and lowest from north of about 1.2 m. The highest waves occur form the north-western sector.

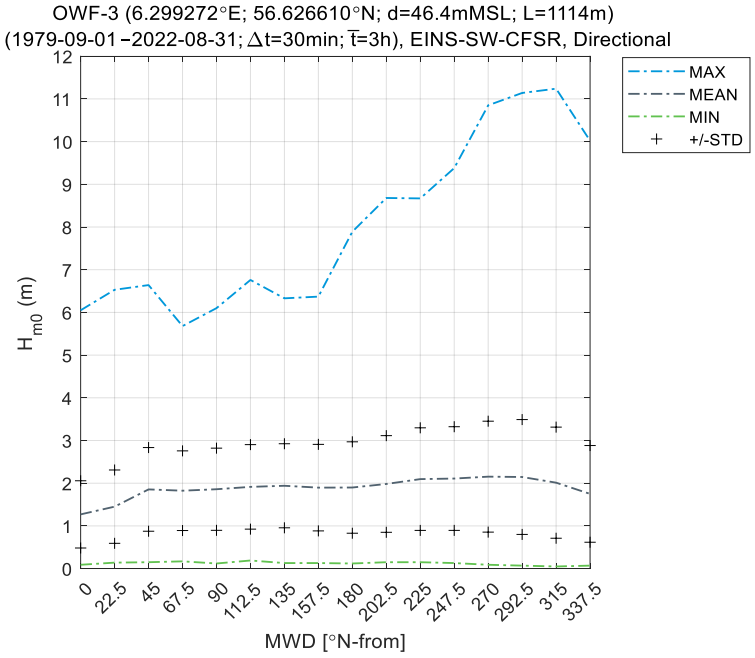

Figure 6.7 Directional statistics of significant wave height at OWF-3

6.1.6 Scatter diagrams (H_{m0})

This section presents scatter diagrams of H_{m0} against the following other metocean parameters at OWF-3:

- Figure 6.8 WS_{10} vs. H_{m0}
- Figure 6.9 H_{m0} vs. T_p
- Figure 6.10 H_{m0} vs. T_{02}
- Figure 6.11 H_{m0} vs. WL
- Figure 6.12 H_{m0} vs. CS

Each scatter diagram includes quantiles and functional fits to the 95%-tile highest data (except for WL and CS).

The scatter of WS_{10} vs H_{m0} shows a reasonable correlation, albeit with some scatter due to the (co-)occurrence of swell in the North Sea.

The wave periods (T_p and T_{02}) are very well correlated with $H_{m0,}$ especially for the high waves that are dominated by local wind.

There is weak correlation between WL (total) and H_{m0} indicating a slight trend of positive high water during high waves.

The total current speed (CS) is almost entirely uncorrelated with H_{m0}, albeit there is a weak trend of stronger currents during high waves, but with significant scatter.

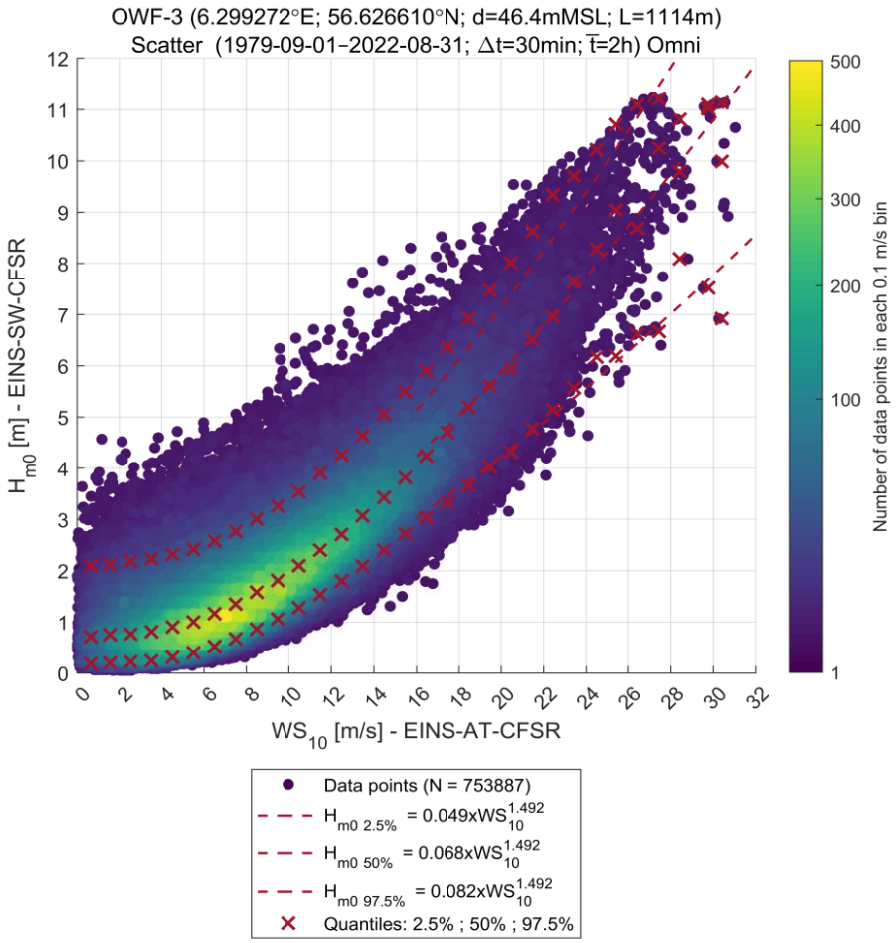

Figure 6.8 Scatter diagram of WS_{10} vs H_{m0} at OWF-3

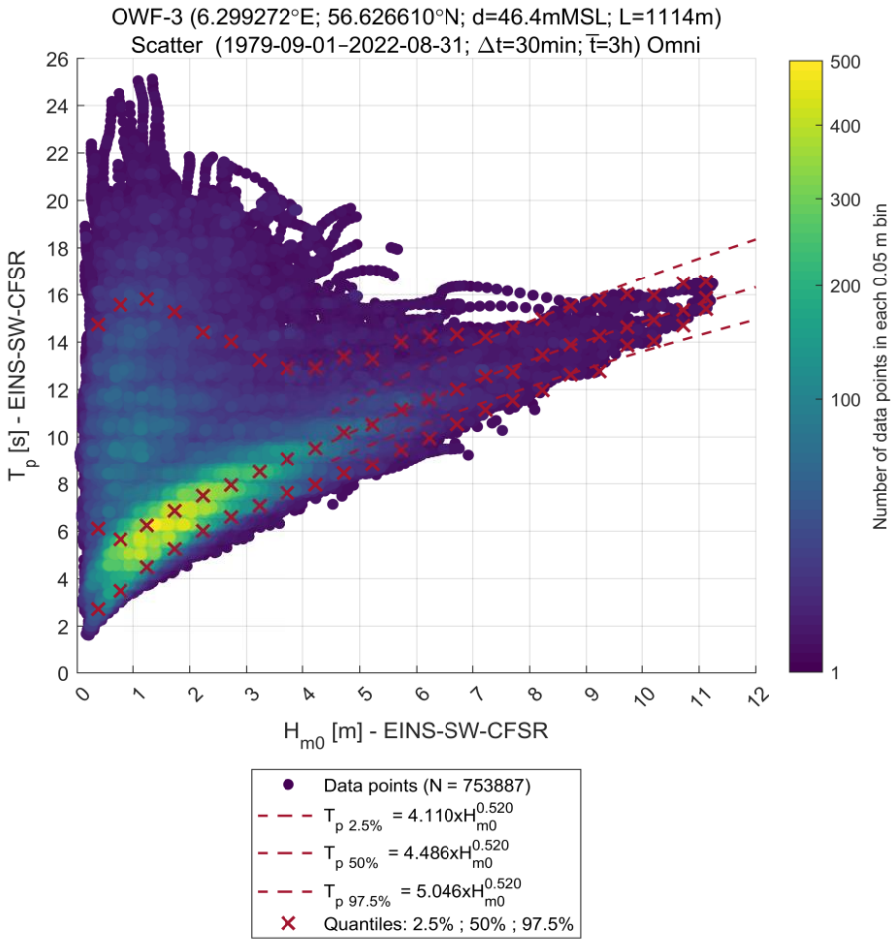

Figure 6.9 Scatter diagram of H_{m0} vs T_p at OWF-3

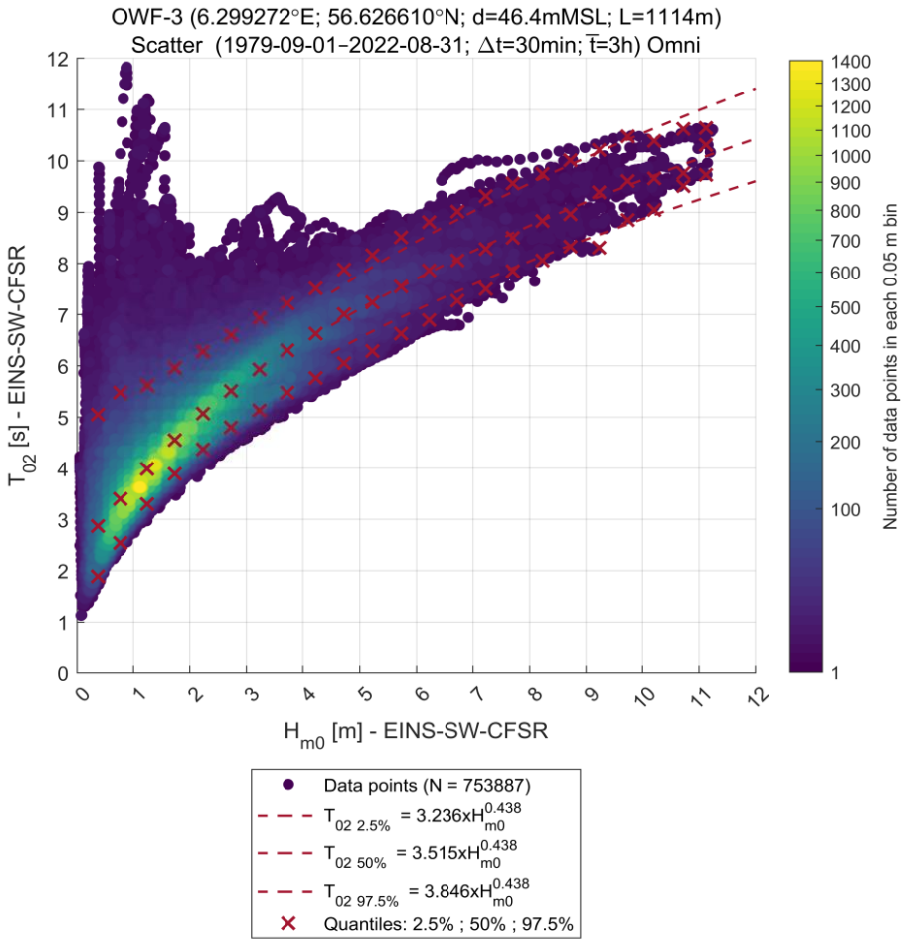

Figure 6.10 Scatter diagram of H_{m0} vs T_{02} at OWF-3

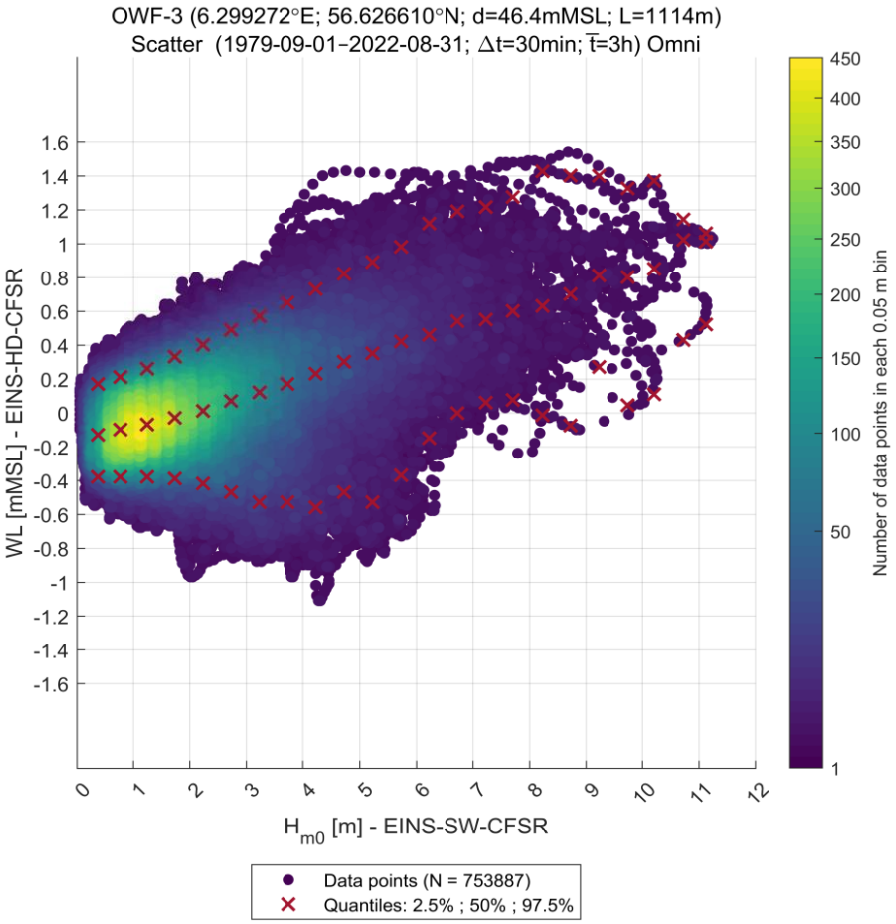

Figure 6.11 Scatter diagram of H_{m0} vs WL at OWF-3

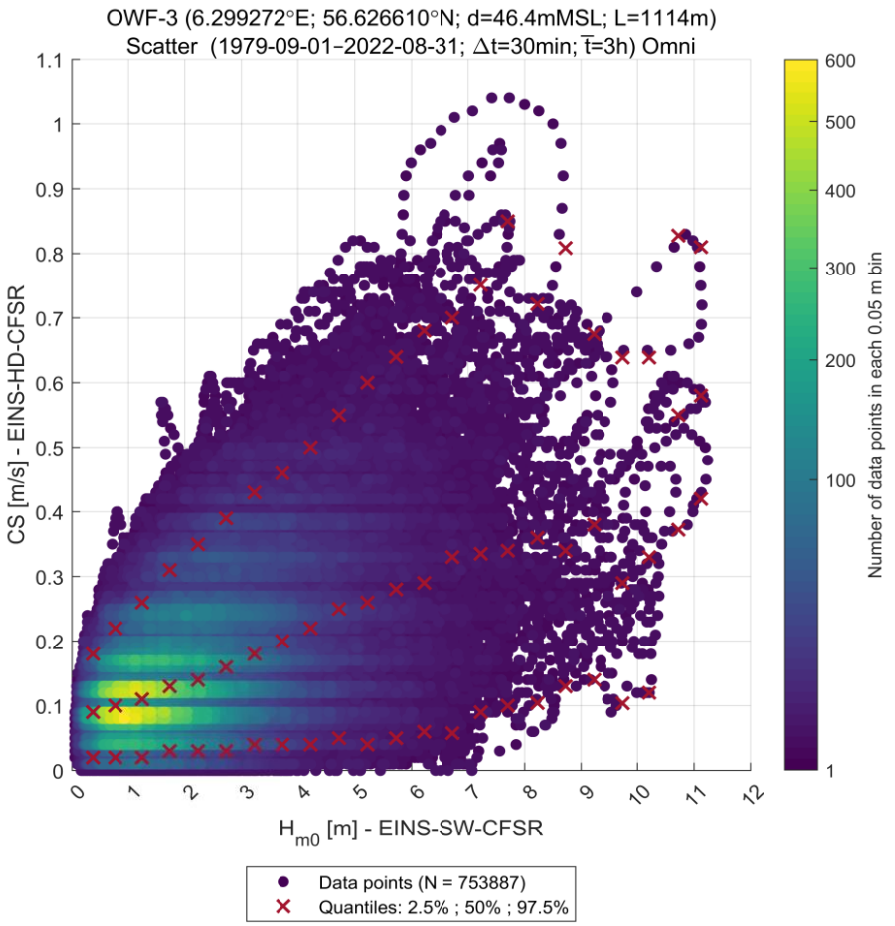

Figure 6.12 Scatter diagram of H_{m0} vs CS at OWF-3

6.1.7 Wind-wave misalignment

The wind-wave misalignment is calculated as WD_{10} minus the MWD. Figure 6.13 presents the misalignment vs. H_{m0} at OWF-3. The curves indicate the mean misalignment for each wind direction sector. The misalignment shows a high scatter for wave height less than ~3 m, while the scatter (misalignment) is relatively low for higher waves when the wind starts to pick up because extreme waves in the North Sea are generally dominated by the local wind.

Figure 6.14 shows a trend of most frequent misalignment between 0 – 22.5°. For omni and almost all directions, the main probability of misalignment is within ±45. Hence, the wind and wave directions are generally reasonably aligned.

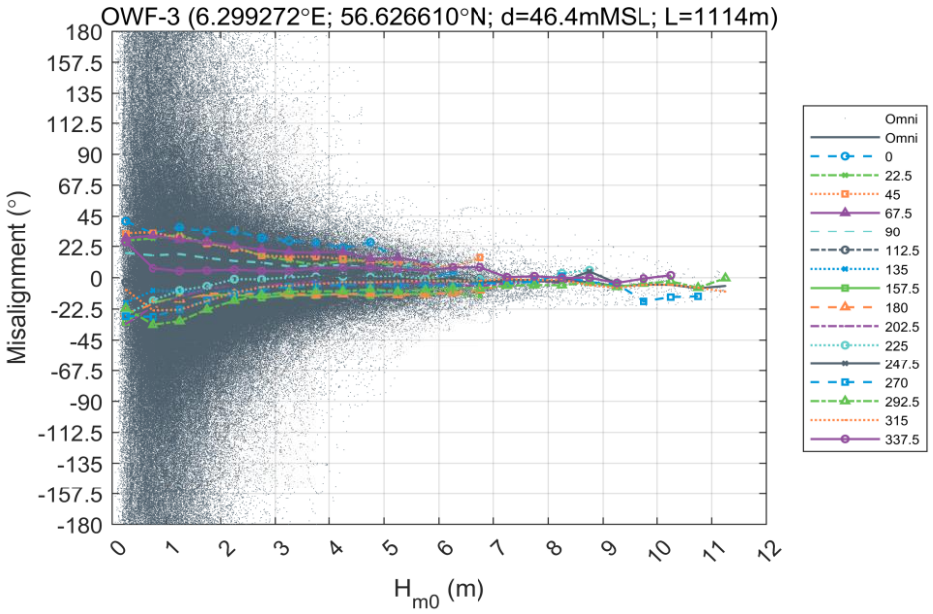

Figure 6.13 Wind-wave misalignment vs. H_{m0} at OWF-3

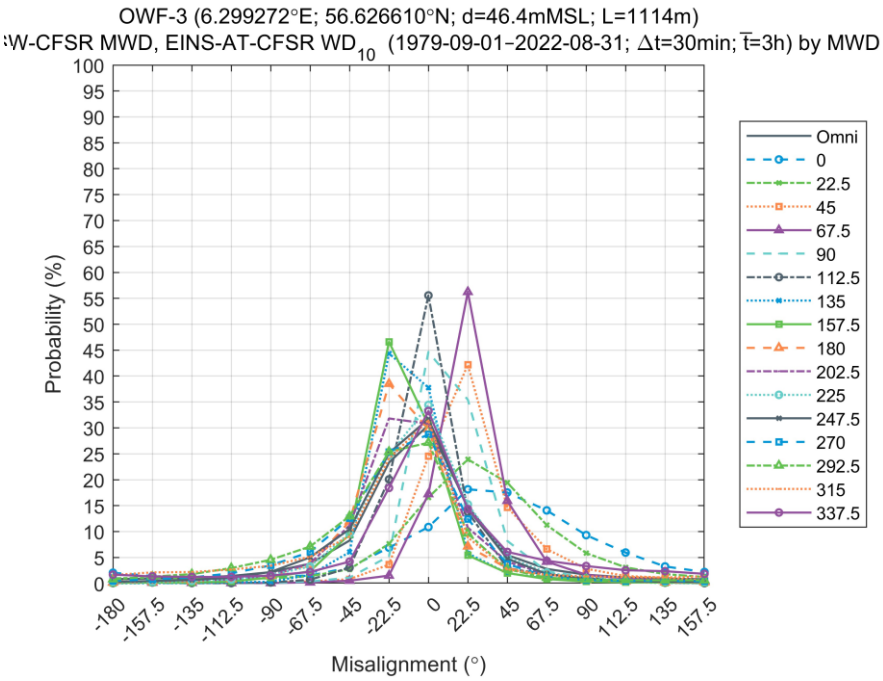

Figure 6.14 Probability of wind-wave misalignment per direction at OWF-3

6.1.8 Swell waves

This section presents a qualitative assessment of wind-sea and swell waves. Figure 6.1 presents time series of the total, wind-sea, and swell partition of H_{m0} at OWF-3, and Figure 6.15 presents a scatter plot of $H_{m0,Swell}$ vs H_{m0}. The figures show a predominance of wind-sea for the higher sea states.

Figure 6.16 present the average ratio of wind-sea to total energy (blue) and swell to total energy (orange), (the energy being proportional to the square of H_{m0}). For the lower sea states (H_{m0} < 2.5 m, which occurs ~75% of the time) the swell partition is responsible for more than half (50-80%) of the total wave energy, while for moderate sea states (2.5 m < H_{m0} < 7.0 m, which occurs ~25% of the time) the wind-sea partition is responsible for the majority (50-90%) of the energy.

For the very highest sea states (H_{m0} > 7.0 m, which occurs <0.3% of the time), the swell partition constitutes less than 15% of the total energy. Such quantification obviously depends on the chosen separation criterion between wind-sea and swell (in this case the wave-age, see Section 5.1 of [14]). The wave-age criteria define the part of the 2D wave spectrum where the speed and direction of wind and waves are aligned as wind-sea, and the remainder of the spectrum as swell.

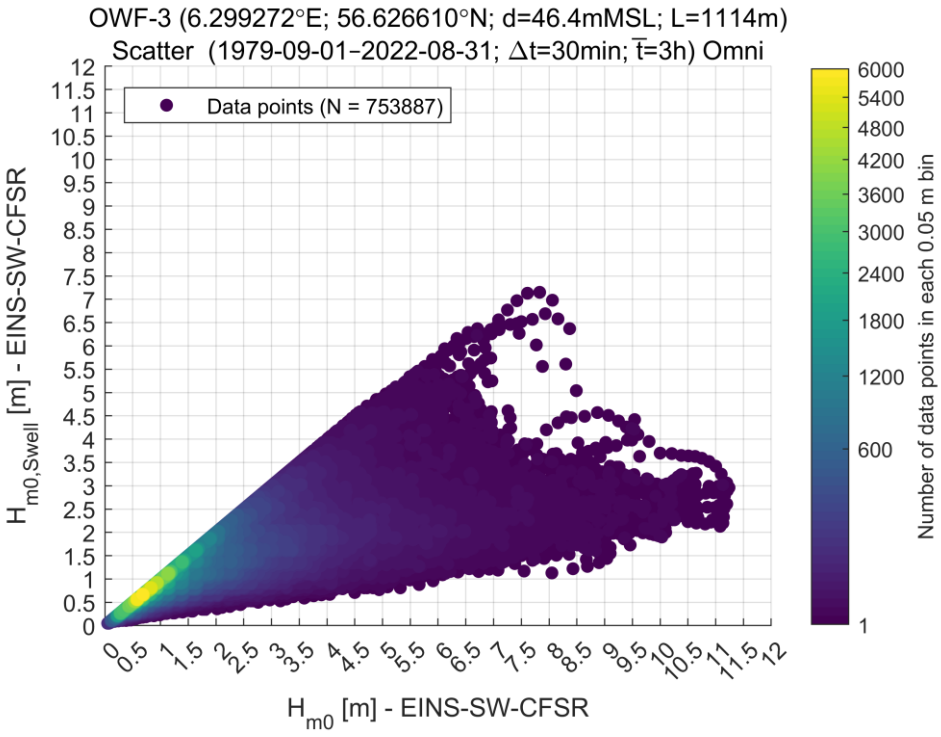

Figure 6.15 Scatter plot of $H_{m0,Swell}$ vs H_{m0} at OWF-3

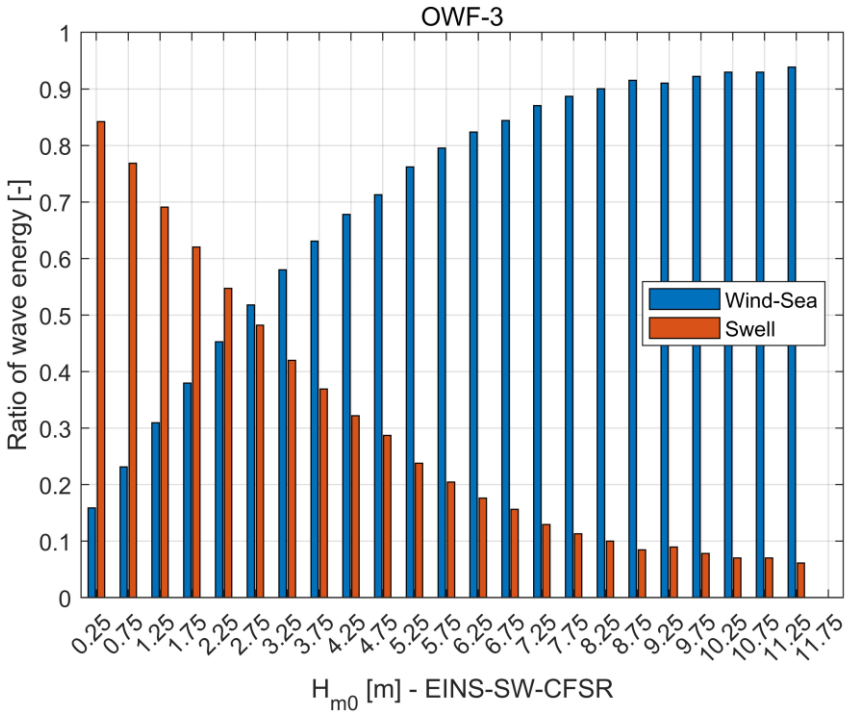

Figure 6.16 Average ratio of wind-sea to total energy (blue) and swell to total energy (orange) vs. H_{m0} (total) at OWF-3

6.1.9 Assessment of wave spectra

Assessment of wave spectra is addressed in Part A, [15]. For moderate and severe sea states, H_{m0} > 1.5 m, the spectrum is often single peaked and can be well represented by a JONSWAP spectrum. According to IEC-61400-3-1 [6], Section 6.4.4.2 Assessment of normal wave conditions: '*There is no requirement for assessment of site-specific wave spectra and directional spreading and the standard formulations provided in ISO 19901-1 may be assumed.*'. However, ISO [16] does not provide precise recommendation on the JONSWAP gamma values, and hence guidance of gamma is recommended to be adopted from Section 3.5.5 of DNV [5], i.e. defining γ based on T_p and H_{m0}. For low sea states, H_{m0} < 1.5m, the spectra are often bi-modal, and should be represented by a JONSWAP spectrum for each of the wind-sea and swell partitions separately.

6.1.10 Maps of mean H_{m0}

Figure 6.17 and Figure 6.18 presents maps across the EINS OWF area of the weighted mean significant wave height, $\overline{H_{m0}}$, calculated as follows.

$$\overline{H_{m0}} = \left[\frac{1}{N}\sum_{i=1}^{N} {H_{m0}}_i^{\,m}\right]^{\frac{1}{m}} \quad \textbf{(6.1)}$$

where $m = (1,2)$ is the power coefficient, and N is the total number of hindcast data points (m = 1 is the mean H_{m0}, while m = 2 is the mean wave energy). There is little variation across EINS OWF area with $\overline{H_{m0,m=1}}$ of about 1.95 m.

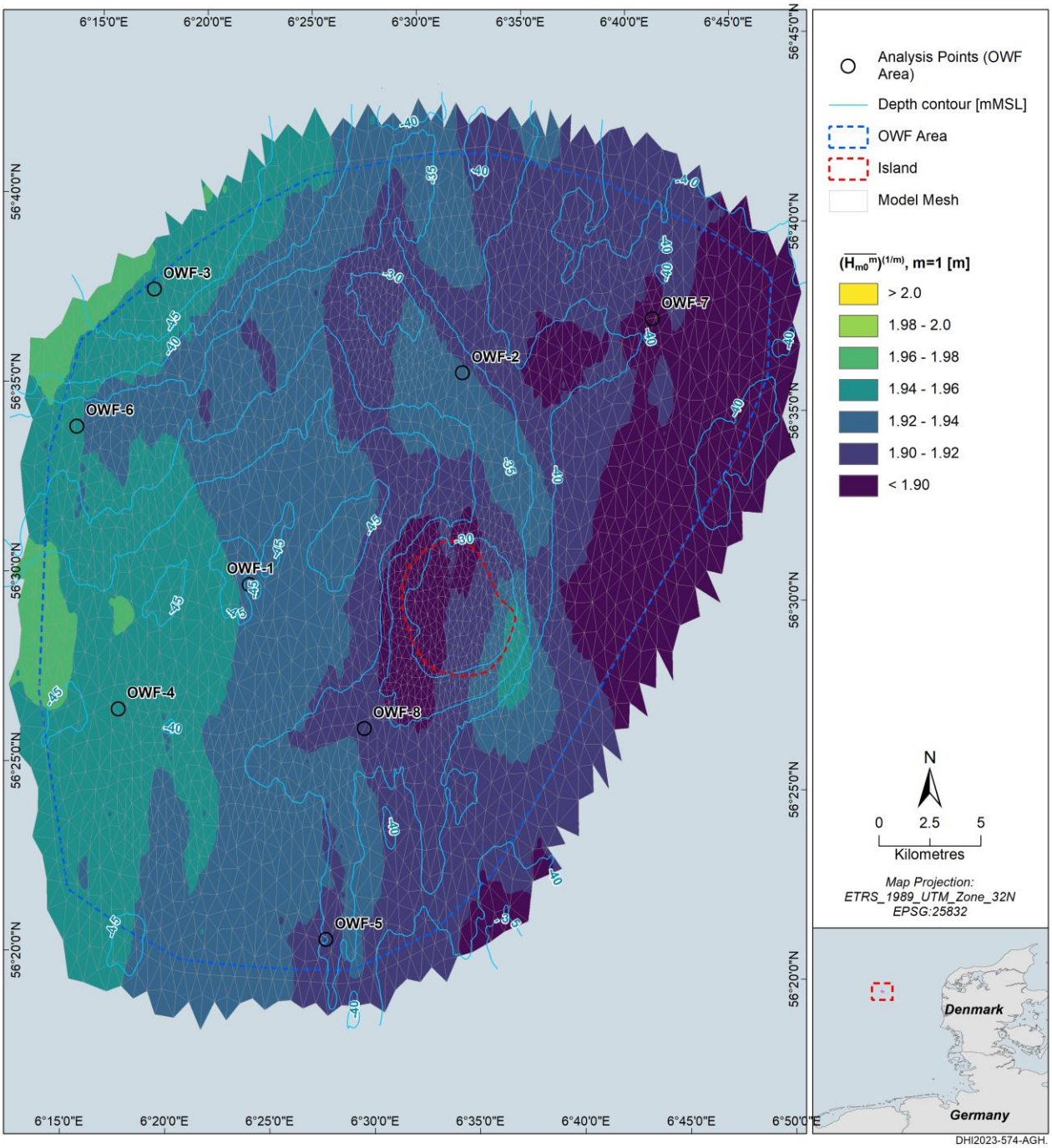

Figure 6.17 Spatial variation of $\overline{H_{m0}}$ across the EINS OWF area
The colour map shows the wave height, and the contours show water depth.

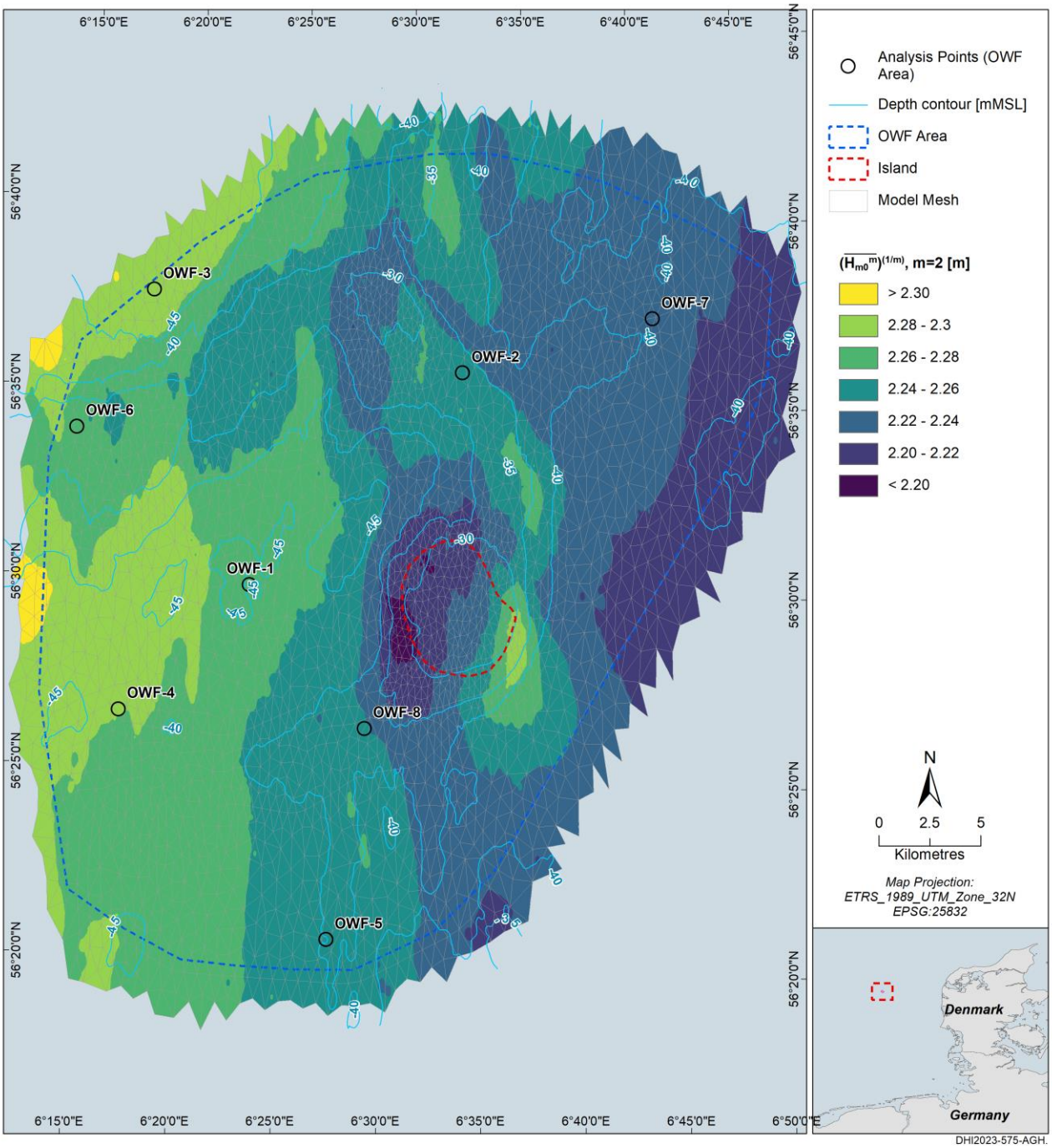

Figure 6.18 Spatial variation of $\sqrt{\overline{Hm0^2}}$ across the EINS OWF area

The colour map shows the wave energy, and the contours show water depth.

6.2 Extreme wave conditions

Extreme wave conditions were established using Traditional Extreme Value Analysis (T-EVA) following the methodology and settings derived and described in Appendix B: Sensitivity of T-EVA to Distribution, Threshold, and Fitting, and Appendix C: T-EVA – Traditional EVA.

For waves the 2-p Weibull distribution fitted by least-square to the 129 (3x43) peak events separated by at least 36 hours was applied.

For H_{max}, the Glukhovskiy short-term distribution is used, whereas for C_{max}, the Forristall distribution is used, as recommended in Section 6.2.1 Evaluation of short-term wave and crest distributions of Part A, [1].

The maximum wave crest is given relative to still water level, $C_{max,SWL}$, and relative to mean sea level, $C_{max,SWL}$. $C_{max,MSL}$ is derived by convoluting the short-term distribution with the simultaneous (residual) water level, as described in Section 13.3 of Appendix C: T-EVA – Traditional EVA.

The estimates of H_{max} , $C_{max,SWL}$, and $C_{max,MSL}$ have been truncated to account for wave breaking and limitations in accordance with Section 6.2.6.

6.2.1 Extreme H_{m0} (omni) and conditioned $T_{p|Hm0}$

Table 6.3 and Figure 6.19 present the extreme significant wave height, H_{m0}, at OWF-3. The fitted distribution aligns very well to the hindcast data points, also at the tail, and all events are within the confidence levels, which gives confidence in the derived values.

The conditioned T_p is estimated by fits to the upper 95%-tile of scatter plot given in Figure 6.9. Table 6.4 gives the conditioned peak wave period, $T_{p|Hm0}$.

The 50-year H_{m0} is 11.8 ± 0.9 m (the 2.5- and 97.5%-tile confidence levels) with conditioned T_p of 14.8 – 18.2 s.

Table 6.3 Extreme significant wave height, H_{m0}, at OWF-3

Return period, T_R [years]	H_{m0} [m]		
	2.5%-tile	Central estimate	97.5%-tile
1	8.0	8.2	8.5
5	9.5	9.9	10.2
10	10.0	10.5	11.0
50	11.0	11.8	12.7

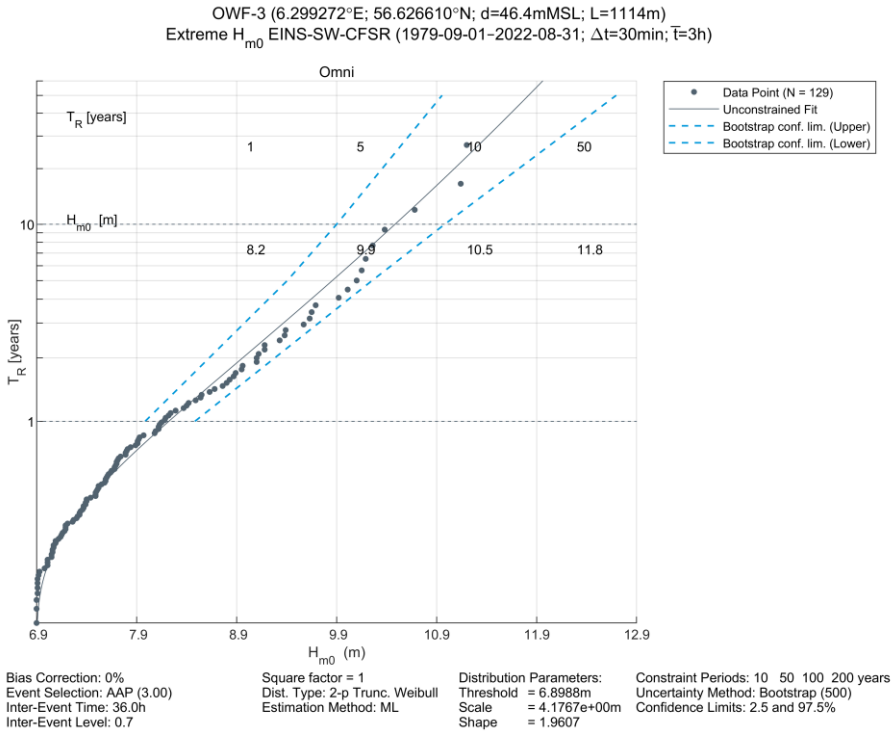

Figure 6.19 Extreme significant wave height, H_{m0} at OWF-3

Table 6.4 Conditioned peak wave period, $T_{p|Hm0}$, at OWF-3

Return period, T_R [years]	$T_{p\|Hm0}$ [s]		
	2.5%-tile	Central estimate	97.5%-tile
1	12.3	13.4	15.1
5	13.5	14.7	16.6
10	13.9	15.2	17.1
50	14.8	16.2	18.2

6.2.2 Extreme H_{max} (omni) and conditioned T_{Hmax}

Table 6.5 and Figure 6.20 presents the extreme maximum wave height, H_{max}, at OWF-3, while Table 6.6 gives the conditioned wave period, T_{Hmax}.

T_{Hmax} is taken as 0.9 x T_p as suggested in [5].

The 50-year H_{max} is 22.4 m (ranging from 20.7 to 23.7 m for the 2.5- and 97.5%-tile confidence levels) with conditioned T_{Hmax} of 13.3 – 16.4 s.

Table 6.5 Extreme maximum wave height, H_{max}, at OWF-3

Return period, T_R [years]	H_{max} [m]		
	2.5%-tile	Central estimate	97.5%-tile
1	15.0	15.4	15.8
5	17.5	18.4	19.1
10	18.6	19.6	20.4
50	20.7	22.4	23.7

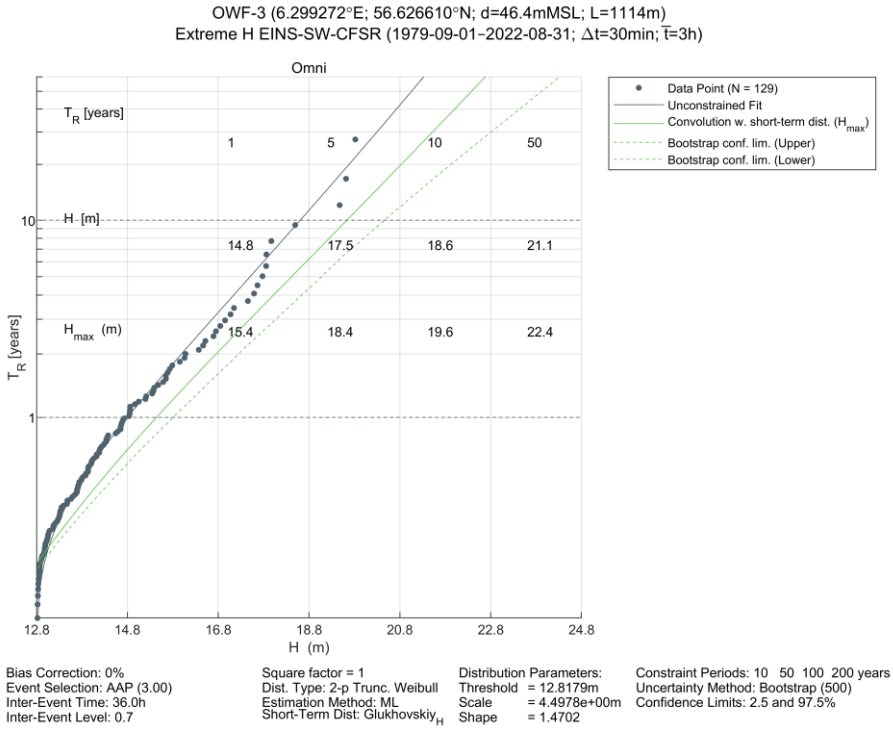

Figure 6.20 Extreme maximum wave height, H_{max}, at OWF-3
The grey line is the long-term distribution fitted to H_{max} of the peak hindcast data points (grey dots), while the green line is the long-term distribution convoluted (with the short-term distribution) over the entire storm, leading to H_{max}.

Table 6.6 Extreme conditioned wave period, T_{Hmax}, at OWF-3

Return period, T_R [years]	T_{Hmax} [s]		
	2.5%-tile	Central estimate	97.5%-tile
1	11.1	12.1	13.6
5	12.1	13.3	14.9
10	12.5	13.7	15.4
50	13.3	14.6	16.4

6.2.3 Extreme C_{max} (omni) relative to SWL

Table 6.7 and Figure 6.21 presents the extreme maximum wave crest to SWL, $C_{max,SWL}$, at OWF-3.

The 50-year $C_{max,SWL}$ is 14.4 ±1.3 m (the 2.5- and 97.5%-tile confidence levels).

Table 6.7 Extreme maximum wave crest to SWL, $C_{max,SWL}$, at OWF-3

Return period, T_R [years]	$C_{max,SWL}$ [mSWL]		
	2.5%-tile	Central estimate	97.5%-tile
1	9.1	9.4	9.6
5	11.0	11.5	12.0
10	11.7	12.4	13.0
50	13.1	14.4	15.7

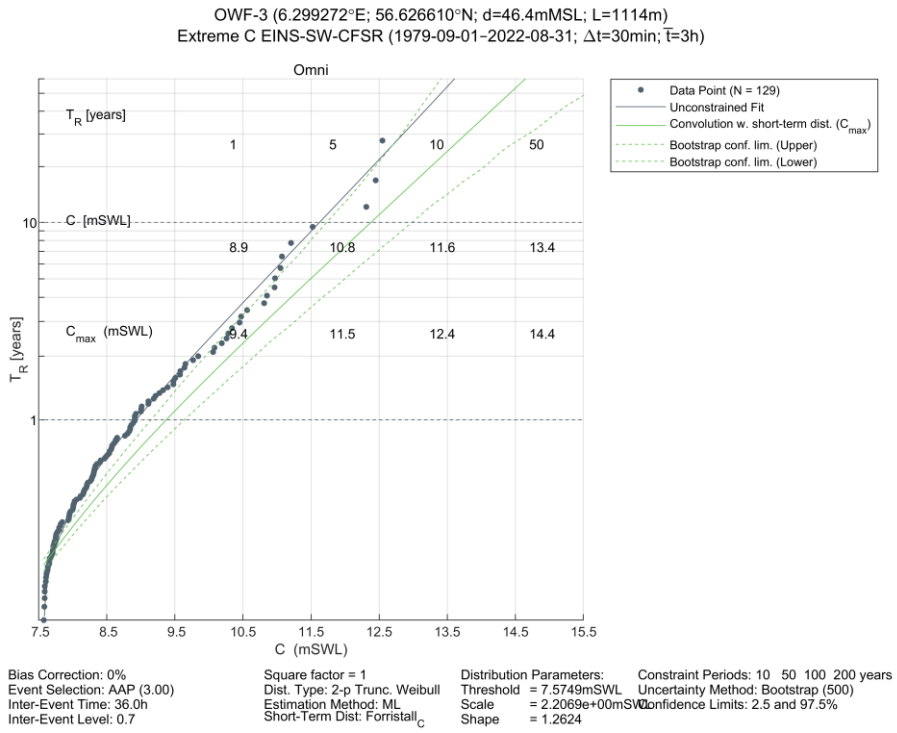

Figure 6.21 Extreme maximum wave crest to SWL, $C_{max,SWL}$, at OWF-3
The grey line is the long-term distribution fitted to C_{max} of the peak hindcast data points (grey dots), while the green line is the long-term distribution convoluted (with the short-term distribution) over the entire storm, leading to C_{max}.

6.2.4 Extreme C_{max} (omni) relative to MSL

Table 6.8 and Figure 6.22 presents the extreme maximum wave crest to MSL, $C_{max,MSL}$, at OWF-3.

The 50-year $C_{max,MSL}$ is 15.6 mMSL (ranging from 14.2 to 17.0 mMSL for the 2.5- and 97.5%-tile confidence levels).

The difference between $C_{max,SWL}$ and $C_{max,MSL}$, is 0.6 - 1.2 m, which is in line with the water level associated with high H_{m0} cf. scatter plot Figure 6.11.

Table 6.8 Extreme maximum wave crest to MSL, $C_{max,MSL}$, at OWF-3

Return period, T_R [years]	$C_{max,SWL}$ [mMSL]		
	2.5%-tile	Central estimate	97.5%-tile
1	9.8	10.0	10.3
5	11.7	12.3	12.8
10	12.5	13.3	14.0
50	14.2	15.6	17.0

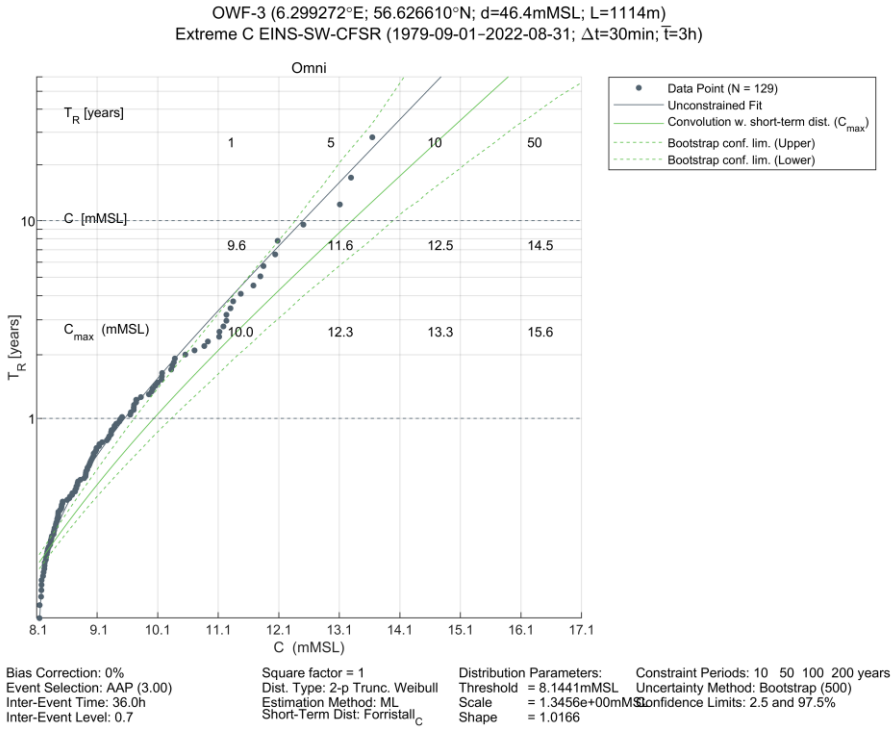

Figure 6.22 Extreme maximum wave crest to MSL, $C_{max,MSL}$, at OWF-3
The grey line is the long-term distribution fitted to C_{max} of the peak hindcast data points (grey dots), while the green line is the long-term distribution convoluted (with the short-term distribution) over the entire storm, leading to C_{max}.

6.2.5 Maps of extreme H_{m0}

Figure 6.23 - Figure 6.24 presents maps of extreme H_{m0} across EINS OWF area for return periods of 1 and 50 years based on traditional extreme value analysis at each mesh element. The maximum 50-yr H_{m0} varies within 11.4 ±1.0 m across the site.

Note: The values within the Island area (red dashed line) differ slightly from the values in Part B, [7], which are scaled according to J-EVA).

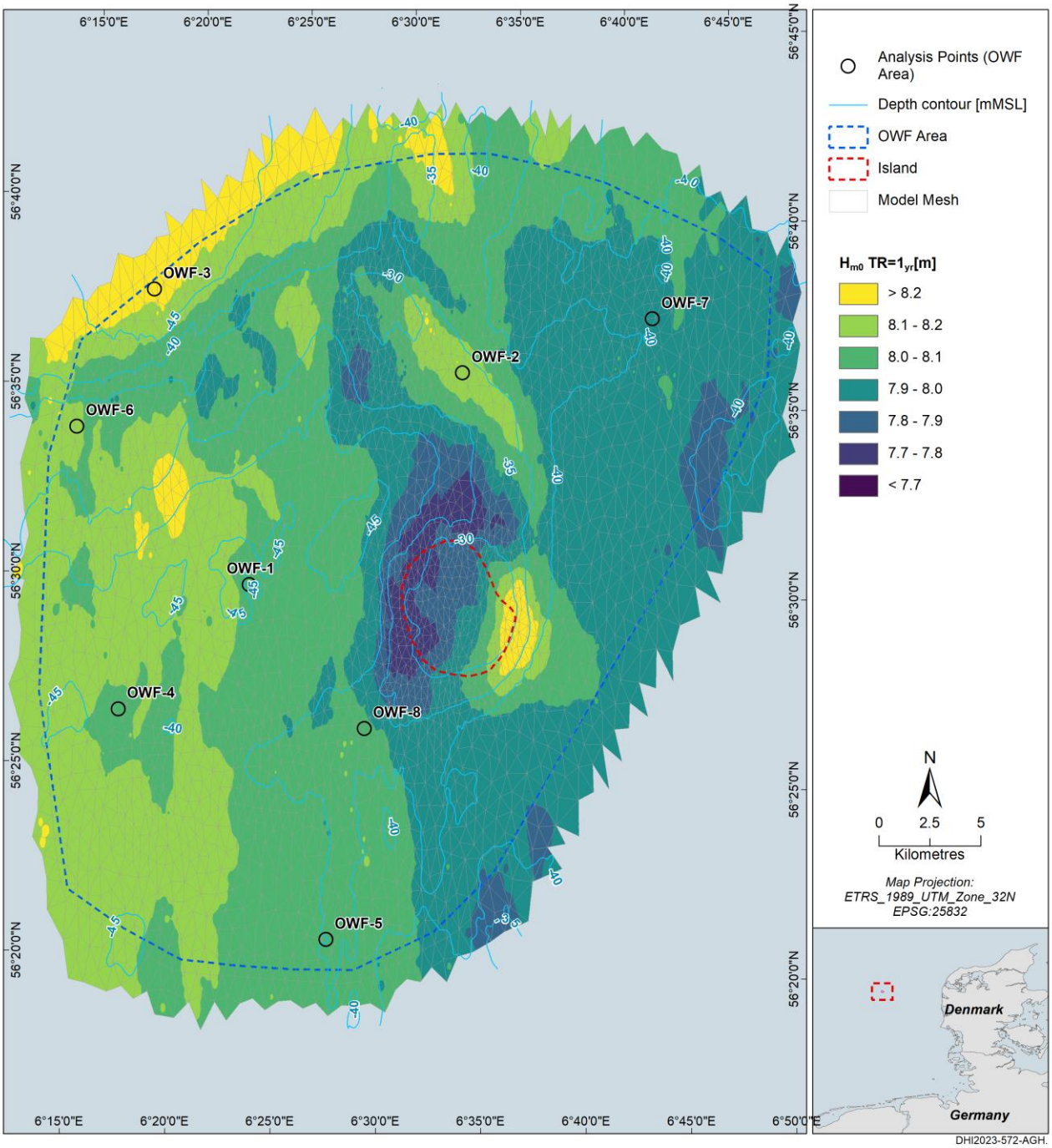

Figure 6.23 Spatial variation across EINS OWF area of H_{m0} speed for return period of 1 year. The colour map shows the wave height, and the contours shows water depth.

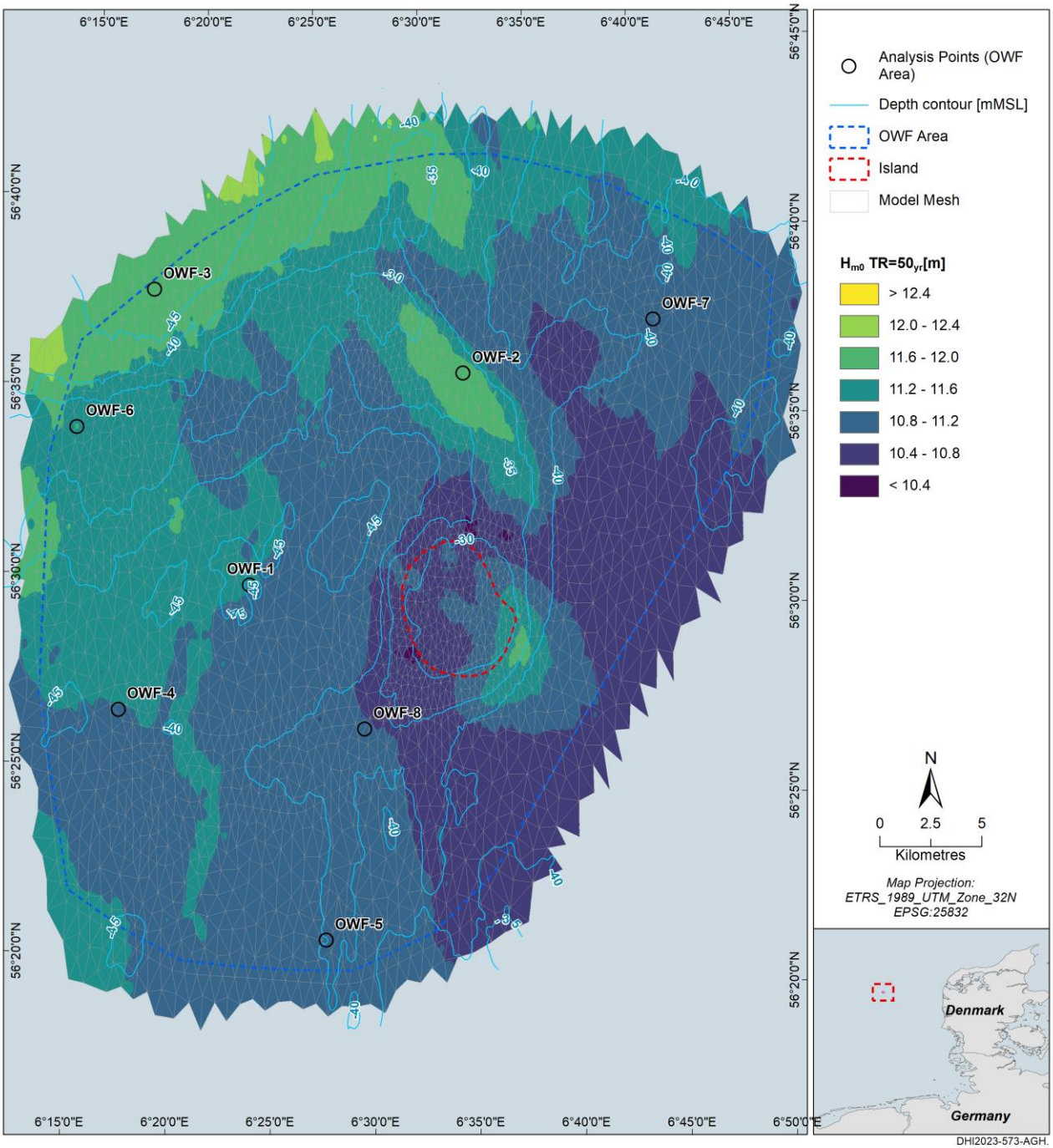

Figure 6.24 Spatial variation across EINS OWF area of H_{m0} speed for return period of 50 years. The colour map shows the wave height, and the contours shows water depth.

6.2.6 Wave breaking and limitations

The extreme H_{max} (Table 6.5) and C_{max} (Table 6.7) were derived following the Glukhovskiy and the Forristall short-term distributions respectively. The extreme distribution of H_{m0} (see Figure 6.19) did not indicate any upper limit. However, in practice, the highest waves are limited by the wave height to water depth ratio or wave steepness (height to length ratio). The water depth and wave periods of extreme sea states at EINS are such that shoaling is non-negligible. This means that the average wave steepness will increase and consequently that the probability of wave breaking will increase.

This section aims to address the occurrence/likelihood of wave breaking and to quantify the limiting individual wave height and wave crest conditions. This is sought by evaluating the magnitude and range of the individual wave period conditioned on H_{max}, T_{Hmax}, and by visiting the below common wave breaking criteria, followed by final recommendations on wave breaking and limitations. IEC-61400-3-1 [6], Section B.4 Breaking waves, concerns shallow water (Eq. B.27), and the breaking wave height formulation by Goda (Eq. B.28) concerns the surf zone (albeit it is sometimes used more generally). The EINS OWF area is not in shallow water nor in the surf zone, and hence guidance on wave limitations (relevant for steep and offshore waves) has been established from DNV [5] and other sources.

- DNV RP-C205, [5] – Steepness-induced breaking (regular waves)
- DNV RP-C205, [5] – Depth-induced breaking (shallow water)
- Fenton, [17, 18] – Stream Function (monochromatic wave on a flat seabed)
- Paulsen, [19] – Steepness and non-linear crest height to water depth ratio

Individual wave period conditioned on H_{max}, T_{Hmax}

The individual wave period conditioned on H_{max}, T_{Hmax}, is fundamental for the steepness-induced breaking. The period will vary because of varying sea state characteristics (variability of T_p given H_{m0}) but also because of the randomness of the sea state itself. The variability of T_{Hmax} against H_{max} is assessed using the following two approaches/datasets and comparing to DNV RP-C205.

1. Figure 6.26: Scatter plot of measured T_{Hmax} vs. H_{max} at EINS-Island (Mini 1), and fit to values above $H_{max,95\%}$.
2. Figure 6.27: Linear simulations of the surface elevation based on modelled spectra and zero-crossing at EINS-3.

According to Section 3.7.4 in DNV RP-C205, [5], the most probable T_{Hmax} to be used in conjunction with long term extreme wave height H_{max}, may be taken as given by Eq. (6.2), or alternatively Eq. (6.3). T_{Hmax} used in conjunction with H_{100} should be varied in the range given by Eq. (6.4).

$$T_{Hmax} = 0.9 \cdot T_p \quad \textbf{(6.2)}$$

$$T_{Hmax} = a \cdot H_{max}^{b} \quad (6.3)$$

where a and b are empirical coefficients. For the southern part of the Norwegian Continental Shelf, a = 2.94, and b = 0.5 may be applied.

$$2.55 \cdot \sqrt{H_{100}} \leq T_{Hmax} \leq 3.32 \cdot \sqrt{H_{100}} \quad (6.4)$$

Where H_{100} is the 100-year individual wave height, $H_{max,100yr}$

The highest measured individual wave was during storm Malik with H_{max} of 19 m and T_{Hmax} of 14.6 s, see Figure 6.25 (left). The second highest measured wave had H_{max} of 17 m and T_{Hmax} of 14.3 s on 2021-12-01, but it is likely an erroneous recording, and was removed from the analysis, see Figure 6.25 (right).

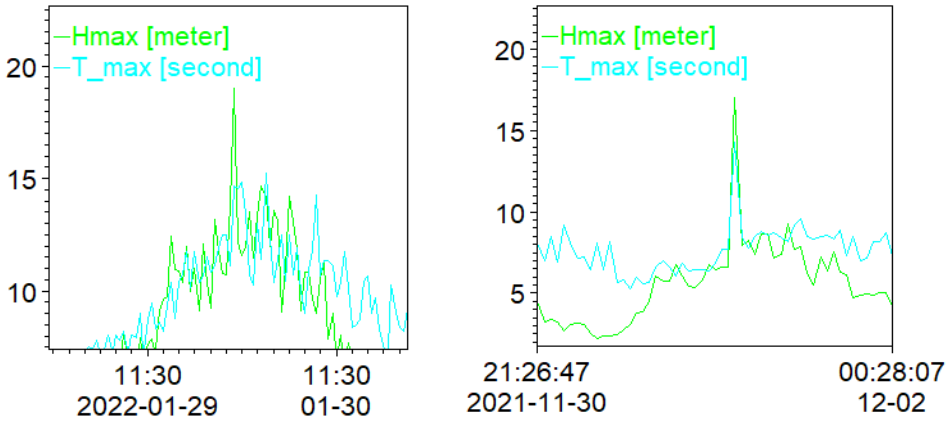

Figure 6.25 Time series of the two highest measured H_{max} (and T_{Hmax}). Left: Storm Malik. Right: is Likely an erroneous recording.

The above approaches were evaluated using the 50%-tile $T_{p|Hm0,100yr}$ = 15.7 s and $H_{max,100yr}$ = 18.8 m as estimated at EINS-3, a point close to the EINS Island measurement station, see coordinates in Table 7.1 (shown by orange lines in Figure 6.26 - Figure 6.27).

The results show a reasonable agreement between the measured and Eq. (6.4) (DNV by T_p) that is applied in this study, albeit the latter is slightly higher. Eq. (6.5) (DNV by H_{max}) gives lower $T_{Hmax,100yr}$, while that from modelled spectra is the lowest:

- Eq. (6.4) (DNV by T_p): T_{Hmax} = 14.1 s
- Eq. (6.5) (DNV by H_{max}): T_{Hmax} = 12.7 s
- Eq. (6.6) (DNV range): T_{Hmax} = [11.1 – 14.4] s
- Figure 6.26 (**based on measured fit**): **T_{Hmax} = 13.7 s**
- Figure 6.27 (from modelled spectra): T_{Hmax} = 12.9 s

All the central estimates are within the DNV range given by Eq. (6.6), but the range of the 2.5 and 97.5%-tiles of Eq. (6.4) (DNV by T_p) and the 2.5 and 97.5%-tiles of the measurements are both larger than the DNV range.

The DNV range is ±1.7 s (i.e. a factor 3.32/2.94 = 1.13), which agree roughly with the corresponding ~87/13%-tiles of the measurements (Figure 6.32) and models (Figure 6.33). Such range (factor of 1.13) of the wave period could be a (upper bound) candidate as input to steepness-based breaking criteria.

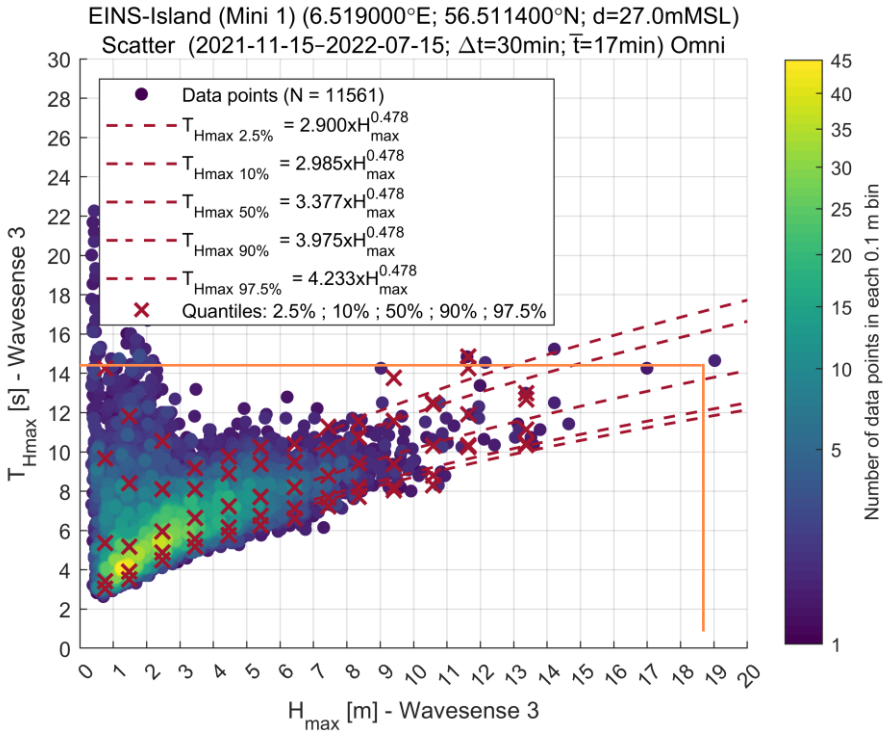

Figure 6.26 Scatter plot of <u>measured</u> T_{Hmax} vs. H_{max} at EINS-Island (Mini 1)
Orange line: $H_{max,100yr}$ = 18.8 m.

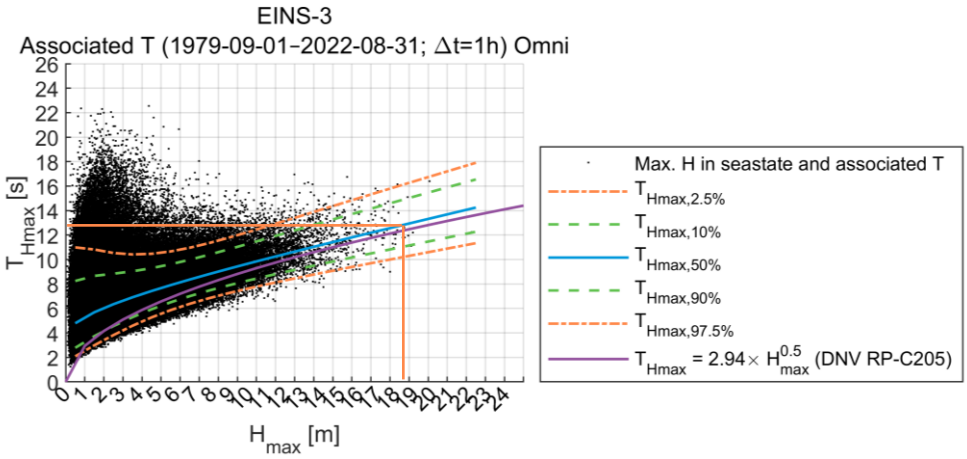

Figure 6.27 Scatter plot of <u>modelled</u> T_{Hmax} vs. H_{max} at EINS-3
Orange line: $H_{max,100yr}$ = 18.8 m.

DNV RP-C205, [5] – Steepness-induced breaking (regular waves)

A commonly adopted criterion for steepness-induced wave breaking limit is given in Section 3.4.6.1 of DNV RP-C205, [5], see Eq. (6.5) and Figure 6.28. This criterion is applicable to regular waves on a plane seabed.

However, the extreme waves at EINS are not regular, and it is well known that irregular and spread (short-crested) sea states can support higher waves, hence such method should only be used with adequate mitigation measures.

$$\frac{H_b}{\lambda} = 0.142 \cdot \tanh\frac{2\pi d}{\lambda} \quad \textbf{(6.5)}$$

Where λ is the wavelength corresponding to water depth d. In deep water, the breaking wave limit corresponds to a maximum steepness of $S_{max} = H_b/\lambda = 1/7$.

DNV RP-C205, [5] – Depth-induced breaking (shallow water)

A common criterion for depth-induced wave breaking limit is given in Section 3.4.6.2 of DNV RP-C205, [5], and Section B4 in IEC-61400-3-1, [6], see Eq. (6.6) and Figure 6.28. This criterion is applicable in shallow water (d < 1/20 λ).

However, the water depths at EINS are not shallow according to the common definition of d < 1/20 λ, albeit the extreme waves will certainly 'feel' the seabed, hence such method should only be used for reference at EINS.

$$H_{max,lim} = 0.78 \cdot \mathrm{d} \quad \textbf{(6.6)}$$

A (potentially cautious) approach would be to use the 97.5%-tile of the conditioned water level to $H_{m0,}$ $WL_{tot|Hm0,97.5\%}$, added to the water depth, d.

The wave crest in shallow water can be capped using the same criterion by anticipating a ratio of 0.85 between the wave crest and wave height (based on stream function, see Table 6.9).

Fenton, [17, 18] – Stream Function (monochromatic wave on a flat seabed)

In this section, Fenton's stream function theory was applied to quantify the limiting wave height (H_m), and wave crest (C_m), of a monochromatic wave given the total water depth (d) and the wavelength (λ) (or wave period), [17, 18], see Eq. (6.7). Using stream function theory means that C_m and H_m occur in the same individual wave, which is not necessarily the case in real sea states.

$$\frac{H_m}{d} = \frac{0.141063\frac{\lambda}{d} + 0.0095721\left(\frac{\lambda}{d}\right)^2 + 0.0077829\left(\frac{\lambda}{d}\right)^3}{1 + 0.0788340\frac{\lambda}{d} + 0.0317567\left(\frac{\lambda}{d}\right)^2 + 0.0093407\left(\frac{\lambda}{d}\right)^3} \quad \textbf{(6.7)}$$

Figure 6.28 shows common limiting wave heights of regular wave theory, along with that of stream function; the figure is adopted from IEC-61400-3-1, [6].

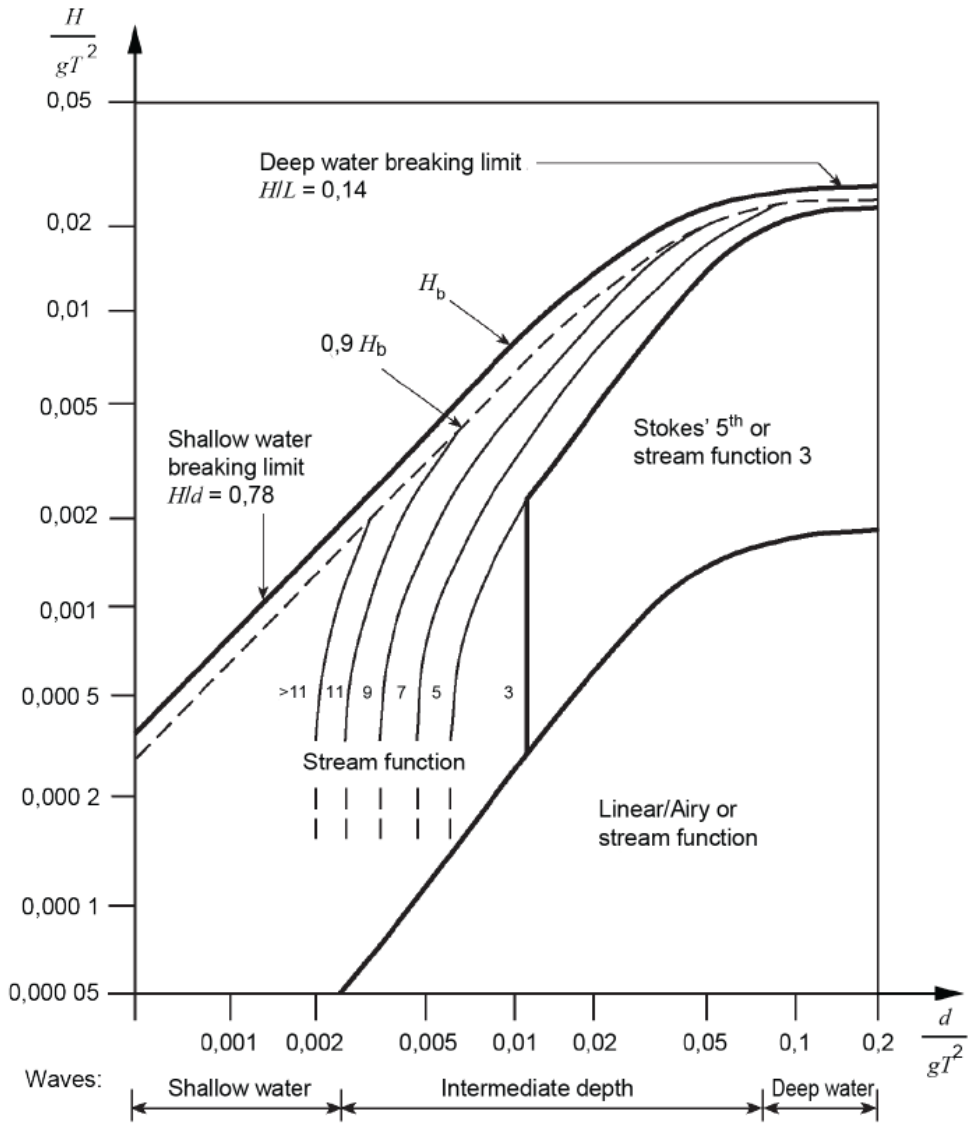

Figure 6.28 Limiting wave heights of regular wave theory; from [6]

The water depth is taken as the mean water depth plus the 97.5%-tile of the total water level conditional on H_{m0} ($WL_{tot|Hm0,97.5\%}$), and the wave period is taken as the 97.5%-tile wave period conditional on H_{max} ($T_{Hmax,97.5\%}$). These inputs are conservative in the sense that lower values (shallower water or shorter wave period) would lead to lower limiting wave height. Figure 6.29 shows the limiting (50-yr) stream function wave at EINS-3.

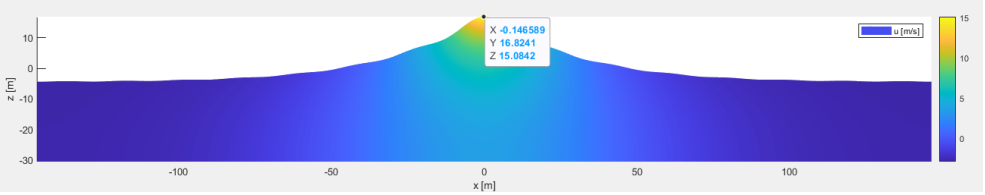

Figure 6.29 Limiting (50-yr) stream function wave at EINS-3

Table 6.9 summarises the limiting (50-yr) wave height (H_m) and wave crest (C_m) according to stream function at EINS-3 using the upper bound $WL_{tot|Hm0,97.5\%r}$ and $T_{Hmax,97.5\%}$.

At EINS, the stream function suggests a limiting wave height and wave crest in between the estimated 100 and 1.000-yr H_{max} and C_{max} values. This means that according to stream function theory, the estimated 1,000-yr H_{max} and C_{max} cannot exist, and it can be argued that the H_{max} and C_{max} values for this and higher return periods may be reduced.

However, it is noted that while stream function can represent very non-linear (steep) waves, it does not account for directional spreading, opposing current or uneven wave shape (the wave front being steeper than the back of the wave). Directional spreading can lead to higher waves (compared to unidirectional waves), and thus a stream function wave cannot be considered an ultimate upper limit. Nevertheless, it is very rare that those values would be exceeded, considering the rather conservative input of the 97.5%-tile conditional water level and wave period,

In practical engineering applications, directional spreading is sometimes compensated for by the use of a 'directional spreading factor' (to compensate for not all energy of the wave spectrum travelling in the same direction).

Table 6.9 Limiting wave and crest of stream function at EINS-3 conditioned on 97.5%-tile – 50-yr

Name	d [mMSL]	$WL_{tot\|Hm0,97.5\%}$ [mMSL]	$T_{Hmax,97.5\%}$ [s]	$H_{max,Glukhoskiy}$ [m]	H_m [m]	$C_{max,Forristall}$ [mSWL]	C_m [mSWL]
EINS-3	28.9	1.5	16.7	18.2	**21.0**	13.0	**16.8**

Paulsen, [19] – Steepness and non-linear crest height to water depth ratio

An alternative method of estimating the breaking (probability) is given by Paulsen et.al., [19]. They quantify the probability that a random wave in a sea state is breaking via the sea state steepness and the non-linear crest height to water depth ratio.

The sea state steepness is calculated based on the linear dispersion relation, T_{01}, and H_{m0} as $R = k_{01}H_{m0}$, and the wave is breaking when the non-linear crest height exceeds a limit α given by Eq. (6.8).

$$\alpha = \min\left(\frac{\beta_0\left(1+\frac{1}{2}\beta_0\right)}{k_{01}}, \alpha_0 h\right)$$
$$\beta_0 \in [0.3; 0.5] \quad (6.8)$$
$$\alpha_0 = 0.4$$
h is the water depth including tide and surge

Figure 6.30 compares this non-breaking wave crest criterion to the extreme wave crests at a location in the North Sea of similar water depth to EINS (~26 mMSL). The figure shows the Forristall crest to still water level, η, against the significant wave height, H_{m0} (grey line) for return periods of 1 to 10,000 years.

This is compared to the depth-limited crest ($0.4 \times h$), Eq. (6.8), at which all crests are assumed to break (blue line). The slight increase for increasing H_{m0} is caused by the increase in surge for increasing return period. It is observed that waves with crests above ~11 m are breaking based on this criterion.

The green and oranges lines show the limits of the steepness-based criterion. The wave crests lie in between these limits but approaches the upper limit for increasing return period. This is because the steepness of the sea state is increasing for increasing return period. This assessment supports that breaking is to be expected at the EINS site.

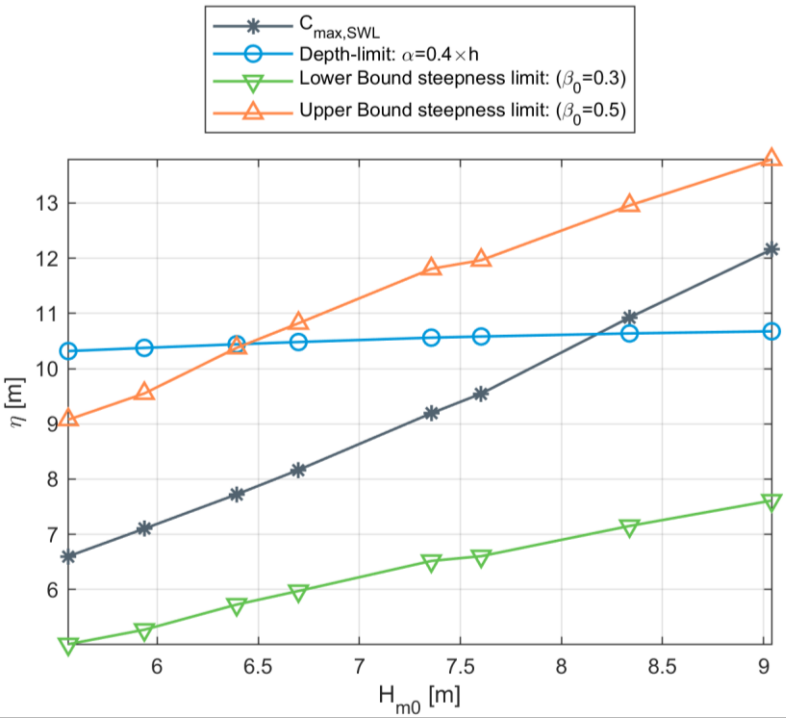

Figure 6.30 Maximum non-breaking crest height according to Paulsen et.al., [19], compared to the wave crests at a location in the North Sea

Recommendations on wave breaking

All the wave breaking, limitation and probability approaches described above are prone to some general simplifications and somewhat crude assumptions about individual waves in extreme sea states. However, there is consensus that the higher waves will break, and as such it is recommended that wave breaking, and related loads, are accounted for in the design of EINS.

Concerning breaker type, we do not recommend following the procedure outlined in e.g. IEC-61400-3-1 Annex B, [6]. This approach classifies wave breaking type as function of seabed slope and wave steepness. For most offshore sites in the North Sea, this will classify breaking waves as spilling, and no additional load to that of stream function theory would be accounted for.

Recommendations on wave limitations

The comparison of measured and modelled relation between H_{max} and T_{Hmax} demonstrated a reasonable agreement, and it showed that the estimated individual wave periods at EINS are slightly higher than the local measurements when based on the simple Eq. (6.4) (DNV by T_p).

Several of the wave limitation approaches suggest that the extreme sea states are prone to steepness- or depth-induced wave breaking. The former is dependent on which quantile of the wave period one considers. The DNV range for the 100-year return period, Eq. (6.6), corresponds to a factor of 1.13 times the central value of T_{Hmax}, which is thus a candidate for such range.

In conclusion, it is recommended to use the DNV steepness criteria, Eq. (6.5), with 1.13 times $T_{Hmax,50\%}$, and $WL_{Hm0,50\%}$ as input, to limit H_{max}. And to limit C_{max} accordingly using a ratio of 0.85 between the wave crest and the wave height.

Table 6.10 presents the recommended limits to H_{max} and C_{max} at EINS-3 for 50 years. The limiting H_{max} is higher than that of the stream function but lower than that of the DNV shallow water criteria, Eq. (6.6) for 50 years. The limiting values are estimated to be between the 1,000- and 10,000-year return period values.

It is noted that neither regular wave theory nor stream function accounts for directional spreading etc., which can lead to higher waves. However, using the steepness criteria with an upper bound T_{Hmax} is considered an optimized and pragmatic, but still safe, approach for the individual extreme waves at EINS.

Table 6.10 Recommended limits to H_{max} and C_{max} based on DNV steepness criteria, Eq. (6.7), with upper bound (UB) as 1.13 times the 50%-tile T_{Hmax}, and the 50%-tile $WL_{|Hm0}$ – 50-yr
Using a ratio of 0.85 between the C_{max} and H_{max} (based on stream function, see Table 6.9).

Name	d [mMSL]	$WL_{Hm0,50\%}$ [mMSL]	$1.13 \times T_{Hmax,50\%}$ [s]	$H_{max,Glukhovskiy}$ [m]	$H_{b,Steepness,UB}$ [m]	$H_{b,Shallow,97.5\%}$ [m] (=0.78 x WL)	$C_{b,Steepness,UB}$ [m] (=0.85 x H_b)
EINS-3	28.9	0.9	14.8	18.2	**21.9**	23.7	**18.6**

7 Other Atmospheric Conditions

This section presents analyses of other atmospheric conditions than wind.

Other atmospheric conditions concern air temperature, humidity, solar radiation, lightning, and visibility.

The spatial variation of these atmospheric conditions is minor at an offshore site with a relatively small extent (~60 x 40 km). Therefore, the conditions are analysed at one location only (one of those given in Table 7.1) and the conditions at this location are considered representative of the entire EINS OWF area.

Table 7.1 Coordinates and water depths of the EINS analysis points

#	Point Name (A-z)	Description	Longitude WGS84 [°E]	Latitude WGS84 [°N]	Depth, Survey [mMSL]	Depth, HD_{EINS} [mMSL]	Depth, SW_{EINS} [mMSL]
1	EINS-1	Shallowest	6.5714	56.5016	26.3	27.0	26.6
2	EINS-2	Max H_{m0}	6.5944	56.4894	28.9	29.1	29.1
3	EINS-3	Max CS_{tot}	6.5383	56.5172	28.8	28.9	28.9

7.1 Air temperature, humidity, and solar radiation

Annual and monthly statistics of modelled air temperature at 2 m above sea level (asl), relative humidity and downward solar radiation, based on CFSR, cf. Section 7.2 of Part A, [1], at analysis point EINS-1 (shallowest) are illustrated in Figure 7.1. The results are summarised in Table 7.2 to Table 7.4.

There is a clear seasonal variation for all three variables. Air temperature, relative humidity and solar radiation are larger during the summer months and lower during the winter months. There is also a clear delay of around ~1 month between highest solar radiation and, air temperature and relative humidity.

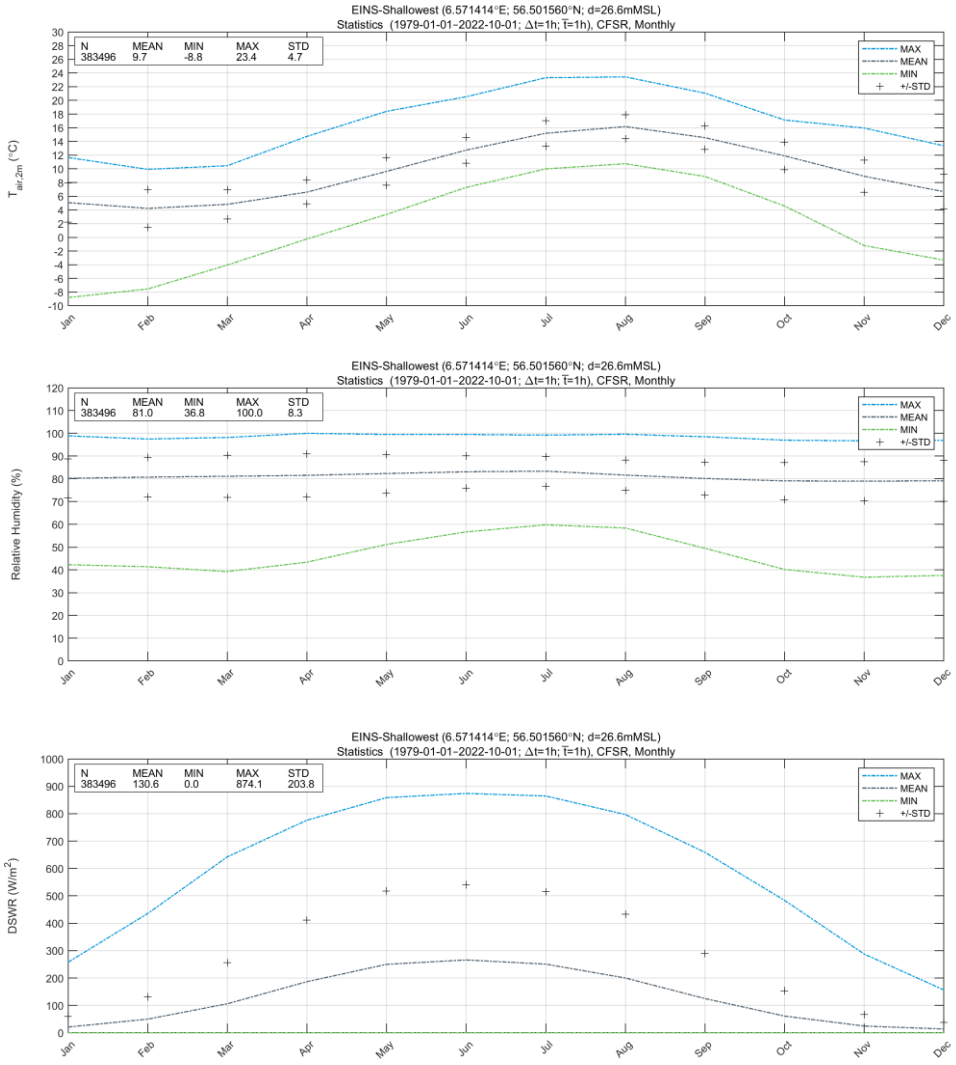

Figure 7.1 **Monthly statistics of air temperature at 2 m asl (top), relative humidity (centre), and downward solar radiation (bottom) at EINS-1 (shallowest)**

Table 7.2 Annual and monthly statistics for air temperature at 2 m asl at EINS-1 (shallowest) based on CFSR (1979-01-01 – 2022-10-01)

Air temperature at 2 m asl at EINS-1 (shallowest) [°C]						
Statistical		№ of data points	Mean	Min.	Max.	STD.
Annual		383,496	9.7	-8.8	23.4	4.7
Monthly	Jan.	32,735	5.1	-8.8	11.7	2.8
	Feb.	29,832	4.2	-7.5	9.9	2.7
	Mar.	32,736	4.8	-4.0	10.5	2.1
	Apr.	31,680	6.6	-0.2	14.7	1.8
	May	32,736	9.6	3.3	18.4	2.0
	Jun.	31,680	12.7	7.3	20.5	1.9
	Jul.	32,736	15.2	10.0	23.3	1.8
	Aug.	32,736	16.2	10.8	23.4	1.8
	Sep.	31,680	14.6	8.9	21.0	1.7
	Oct.	31,993	11.9	4.6	17.1	2.0
	Nov.	30,960	8.9	-1.2	16.0	2.4
	Dec.	31,992	6.7	-3.3	13.4	2.6

Table 7.3 Annual and monthly statistics for relative humidity at EINS-1 (shallowest) based on CFSR (1979-01-01 – 2022-10-01)

Relative humidity at EINS-1 (shallowest) [%]						
Statistical		№ of data points	Mean	Min.	Max.	STD.
Annual		383,496	81.0	36.8	100.0	8.3
Monthly	Jan.	32,735	80.3	42.3	98.9	8.6
	Feb.	29,832	80.8	41.4	97.5	8.7
	Mar.	32,736	81.1	39.3	98.2	9.3
	Apr.	31,680	81.6	43.4	100.0	9.5
	May	32,736	82.3	51.2	99.5	8.5
	Jun.	31,680	83.1	56.7	99.5	7.1
	Jul.	32,736	83.4	59.8	99.2	6.5
	Aug.	32,736	81.7	58.4	99.6	6.7
	Sep.	31,680	80.2	49.5	98.5	7.2
	Oct.	31,993	79.1	40.2	97.0	8.1
	Nov.	30,960	79.0	36.8	96.7	8.5
	Dec.	31,992	79.2	37.6	96.9	9.0

Table 7.4 Annual and monthly statistics for downward solar radiation at EINS-1 (shallowest) based on CFSR (1979-01-01 – 2022-10-01)

Downward solar radiation at EINS-1 (shallowest) [W/m^2]						
Statistical		№ of data points	Mean	Min.	Max.	STD.
Annual		383,496	130.6	0.0	874.1	203.8
Monthly	Jan.	32,735	21.1	0.0	257.7	38.6
	Feb.	29,832	50.0	0.0	435.6	82.1
	Mar.	32,736	106.1	0.0	642.4	150.1
	Apr.	31,680	186.7	0.0	776.3	224.8
	May	32,736	250.1	0.0	858.6	267.9
	Jun.	31,680	266.1	0.0	874.1	274.5
	Jul.	32,736	250.8	0.0	864.5	265.2
	Aug.	32,736	200.1	0.0	797.0	232.1
	Sep.	31,680	125.0	0.0	658.8	165.4
	Oct.	31,993	61.1	0.0	483.4	93.0
	Nov.	30,960	24.7	0.0	287.4	43.2
	Dec.	31,992	13.9	0.0	156.4	24.9

7.2 Lightning

Lightning data was obtained from the LIS/OTD Gridded Climatology dataset [20] from NASA's Global Hydrology Resource Center (GHRC), cf. Section 7.4 of Part A, [1]. Table 7.5 summarises the statistics of the HRFC (High Resolution Full Climatology), HRMC (High Resolution Monthly Climatology) and LRMTS (Low Resolution Monthly Time Series) datasets for the whole EINS OWF. Figure 7.2 and Figure 7.3 show the monthly and yearly variation of flash rates, based on the HRMC and LRMTS datasets, respectively. It should be noted that both HRMC and LRMTS contain extensive smoothing (see [21] for further results).It should be noted that both HRMC and LRMTS contain extensive smoothing (see [21] for further results). Therefore, the values are different from the HRFC dataset (discussed in the paragraph above). The results from HRMC and LRMTS presented here are only shown to demonstrate the monthly and yearly variations, therefore, it is recommended to use the HRFC data set. Based on the HRFC data set the mean flash rate at the EINS OWF is 0.285 fl/(km^2 yr), i.e. 7.81e^{-4} fl/(km^2 day). As it can be seen from the figures, the flash rate in June and September is, on average, higher than in other months.

Table 7.5 Statistics of flash rates at EINS

HRFC dataset: Mean annual flash rate. HRMC: Mean flash rate in middle of each month, with monthly smoothing. LRMTS: Monthly time series of flash rate, with smoothing.

Data set	Units	Grid [°]	Max	Min	Mean
HRFC	fl/(km^2·year)	0.5	---	---	0.285
HRMC	fl/(km^2·day)	0.5	0.004	0.0	0.001
LRMTS	fl/(km^2·day)	2.5	0.005	0.0	0.002

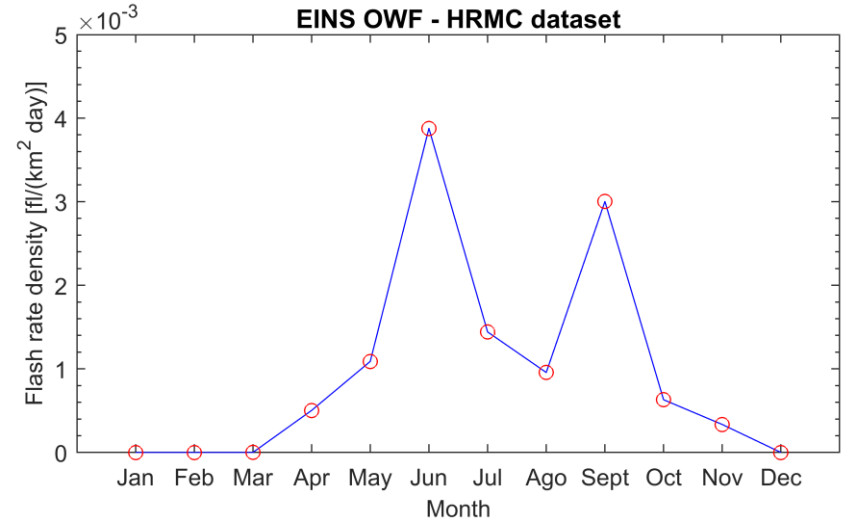

Figure 7.2 Monthly variation of flash rate at EINS area based on HRMC data for the period July 1995 to February 2000

Mean flash rate in middle of each month, with monthly smoothing

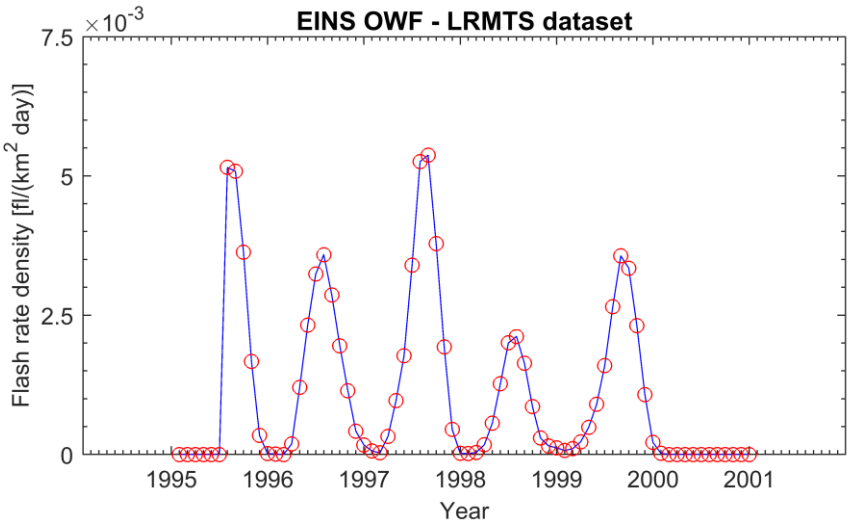

Figure 7.3 Combined monthly time series of flash rates at EINS based on LRMTS data for the period July 1995 to February 2000

Monthly time series of flash rate (weighted more toward LIS than other products)

7.3 Visibility

The visibility was derived from the air temperature at 2m height above sea surface, T_{2m}, and the relative humidity, RH, from CFSR, cf. Section 7.4 of Part A, [1], following the method described in [22], see (7.1). The dew point temperature, T_{dp}, was approximated using the Magnus formulae[3]. The visibility was capped at 50 km.

$$Visibility\ [\mathrm{km}] = 1.609 \times 6000 \times \frac{T_{2m} - T_{dp}}{RH^{1.75}} \qquad (7.1)$$

Figure 7.4 shows time series of T_{2m}, RH and Visibility, and Figure 7.5 presents the probability of visibility at EINS-2. The visibility is most frequently between 4 and 20 km, with a 50%-tile of 12.8 km.

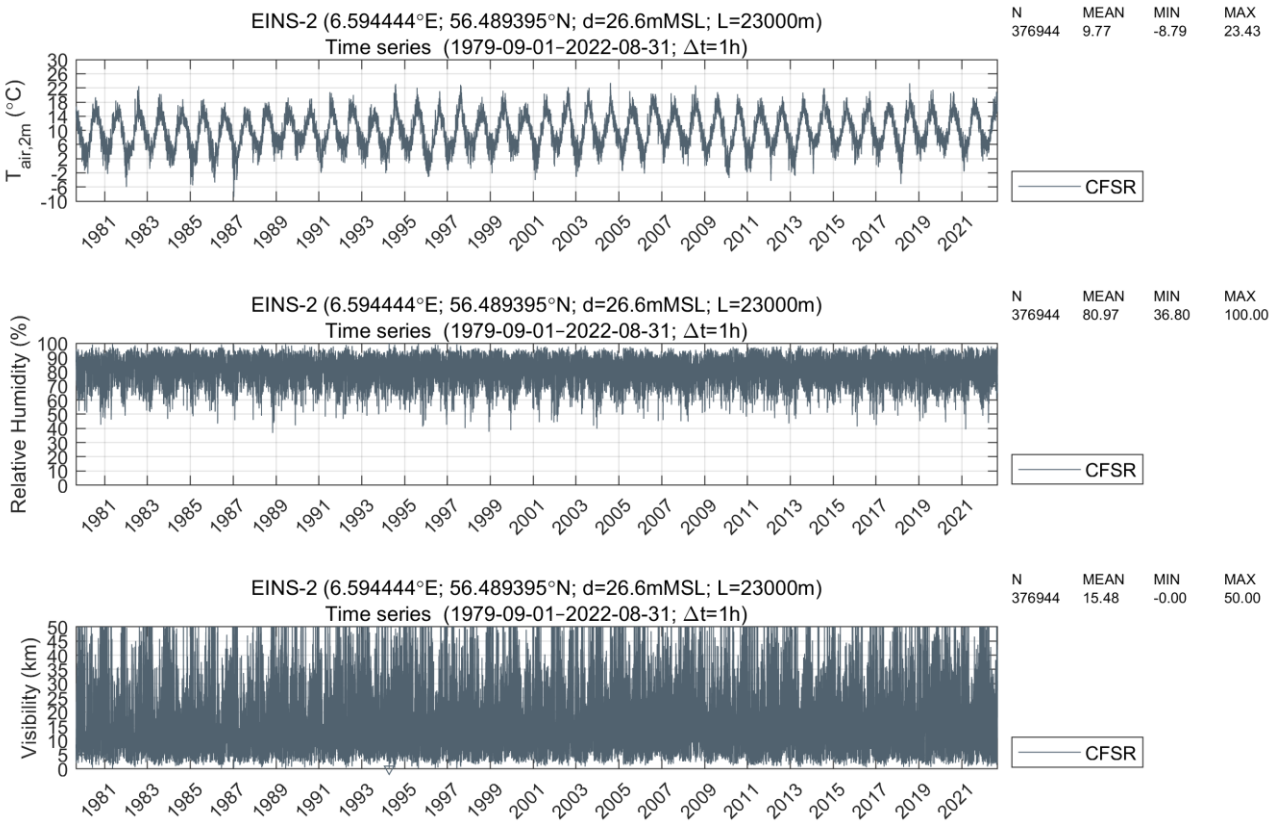

Figure 7.4 Time series of T_{2m}, RH and Visibility at EINS-2

[3] https://en.wikipedia.org/wiki/Dew_point

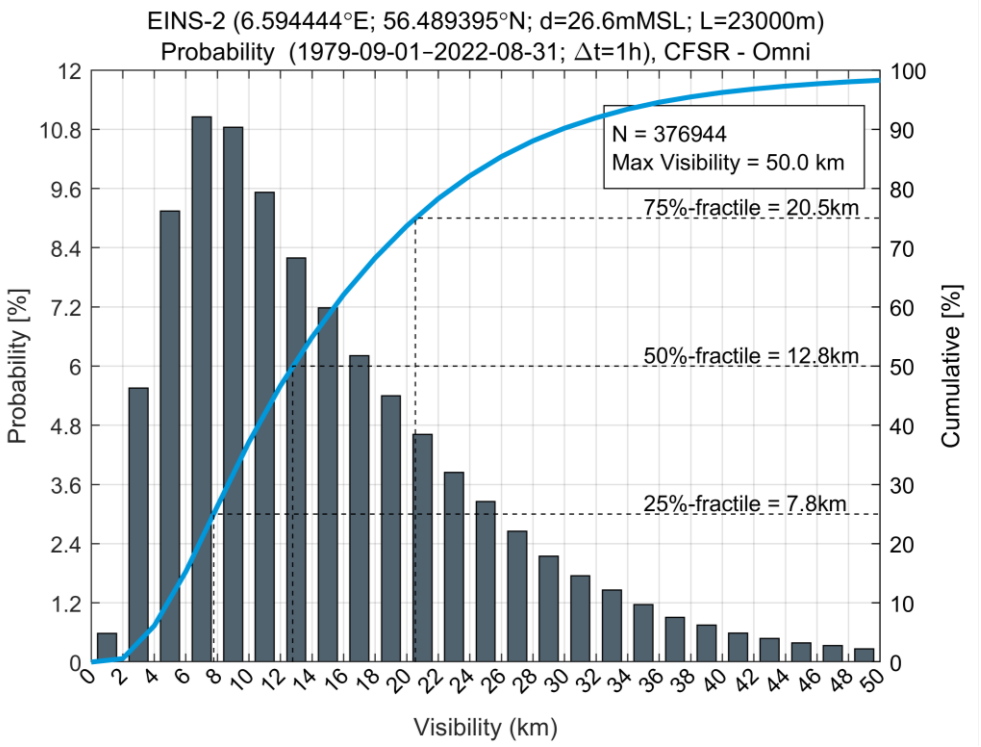

Figure 7.5 Probability of visibility at EINS-2

8 Other Oceanographic Conditions

This section presents analyses of other oceanographic conditions.

Other oceanographic conditions concern water temperature, salinity, and density, and marine growth.

8.1 Water temperature, salinity, and density

Information on the properties of seawater (temperature and salinity) was obtained from the HD_{UKNS3D} model described in Section 5.4 of Part A, [1]. Time series of seawater temperature and seawater salinity were extracted for the surface and near-seabed layer at four (4) locations: EINS-1 (shallowest), EINS-3 (max CS_{tot}), EINS-Island (Mini 2), and EINS-5 (South). The data cover a 10-year period (2013 to 2022) with a temporal resolution of 1-hour. Results of the analysis are presented only at the EINS-South location, where model outputs were validated. Results at the other stations are not produced since the variation in water temperature, salinity, and density across the site is limited.

Seawater temperature

Figure 8.1 presents the monthly statistics (mean, minimum, maximum, and standard deviation) of seawater temperature near the surface and near the seabed temperature at EINS-South. The statistics are summarised in Table 8.1.

The seasonal variation in seawater temperature is clear at the surface with largest temperatures occurring in summer and early autumn (June to September) and the lowest temperatures during the winter and early spring (January to March). The monthly mean seawater temperatures at the surface are higher than those at the seabed for the entire year. The seasonal variation at the seabed is also clear but less pronounced. The highest temperatures occur during autumn and the lowest in spring, showing the delay in temperature changes over the depth.

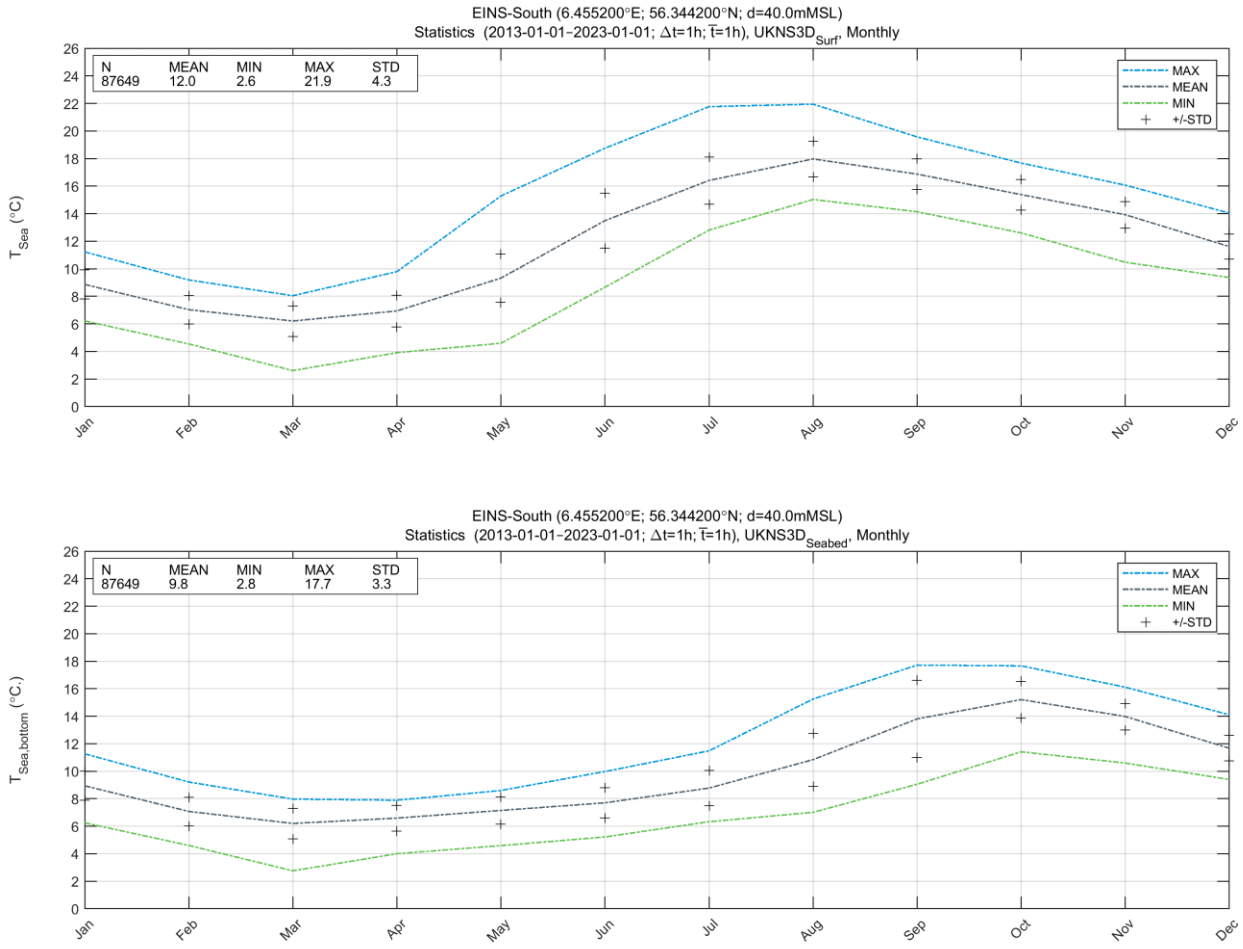

Figure 8.1 Monthly statistics of surface (top panel) and bottom (bottom panel) seawater temperature at EINS-South

Table 8.1 Annual and monthly statistics for seawater temperature near the surface and near the seabed at EINS-South based on HD_{UKNS3D} (2013-01-01 to 2023-01-01)

Near-surface and near-seabed data is extracted from top and bottom layers of HD_{UKNS3D}

Seawater temperature at EINS-South [°C] – Near-surface						
Statistical		№ of data points	Mean	Min.	Max.	STD.
Annual		87,649	12.0	2.6	21.9	4.3
Monthly	Jan.	7,441	8.9	6.2	11.2	1.0
	Feb.	6,768	7.0	4.5	9.2	1.0
	Mar.	7,440	6.2	2.6	8.0	1.1
	Apr.	7,200	6.9	3.9	9.8	1.1
	May	7,440	9.3	4.6	15.3	1.7
	Jun.	7,200	13.5	8.7	18.7	2.0
	Jul.	7,440	16.4	12.8	21.8	1.7
	Aug.	7,440	18.0	15.0	21.9	1.3
	Sep.	7,200	16.9	14.1	19.6	1.1
	Oct.	7,440	15.4	12.6	17.7	1.1
	Nov.	7,200	13.9	10.5	16.1	1.0
	Dec.	7,440	11.6	9.4	14.0	0.9
Seawater temperature at EINS-South [°C] - Near-seabed						
Statistical		№ of data points	Mean	Min.	Max.	STD.
Annual		87,649	10.3	2.7	17.7	3.4
Monthly	Jan.	7,441	8.9	6.2	11.3	1.0
	Feb.	6,768	7.1	4.6	9.2	1.0
	Mar.	7,440	6.2	2.7	8.0	1.1
	Apr.	7,200	6.6	4.0	7.9	0.9
	May	7,440	7.4	4.6	9.4	1.0
	Jun.	7,200	8.4	6.0	10.8	1.1
	Jul.	7,440	10.2	6.5	13.1	1.5
	Aug.	7,440	12.6	7.6	16.1	1.9
	Sep.	7,200	15.0	11.0	17.7	1.9
	Oct.	7,440	15.3	11.7	17.7	1.2
	Nov.	7,200	14.0	10.6	16.1	1.0
	Dec.	7,440	11.7	9.4	14.1	0.9

Seawater salinity

Figure 8.2 presents the monthly statistics (mean, minimum, maximum, and standard deviation) of seawater salinity near the surface and near the seabed salinity at EINS-South. The statistics are summarised in Table 8.2.

The seasonal variation in seawater salinity is clear at the surface. The highest and mean salinity values are almost constant during the whole year, while the lowest salinity values vary considerably during the spring and summer months. During the first month of spring, minimum salinity values at the surface drop to a minimum in May, where then minimum salinity values increase slowly until November. There is little seasonal variation near the seabed.

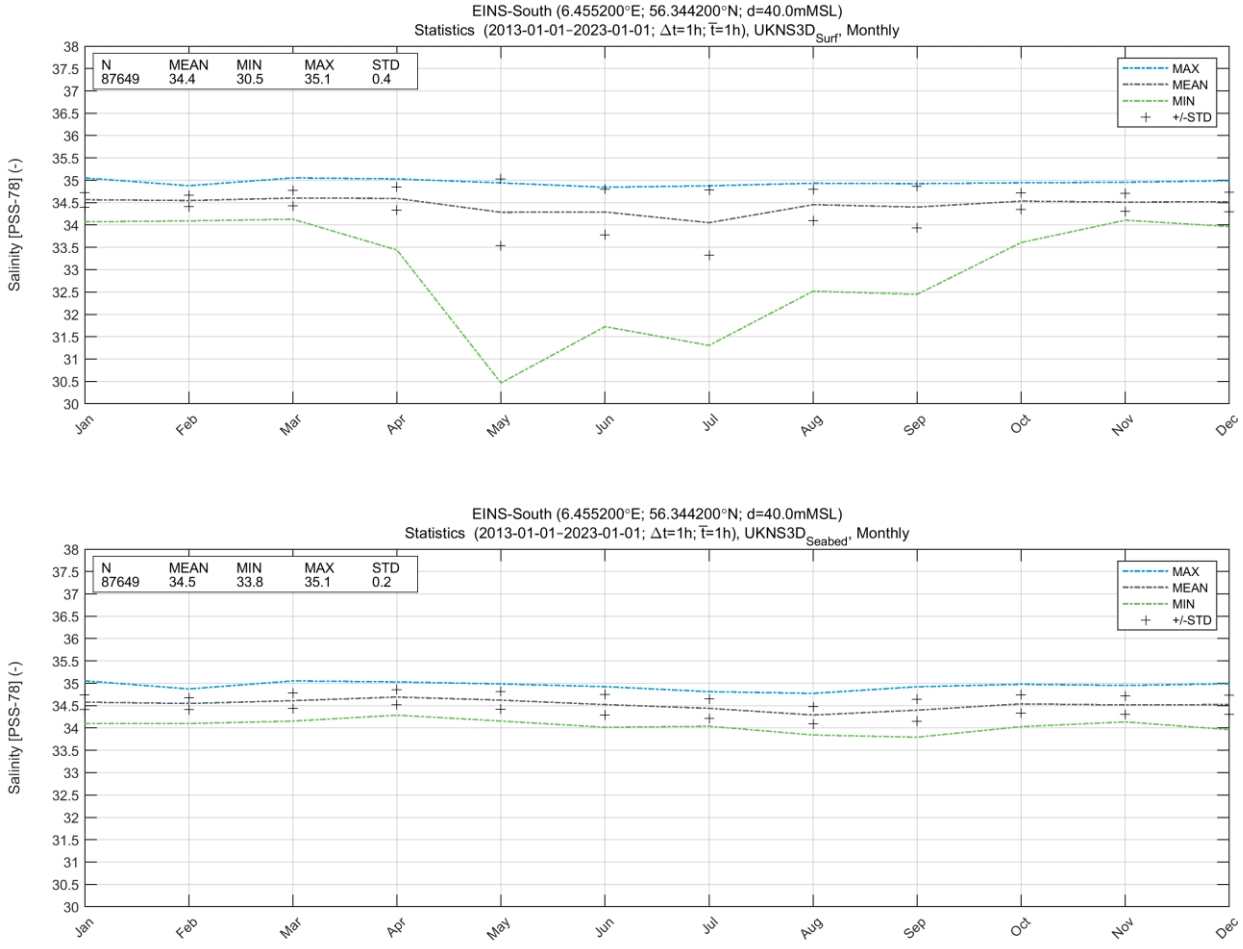

Figure 8.2 Monthly statistics of surface (top panel) and bottom (bottom panel) seawater salinity at EINS-South

Table 8.2 Annual and monthly statistics for seawater salinity near the surface and near the seabed at EINS-South based on HD_{UKNS3D} (2013-01-01 to 2023-01-01)

Near-surface and near-seabed data is extracted from top and bottom layers of HD_{UKNS3D}

Seawater salinity at EINS-South [PSS-78] - Near-surface						
Statistical		№ of data points	Mean	Min.	Max.	STD.
Annual		87,649	34.4	30.5	35.1	0.4
Monthly	Jan.	7,441	34.6	34.1	35.1	0.2
	Feb.	6,768	34.5	34.1	34.9	0.1
	Mar.	7,440	34.6	34.1	35.1	0.2
	Apr.	7,200	34.6	33.4	35.0	0.3
	May	7,440	34.3	30.5	34.9	0.8
	Jun.	7,200	34.3	31.7	34.8	0.5
	Jul.	7,440	34.1	31.3	34.9	0.7
	Aug.	7,440	34.5	32.5	34.9	0.3
	Sep.	7,200	34.4	32.4	34.9	0.5
	Oct.	7,440	34.5	33.6	34.9	0.2
	Nov.	7,200	34.5	34.1	35.0	0.2
	Dec.	7,440	34.5	34.0	35.0	0.2
Seawater salinity at EINS-South [PSS-78] - Near-seabed						
Statistical		№ of data points	Mean	Min.	Max.	STD.
Annual		87,649	34.5	33.8	35.1	0.2
Monthly	Jan.	7,441	34.6	34.1	35.1	0.2
	Feb.	6,768	34.5	34.1	34.9	0.1
	Mar.	7,440	34.6	34.2	35.1	0.2
	Apr.	7,200	34.7	34.3	35.0	0.2
	May	7,440	34.6	34.2	35.0	0.2
	Jun.	7,200	34.5	34.0	34.9	0.2
	Jul.	7,440	34.4	34.0	34.8	0.2
	Aug.	7,440	34.3	33.8	34.8	0.2
	Sep.	7,200	34.4	33.8	34.9	0.2
	Oct.	7,440	34.5	34.0	35.0	0.2
	Nov.	7,200	34.5	34.1	35.0	0.2
	Dec.	7,440	34.5	34.0	35.0	0.2

Seawater density

The density of seawater was calculated from the seawater temperature and salinity from the HD_{UKNS3D} model using the international one-atmosphere equation of the state of seawater derived by Millero, F.J. & Poisson, A. [23]. [23].

Figure 8.3 presents the monthly statistics (mean, minimum, maximum, and standard deviation) of near sea surface and near-seabed water density at the EINS-South location. The statistics are summarised in Table 8.3.

The seasonal variation in seawater density is clear at the surface with the largest density occurring in winter (December to March) and the lowest density seen during spring and summer (April to September). There is little seasonal variation in seawater density at the seafloor, but the lowest density levels occur during September to November, showing the delay in density changes over the depth, i.e., the variations follow roughly the combined pattern of temperature and salinity.

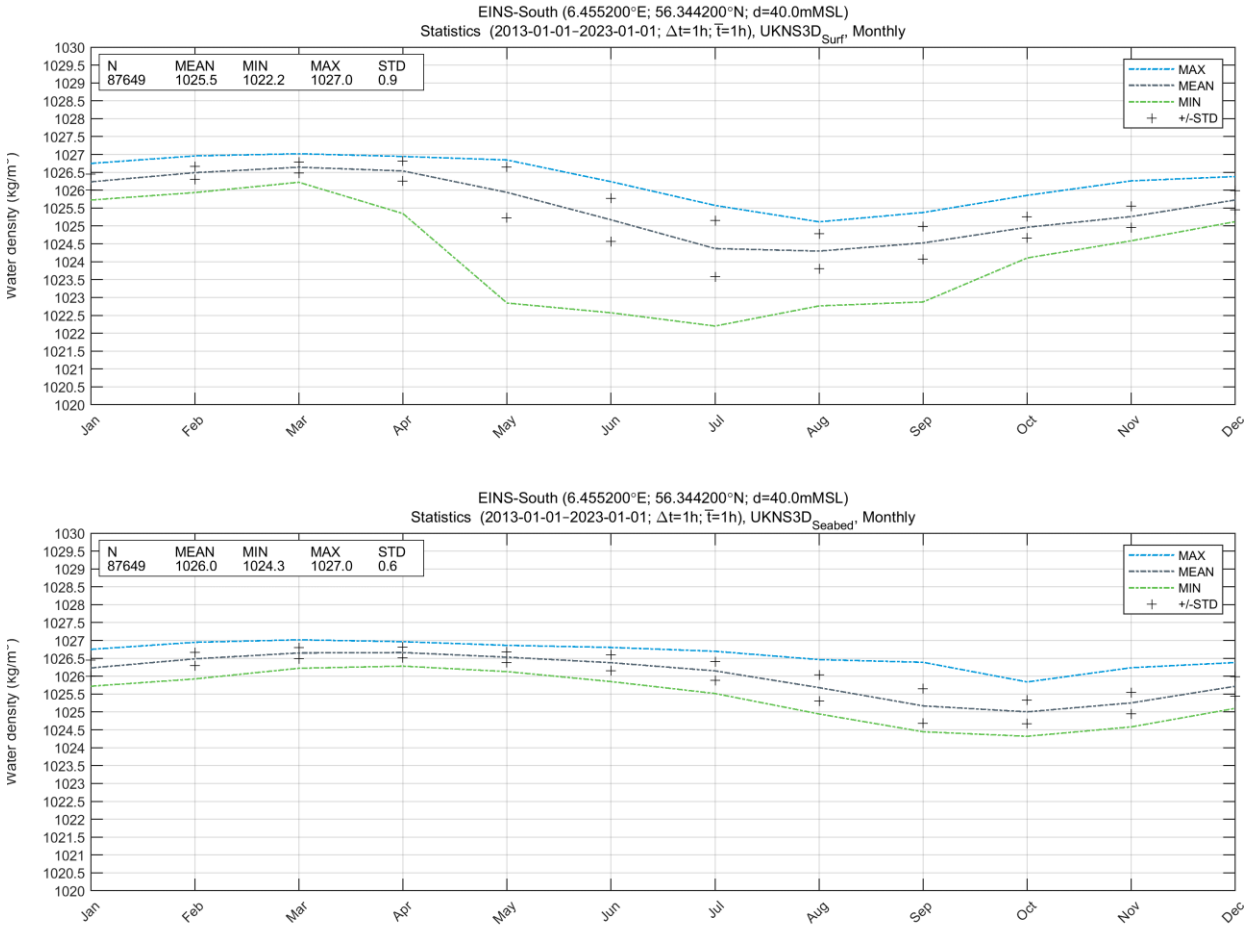

Figure 8.3 Monthly statistics of surface (top panel) and bottom (bottom panel) seawater density at EINS-South

Table 8.3 Annual and monthly statistics for seawater density at EINS-South based on HD_{UKNS3D} (2013-01-01 to 2023-01-01)
Near-surface and near-seabed data is extracted from top and bottom layers of HD_{UKNS3D}.

Seawater density at EINS-South [kg/m³] - Near-surface						
Statistical		№ of data points	Mean	Min.	Max.	STD.
Annual		87,649	1025.5	1022.2	1027.0	0.9
Monthly	Jan.	7,441	1026.2	1025.7	1026.7	0.2
	Feb.	6,768	1026.5	1025.9	1027.0	0.2
	Mar.	7,440	1026.6	1026.2	1027.0	0.2
	Apr.	7,200	1026.5	1025.3	1026.9	0.3
	May	7,440	1025.9	1022.8	1026.8	0.7
	Jun.	7,200	1025.2	1022.6	1026.2	0.6
	Jul.	7,440	1024.4	1022.2	1025.6	0.8
	Aug.	7,440	1024.3	1022.8	1025.1	0.5
	Sep.	7,200	1024.5	1022.9	1025.4	0.5
	Oct.	7,440	1025.0	1024.1	1025.9	0.3
	Nov.	7,200	1025.3	1024.6	1026.3	0.3
	Dec.	7,440	1025.7	1025.1	1026.4	0.3
Seawater density at EINS-South [kg/m³] - Near-seabed						
Statistical		№ of data points	Mean	Min.	Max.	STD.
Annual		87,649	1026.0	1024.3	1027.0	0.6
Monthly	Jan.	7,441	1026.2	1025.7	1026.8	0.2
	Feb.	6,768	1026.5	1025.9	1026.9	0.2
	Mar.	7,440	1026.7	1026.2	1027.0	0.2
	Apr.	7,200	1026.7	1026.3	1027.0	0.1
	May	7,440	1026.5	1026.1	1026.9	0.2
	Jun.	7,200	1026.4	1025.8	1026.8	0.2
	Jul.	7,440	1026.1	1025.5	1026.7	0.3
	Aug.	7,440	1025.7	1024.9	1026.5	0.4
	Sep.	7,200	1025.2	1024.4	1026.4	0.5
	Oct.	7,440	1025.0	1024.3	1025.8	0.3
	Nov.	7,200	1025.3	1024.6	1026.2	0.3
	Dec.	7,440	1025.7	1025.1	1026.4	0.3

9 Marine growth

Marine growth is defined as the unwanted settlement and growth of marine organisms on submerged surfaces of ship hulls, buoys, piers, offshore platforms, etc. It may also be referred to as “marine fouling” or “biofouling”. The composition and extent of marine growth vary with the biogeographical region being higher at tropical regions than at other latitudes.

The assessment of marine growth is based on scientific publications (see [24], [25], [26], [27]). From those publications there are not available marine growth time series, only values of observed marine growth weight at different water depths.

Numerous factors influence the amount and type of marine growth, including salinity, temperature, depth, current speed, and wave exposure, in addition to biological factors such as food availability, larval supply, presence of predators, and the general biology and physiology of the fouling species. Extensive knowledge on factors that affect the level of marine growth in the North Sea has been obtained through years of operation and maintenance of gas and oil platforms. Once a new hard substrate has been introduced into the environment, the organisms colonise quickly, and can grow within days. Typically, a succession in species composition will take place as the age of the deployed substrate increases. The succession is a result of organisms competing for space, and a quasi-steady state in fouling communities will be established within less than 4 to 6 years. Along with succession, individual organisms grow larger which creates an increasing thickness of marine growth. Predators such as starfish become an integral part of the fouling ecosystem finding empty spaces in the marine growth cover. In the southern North Sea (< 56° N), some studies have shown that marine growth on offshore installations (6900 records from 39 locations duing 1996-2017) may vary between 0 and 350 mm with an average of 52.76 mm (± 36.54 mm standard deviation) [24]. Of those installations located in regions with high concentrations of chlorophyll (0.84 mg/m^3) showed thicker layers of marine growth. DNV [28] states that values, up to 150 mm between sea level and LAT –10 m, may be seen in the Southern North Sea.

Studies carried out in two existing offshore wind farms, Egmond aan Zee (52.6° N, 4.41° E) and Princess Amalia (52.58° N, 4.02° E), located at a depth range of 17 – 22 m within the Dutch EEZ have demonstrated that marine growth below the splash zone (±1 m) is dominated by mussels, starfish (predating on mussels), various crustaceans (sessile and mobile), sea anemones and polychaetes (tube-building and mobile) [25], [26], [27]. Thickness of marine growth was measured/estimated on two monopiles in the Egmond aan Zee wind farm 1.7 years after monopile erection and probably too early to reflect a mature fouling community. Below the splash zone, marine growth ranged between 5 and 15 cm in the upper 6-7 m of a monopile. Below 6-7 m, the thickness of marine growth decreased to between 1 and 5 cm but with 100% cover. The marine growth will add to the weight of substructures (monopiles) ranging between 1 and 6.5 kg/m^2 depending on depth. Weight data from the two existing wind farms (Egmond aan Zee and Princess Amalia) differs with respect to depth-distribution as Egmond aan Zee showed increasing weight under water from 2 kg/m^2 at 2 m to 6.5 kg/m^2 at 10 m and decreasing to 1.5 kg/m^2 at 15 m. In contrast, marine growth in Princess Amalia wind farm, monitored after 4 and 6 years of installation, peaked at 2 m with weight under water at 4.3 kg/m^2 gradually decreasing to 1 kg/m^2 at 10 m, to increase again to

1.5 kg/m^2 at 17 m. Slightly smaller values are expected at higher latitudes of the North Sea.

In [29], density data were acquired from A12-CCP and the Q1 Haven platforms operated by Petrogas E&P Netherlands B.V. to model density across 39 platforms located in the southern North Sea. Weight varied from 2 to 113 kg/m^2 (average 47 kg/m^2), thickness from 5 to 120 mm (average 35 mm) with densities between 311 and 945 kg/m^3. The model predicted a reduction in weight with depth and a generalised density of 612 kg/m^3.

At Central and Northern North Sea (56°N to 59°N), DNV [28] suggest applying a thickness of marine growth of 10 cm (from sea surface to 40 m depth) to account for the added weight on the structural component. The density of the marine growth may be set equal to 1325 kg/m^3 (resulting in thickness of 1-5 mm considering a weight of 1-6.5 kg/m^2) unless more accurate data are available. We suggest following DNVs recommendation, which also will be in line with the observed/calculated depth distribution of ash free and wet weight of biomass.

10 References

[1] DHI, "Energy Island North Sea, Metocean Site Conditions Assessment, Part A: Data Basis – Measurements and Models, 2023-06-09 ", 2023.

[2] NORSOK, "Actions and action effects, N-003, Edition 3, April 2016," 2016.

[3] Energinet, "Scope of Services – North Sea Energy Island Metocean Conditions Assessment, document number: 2/05192-6, 2022-06-22," 2022.

[4] Energinet, "Scope of Services – Site Metocean Conditions Assessment for Offshore Wind Farms, North Sea, Document number: 22/08564-1, 2022-11-08," 2022.

[5] *Environmental Conditions and Environmental Loads*, DNV-RP-C205, DNV, 2021.

[6] *Wind energy generation systems – Part 3-1: Design Requirements for fixed offshore wind turbines. Ed. 1.0*, IEC-61400-3-1, 2019.

[7] DHI, "Energy Island North Sea, Metocean Site Conditions Assessment, Part B: Data Analyses – Energy Island, 2023-06-16," 2023.

[8] DHI, "Energy Island, North Sea, Metocean Site Conditions Assessment, Part C: Data Analyses – Wind Farm Area (FEED), due Apr. 2023," 2023.

[9] DHI, "Energy Island North Sea, Metocean Site Conditions Assessment, Part D: Data Basis – Hindcast revalidation note, due Jan. 2024," 2024.

[10] D. L. Codiga, "Unified Tidal Analysis and Prediction Using the UTide Matlab Functions. Technical Report 2011-01," Graduate School of Oceanography, University of Rhode Island, Narragansett, RI. 59pp, 2011.

[11] B. B. a. S. L. R. Pawlowicz, "Classical tidal harmonic analysis including error estimates in MATLAB using T-TIDE, Computers & Geosciences 28, pp. 929-937," 2002.

[12] K. E. L. a. D. A. Jay, "Enhancing tidal harmonic analysis: Robust (hybrid L-1/L-2) solutions, Cont. Shelf Res. 29, pp. 78-88. DOI: 10.1016/j.csr.2008.1004.1011," 2009.

[13] J. Y. C. a. V. A. B. M. G. G. Foreman, "Versatile Harmonic Tidal Analysis: Improvements and

Applications," *J. Atmos. Oceanic Tech. 26, pp. 806-817. DOI: 810.1175/2008JTECHO1615.1171,* 2009.

[14] DHI, "MIKE 21 Spectral Waves FM: User Guide," 2022.

[15] DHI, "Energy Island North Sea, Metocean Site Conditions Assessment, Part A: Data Basis – Measurements & Models, 2023-06-09 ", 2023.

[16] *Petroleum and natural gas industries — Specific requirements for offshore structures — Part 1: Metocean design and operating considerations*, ISO 19901-1:2015, ISO, 2015.

[17] J. D. Fenton, "The numerical solution of steady water wave problems," *Computers & Geosciences,* vol. vol. 14, pp. pp. 357-368, 1988.

[18] J. D. Fenton, "Nonlinear Wave Theories," *Ocean Engineering Science,* vol. Vol.9, 1990.

[19] B. T. S. Paulsen, Ben de; van der Meulen, Michiel; Jacobsen, Niels Gjøl, "Probability of wave slamming and the magnitude of slamming loads on offshore wind turbine foundations," *Coastal Engineering,* pp. 76-95, 2019.

[20] D. J. Cecil. *LIS/OTD Gridded Lightning Climatology Data Collection, Version 2.3.2015*, NASA EOSDIS Global Hydrology Resource Center Distributed Active Archive Center, Huntsville, Alabama, U.S.A., doi: http://dx.doi.org/10.5067/LIS/LIS-OTD/DATA311.

[21] D. J. B. Cecil, D. E.; Blackeslee, R. J., "Gridded lightning climatology from TRMM-LIS and OTD: Dataset description," *Atmospheric Research,* vol. 135-136, pp. 404-414, 2014.

[22] P. R. J. Doran, D. J. Beberwyk, G. R. Brooks, G. A. Gayno, R. T. Williams, J. M. Lewis and R. J. Lefevre, "The MM5 at the AF Weather Agency – new products to support military operations," in *8th Conference on Aviation, Range, and Aerospace Meteorology, American, Dallax, TX, USA.*, 1999.

[23] F. J. Millero and A. Poisson, "International one-atmosphere equation of state of seawater," *Deep Sea Research Part A. Oceanographic Research Papers,* vol. 28, no. 6, pp. 625-629, 1981/06/01/ 1981, doi: https://doi.org/10.1016/0198-0149(81)90122-9.

[24] L. P. Almeida and J. W. P. Coolen, "Modelling thickness variations of macrofouling communities on offshore

platforms in the Dutch North Sea," *Journal of Sea Research,* vol. 156, p. 101836, 2020/01/01/ 2020, doi: https://doi.org/10.1016/j.seares.2019.101836.

[25] M. C. Bruija, "Biological Fouling - Survey of marine fouling on turbine support structures of the Offshore Windfarm Egmond aan Zee.," *KEMA Nederland B.V.,* 2010.

[26] S. B. a. W. Lengkeek, "Benthic communities on hard substrates of the offshore wind farm Egmond aan Zee (OWEZ) - Including results of samples collected in scour holes," *Bureau Waardenburg bv,* 2012.

[27] L. V. d. M. a. M. F. T. Vanagt, "Development of hard substrate fauna in the Princess Amalia Wind Farm. Monitoring 3.5 years after construction.," *eCOAST,* 2013.

[28] *Loads and site conditions for wind turbines*, DNV-ST-0437, DNV, 2021.

[29] J. W. P. A. Coolen, L. P.; Olie, R., "Modelling marine growth biomass on North Sea offshore structures," presented at the Structures in the Marine Environment (SIME2019), Glasgow, UK, 2019.

[30] J. E. Heffernan and J. A. Tawn, "A conditional approach for multivariate extreme values," *Journal of the Royal Statistical Society. Series B,* vol. 66, no. 3, pp. 497-546, 2004.

11 Appendix A: List of Data Reports

This appendix presents a list of data reports attached to this report.

Table 11.1 List of data reports (.xlsx) attached to this report
Normal and extreme conditions (based on T-EVA).

Filename
Normal and extreme conditions (based on T-EVA)
OWF-1_Metocean-Data-Report_2023-06-30.xlsx
OWF-2_Metocean-Data-Report_2023-06-30.xlsx
OWF-3_Metocean-Data-Report_2023-06-30.xlsx
OWF-4_Metocean-Data-Report_2023-06-30.xlsx
OWF-5_Metocean-Data-Report_2023-06-30.xlsx
OWF-6_Metocean-Data-Report_2023-06-30.xlsx
OWF-7_Metocean-Data-Report_2023-06-30.xlsx
OWF-8_Metocean-Data-Report_2023-06-30.xlsx

12 Appendix B: Sensitivity of T-EVA to Distribution, Threshold, and Fitting

This section presents an assessment of the sensitivity of T-EVA to distribution, threshold, and fitting, leading to the choice of EVA settings.

It is good practice for conducting EVA to assess the sensitivity of the results using multiple thresholds, distributions, and fitting methods. Furthermore, one should consider the goodness of fit (visually), and magnitude (inter-compared), and water depth (waves), before deciding on an adequate EVA setup.

Figure 12.1 – Figure 12.7 presents sensitivity of T-EVA to distribution, threshold, and fitting for waves (H_{m0}), water levels (high and low, total and residual), and current speed (total and residual) at EINS-2 (H_{m0} and WL) and EINS-1 (CS) (the location coordinates are given in Table 7.1) .

The plots depict the 100-year value vs. number of events per year for various long-term extreme value distributions and for two common fitting methods (Maximum likelihood (ML) and Least-Squares (LS), see technical details in Appendix C: T-EVA – Traditional EVA. Based on the approach above, the applied EVA settings are chosen as follows:

- **Waves**: 2-p Weibull distribution fitted by least-square (LS) to the 129 (3x43) peak events separated by at least 36 hours.
- **Water level**: Exponential distribution fitted by least-square (LS) to the 215 (5x43) peak events separated by at least 36 hours.
- **Current speed**: 2-p Weibull distribution fitted by least-square (LS) to the 129 (3x43) peak events separated by at least 36 hours.

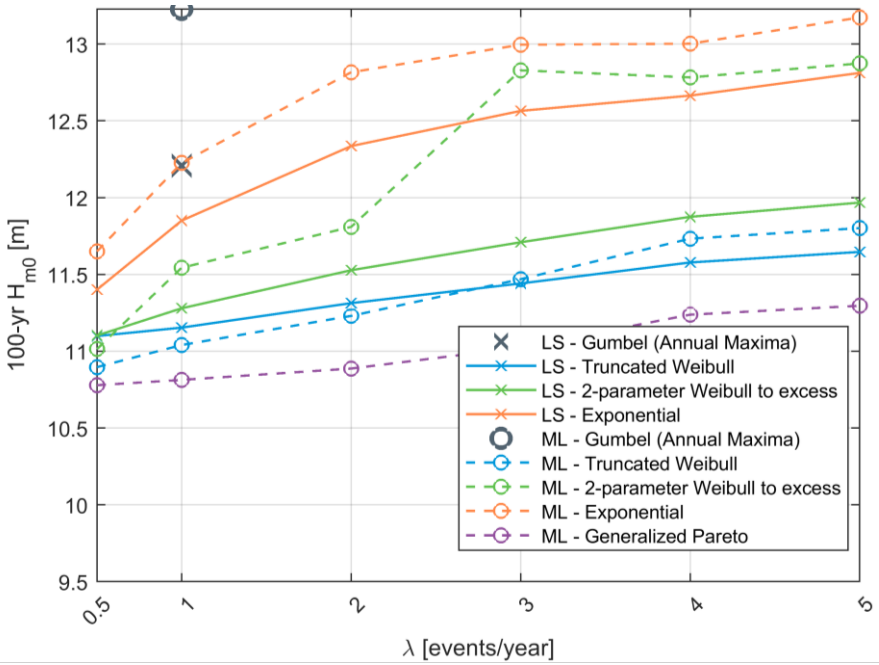

Figure 12.1 Sensitivity of T-EVA to distribution, threshold, and fitting at EINS-2
Variable: H_{m0}

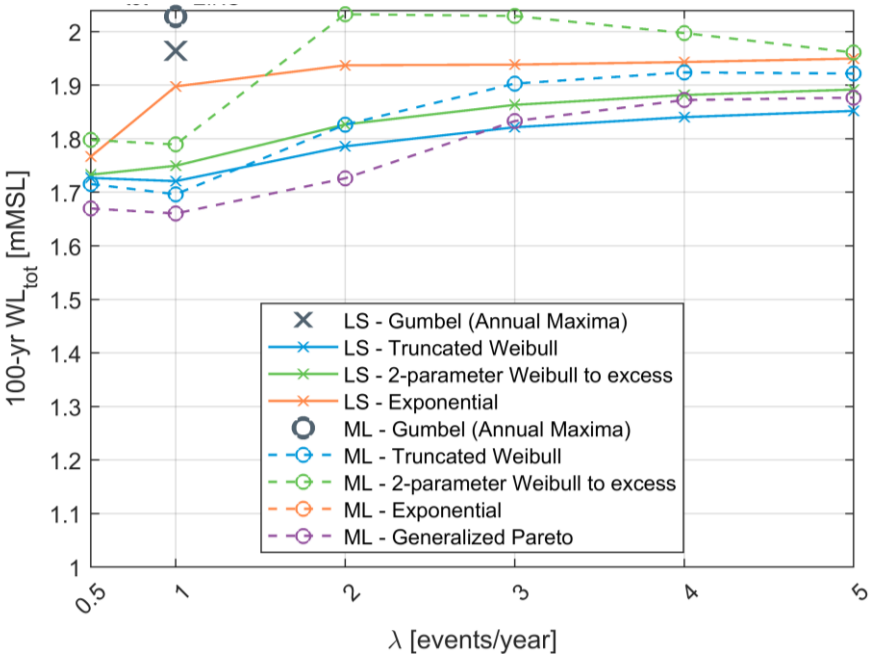

Figure 12.2 Sensitivity of T-EVA to distribution, threshold, and fitting at EINS-2
Variable: WL_{tot}

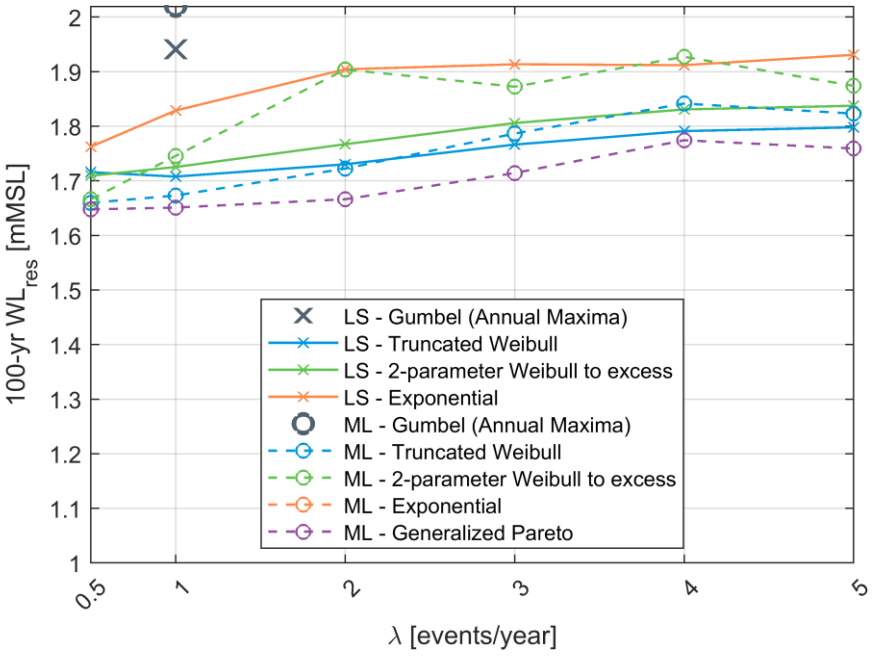

Figure 12.3 Sensitivity of T-EVA to distribution, threshold, and fitting at EINS-2
Variable: WL_{res}

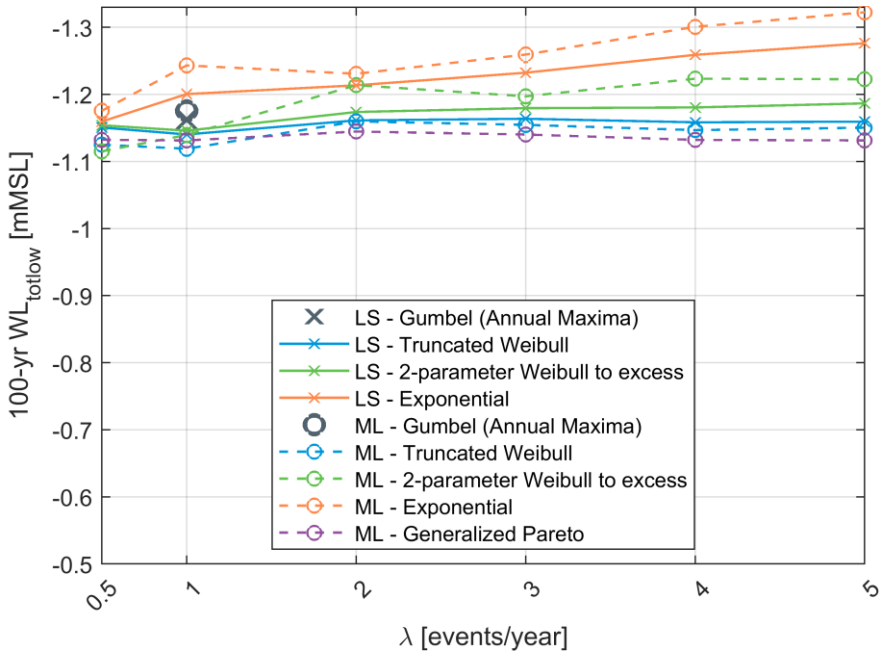

Figure 12.4 Sensitivity of T-EVA to distribution, threshold, and fitting
Variable: $WL_{tot,low}$

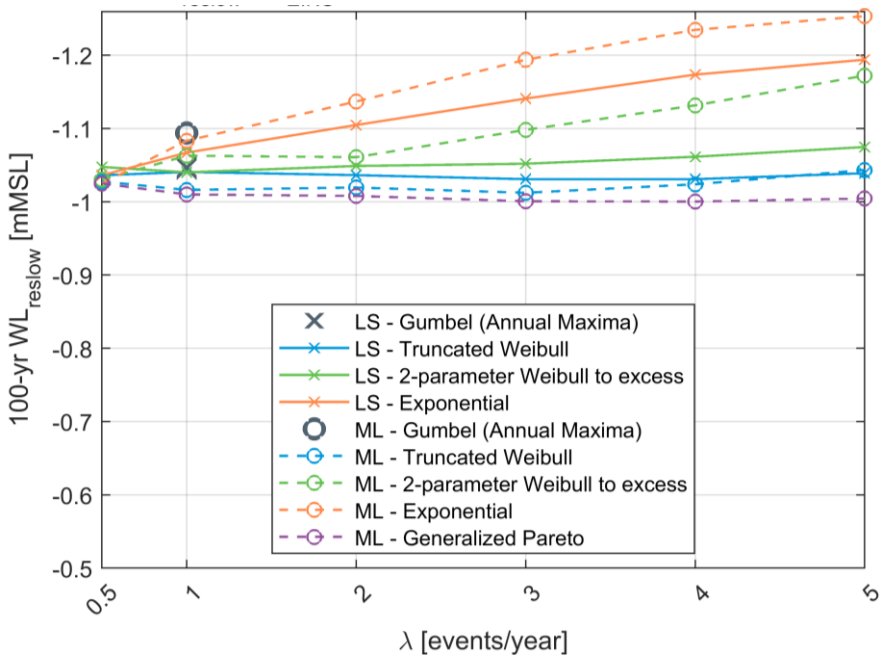

Figure 12.5 Sensitivity of T-EVA to distribution, threshold, and fitting
Variable: $WL_{res,low}$

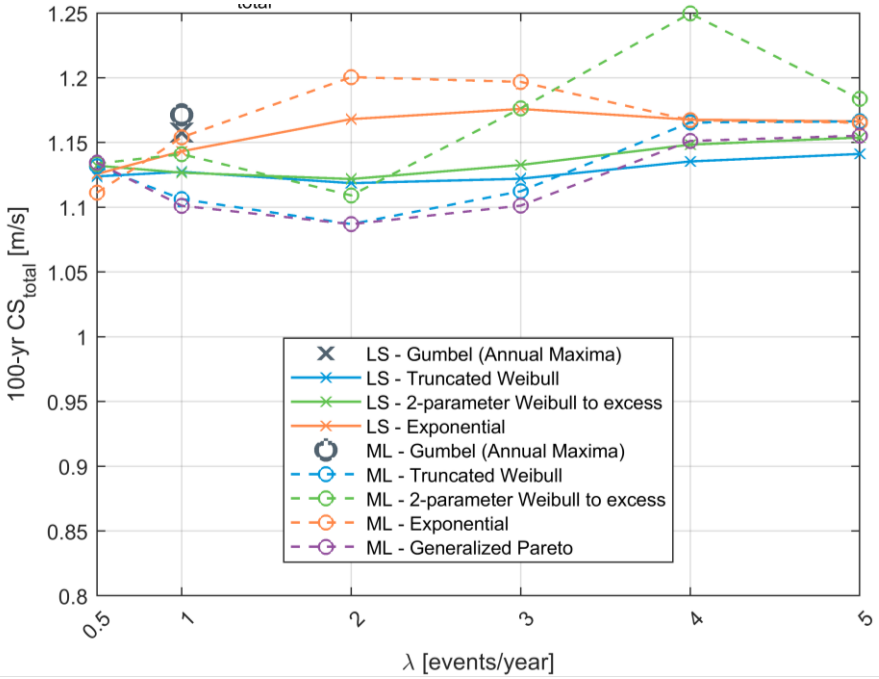

Figure 12.6 Sensitivity of T-EVA to distribution, threshold, and fitting at EINS-1
Variable: CS_{tot}

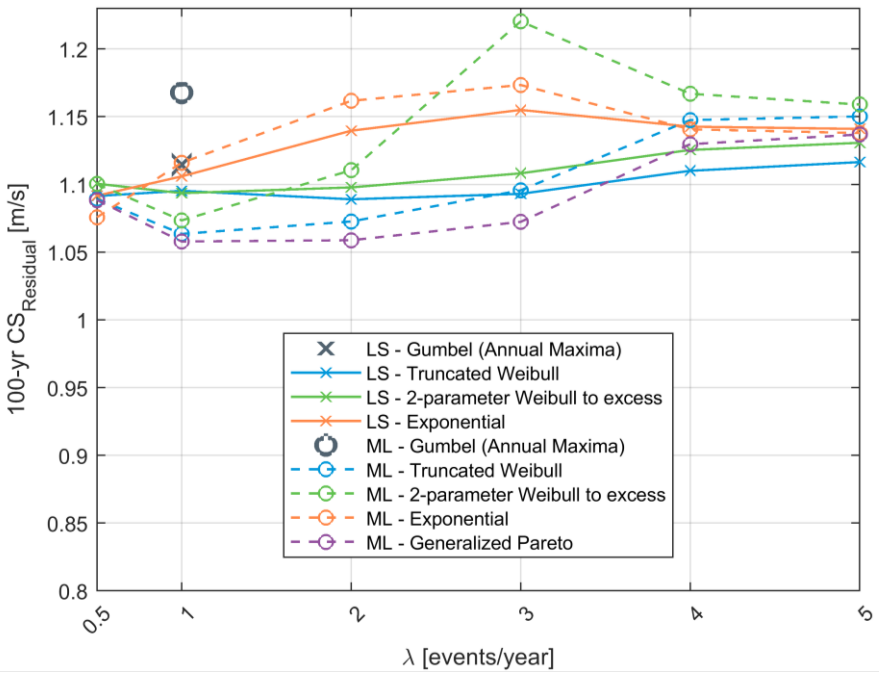

Figure 12.7 Sensitivity of T-EVA to distribution, threshold, and fitting at EINS-1
Variable: CS_{res}

13 Appendix C: T-EVA – Traditional EVA

This document describes the DHI extreme value analysis (EVA).

13.1 Summary of approach

Extreme values with conditioned long return periods are estimated by fitting a probability distribution to historical data. Several distributions, data selection and fitting techniques are available for estimation of extremes, and the estimated extremes are often rather sensitive to the choice of method. However, it is not possible to choose a preferred method only on its superior theoretical support or widespread acceptance within the industry. Hence, it is common practice to test several approaches and make the final decision based on goodness of fit.

The typical extreme value analyses involved the following steps:

1. Extraction of independent identically-distributed events by requiring that events are separated by at least 36 hours (or similar), and that the value between events had dropped to below 70% (or similar) of the minor of two consecutive events. The extraction is conducted individually for omni and directional/seasonal subsets respectively.
2. Fitting of extreme value distribution to the extracted events, individually for omni and directional/seasonal subsets. Distribution parameters are estimated either by maximum likelihood or least-square methods. The following analysis approaches are used (see Section 13.2 for details):
   - Fitting the Gumbel distribution to annual maxima.
   - Fitting a distribution to all events above a certain threshold (the Peak-Over-Threshold method). The distribution type can be exponential, truncated Weibull or 2-parameter Weibull to excess.
3. Constraining of subseries to ensure consistency with the omni/all-year distribution; see Section 13.4 for details.
4. Bootstrapping to estimate the uncertainty due to sampling error; see Section 13.6 for details.
5. Values of other parameters conditioned on extremes of one variable are estimated using the methodology proposed in [30] (Heffernan & Tawn).

Figure 13.1 shows an example of EVA based on 38 years of hindcast data and a Gumbel distribution fitted to the annual maxima using max. likelihood.

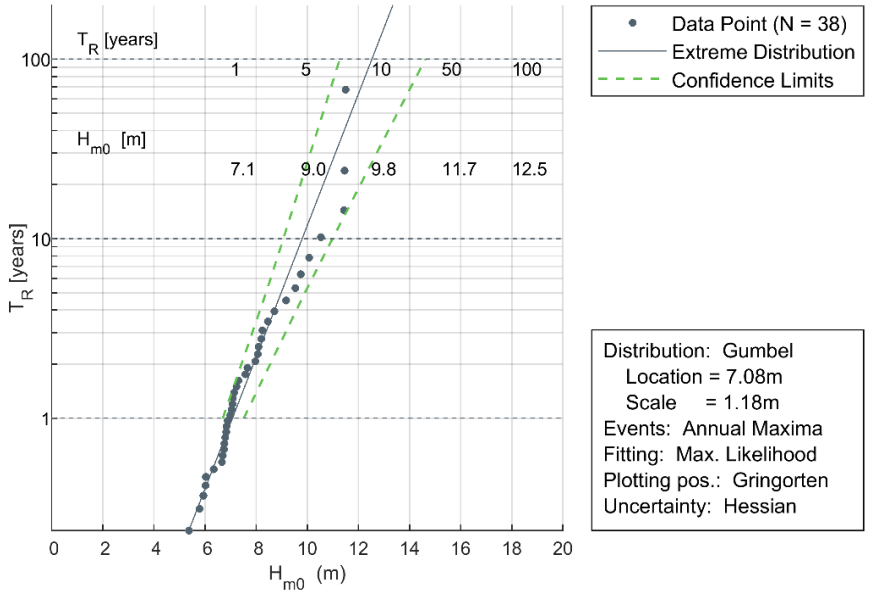

Figure 13.1 Example of traditional extreme value analysis of H_{m0}.
A Gumbel distribution fitted to the annual maxima using maximum likelihood.

13.2 Long-term distributions

The following probability distributions are often used in connection with extreme value estimation:

- 2-parameter Weibull distribution
- Truncated Weibull distribution
- Exponential distribution
- Gumbel distribution

The 2-parameter Weibull distribution is given by:

$$P(X < x) = 1 - \exp\left(-\left(\frac{x}{\beta}\right)^{\alpha}\right) \tag{13.1}$$

with distribution parameters α (shape) and β (scale). The 2-parameter Weibull distribution used in connection with Peak-Over-Threshold (POT) analysis is fitted to the excess of data above the threshold, i.e., the threshold value is subtracted from data prior to fitting.

The 2-parameter *truncated* Weibull distribution is given by:

$$P(X < x) = 1 - \frac{1}{P_0}\exp\left(-\left(\frac{x}{\beta}\right)^{\alpha}\right) \tag{13.2}$$

with distribution parameters α (shape) and β (scale) and the exceedance probability, P_0, at the threshold level, γ, given by:

$$P_0 = \exp\left(-\left(\frac{\gamma}{\beta}\right)^{\alpha}\right) \tag{13.3}$$

The 2-parameter truncated Weibull distribution is used in connection with Peak-Over-Threshold analysis, and as opposed to the non-truncated 2-p Weibull, it is fitted directly to data, i.e., the threshold value is **not** subtracted from data prior to fitting.

The exponential distribution is given by:

$$P(X < x) = 1 - \exp\left(-\left(\frac{x-\mu}{\beta}\right)\right), \quad x \geq \mu \tag{13.4}$$

with distribution parameters β (scale) and μ (location). Finally, the Gumbel distribution is given by:

$$P(X < x) = \exp\left(-\exp\left(\frac{\mu - x}{\beta}\right)\right) \tag{13.5}$$

with distribution parameters β (scale) and μ (location).

13.3 Individual wave and crest height

Short-term distributions

The short-term distributions of individual wave heights and crests conditional on H_{m0} are assumed to follow the distributions proposed by Forristall, (Forristall G. Z., 1978) and (Forristall G. Z., 2000). The Forristall wave height distribution is based on Gulf of Mexico measurements, but experience from the North Sea has shown that these distributions may have a more general applicability. The Forristall wave and crest height distributions are given by:

$$P(X > x \mid H_{m0}) = \exp\left(-\left(\frac{x}{\alpha H_{m0}}\right)^{\beta}\right) \tag{13.6}$$

where the distribution parameters, α and β, are as follows:

Forristall wave height: α = 0.681 β = 2.126

Forristall crest height (3D): $\alpha = 0.3536 + 0.2568 \cdot S_1 + 0.0800 \cdot Ur$

$\beta = 2 - 1.7912 \cdot S_1 - 0.5302 \cdot Ur + 0.284 \cdot Ur^2$

$$S_1 = \frac{2\pi}{g}\frac{H_{m0}}{T_{01}^2} \quad \text{and} \quad U_r = \frac{H \cdot L^2}{d^3}$$

For this type of distribution, the distribution of the extremes of a given number of events, N, (waves or crests) converges towards the Gumbel distribution conditional on the most probable value of the extreme event, H_{mp} (or C_{mp} for crests):

$$P(h_{\max} \mid H_{mp}) = \exp\left(-\exp\left(-\ln N\left(\left(\frac{h_{\max}}{H_{mp}}\right)^{\beta} - 1\right)\right)\right) \tag{13.7}$$

13.3.1 Individual waves (modes)

The extreme individual wave and crest heights are derived using the storm mode approach, (Tromans, P.S. and Vanderschuren, L., 1995). The storm modes, or most probable values of the maximum wave or crest in the storm (H_{mp} or C_{mp}), are obtained by integrating the short-term distribution of wave heights conditional on H_{m0} over the entire number of sea states making up the storm. In practice, this is done by following these steps:

1. Storms are identified by peak extraction from the time series of significant wave height. Individual storms are taken as portions of the time series with H_{m0} above 0.7 times the storm peak, H_{m0}.
2. The wave (or crest) height distribution is calculated for each sea state above the threshold in each individual storm. The short-term distribution of H (or C) conditional on H_{m0}, $P(h|H_{m0})$, is assumed to follow the empirical distributions by Forristall (see Section 13.3). The wave height probability distribution is then given by the following product over the n sea states making up the storm:

$$P(H_{\max} < h) = \prod_{j=1}^{n_{seastates}} P(h \mid H_{m0,j})^{N_{waves,j}} \tag{13.8}$$

with the number of waves in each sea state, N_{waves}, being estimated by deriving the mean zero-crossing period of the sea state. The most probable maximum wave height (or mode), H_{mp}, of the storm is given by:

$$P(H_{\max} < h) = \frac{1}{e} \tag{13.9}$$

This produces a database of historical storms each characterised by its most probable maximum individual wave height which is used for further extreme value analysis.

13.3.2 Convolution of short-term variability with long-term storm density

The long-term distribution of individual waves and crests is found by convolution of the long-term distribution of the modes (subscript $_{mp}$ for most probable value) with the distribution of the maximum conditional on the mode given by:

$$\begin{aligned} P(H_{\max}) &= \int_0^\infty P(h_{\max} \mid H_{mp}) \cdot p(H_{mp}) dH_{mp} \\ &= \int_0^\infty \exp\left(-\exp\left(-\ln N \left(\left(\frac{h}{H_{mp}} \right)^\beta - 1 \right) \right) \right) \cdot p(H_{mp}) dH_{mp} \end{aligned} \tag{13.10}$$

The value of N, which goes into this equation, is determined by defining equivalent storm properties for each individual storm. The equivalent storms have constant H_{m0} and a duration such that their probability density function of H_{max} or C_{max} matches that of the actual storm. The density functions of the maximum wave in the equivalent storms are given by:

$$p(H_{\max} \mid H_{m0,eq}, N_{eq}) = \frac{d}{dH} \left[1 - \exp\left(-\left(\frac{H_{\max}}{\alpha \cdot H_{m0,eq}} \right)^\beta \right) \right]^{N_{eq}} \tag{13.11}$$

The β parameter in eq. (13.10) comes from the short-term distribution of individual crests, eq. ((13.6), and is a function of wave height and wave period. Based on previous studies, it has been assessed that the maximum crest heights are not sensitive to β_C for a constant value of 1.88 and hence, it is decided to apply β_C = 1.88. The number of waves in a storm, N, was

conservatively calculated from a linear fit to the modes minus one standard deviation.

13.4 Subset extremes

Estimates of subset (e.g., directional, and monthly) extremes are required for several parameters. To establish these extremes, it is common practice to fit extreme value distributions to data sampled from the population (i.e., the model database) that fulfils the specific requirement e.g., to direction, i.e., the extremes from each direction are extracted and distributions fitted to each set of directional data in turn. By sampling an often relatively small number of values from the data set, each of these directional distributions is subject to uncertainty due to sampling error. This will often lead to the directional distributions being inconsistent with the omnidirectional distribution fitted to the maxima of the entire (omnidirectional) data set. Consistency between directional and omnidirectional distributions is ensured by requiring that the product of the n directional annual non-exceedance probabilities equals the omnidirectional, i.e.:

$$\prod_{i=1}^{n} F_i\left(x,\hat{\theta}_i\right)^{N_i} = F_{omni}\left(x,\hat{\theta}_{omni}\right)^{N_{omni}} \tag{13.12}$$

where N_i is the number of sea states or events for the i'th direction and $\hat{\theta}_i$, the estimated distribution parameter. This is ensured by estimating the distribution parameters for the individual distributions and then minimising the deviation:

$$\delta = \sum_{x_j}\left[-\ln\left(-N_{omni}\ln F_{omni}\left(x,\hat{\theta}_{omni}\right)\right) + \ln\left(-\sum_{i=1}^{n} N_i \ln F_i\left(x_j,\hat{\theta}_i\right)\right)\right]^2 \tag{13.13}$$

Here x_j are extreme values of the parameter for which the optimisation is carried out, i.e., the product of the directional non-exceedance probabilities is forced to match the omnidirectional for these values of the parameter in question.

The directional extremes presented in this report are given without scaling, that is, a T_{yr} event from direction it will be exceeded once every T years on the average. The same applies for monthly extremes. A T_{yr} monthly event corresponds to the event that is exceeded once (in that month) every T years, which is the same as saying that it is exceeded once every *T*/12 years (on average) of the climate for that month.

13.4.1 Optimised directional extremes

The directional extremes are derived from fits to each subseries data set meaning that a T_R year event from each direction will be exceeded once every T_R years on average. Having e.g., 12 directions, this means that **one** of the directions will be exceeded once every T_R/12 years on average. A 100-year event would thus be exceeded once every 100/12 = 8⅓ years (on average) from **one** of the directions.

For design application, it is often required that the summed (overall) return period (probability) is T_R years. A simple way of fulfilling this would be to take the return value corresponding to the return period T_R times the number of

directions, i.e., in this case the 12x100 = 1200-year event for each direction. However, this is often not optimal since it may lead to very high estimates for the strong sectors, while the weak sectors may still be insignificant.

Alternatively, an optimised set of directional extreme values may be produced for design purpose in addition to the individual values of directional extremes described above. The optimised values are derived by increasing (scaling) the individual T_R values of the directions to obtain a summed (overall) probability of T_R years while ensuring that the extreme values of the strong sector(s) become as close to the overall extreme value as possible. In practice, this is done by increasing the T_R of the weak directions more than that of the strong sectors but ensuring that the sum of the inverse directional T_R's equals the inverse of the targeted return period, i.e.:

$$\sum_{i=1}^{n} \frac{1}{T_{R,i}} = \frac{1}{T_{R,\text{omni}}} \tag{13.14}$$

where n is the number of directional sectors and $T_{R,omni}$ is the targeted overall return period.

13.5 Uncertainty assessment

The extreme values are estimated quantities and therefore all associated with uncertainty. The uncertainty arises from several sources:

Measurement/model uncertainty

The contents of the database for the extreme value analysis are associated with uncertainty. This type of uncertainty is preferably mitigated at the source – e.g., by correction of biased model data and removal of obvious outliers in data series. The model uncertainty can be quantified if simultaneous good quality measurements are available for a reasonably long overlapping period.

True extreme value distribution is unknown

The distribution of extremes is theoretically unknown for levels above the levels contained in the extreme value database. There is no justification for the assumption that a parametric extreme value distribution fitted to observed/modelled data can be extrapolated beyond the observed levels. However, it is common practice to do so, and this obviously is a source of uncertainty in the derived extreme value estimates. This uncertainty, increasing with decreasing occurrence probability of the event in question, is not quantifiable but the metocean expert may minimise it by using experience and knowledge when deciding on an appropriate extreme value analysis approach. Proper inclusion of other information than direct measurements and model results may also help to minimise this type of uncertainty.

Uncertainty due to sampling error

The number of observed/modelled extreme events is limited. This gives rise to sampling error which can be quantified by statistical methods such as Monte Carlo simulations or bootstrap resampling. The results of such an analysis are termed the confidence limits. The confidence limits (see Section 13.6) should **not** be mistaken for the total uncertainty in the extreme value estimate.

Settings of the analysis (judgement)

Any EVA involves the need to define the various settings of the analysis (threshold, distribution, and fitting method), which introduces subjectivity to the analysis. The sensitivity of these settings can be assessed by comparing the resulting extreme values, and the goodness of fit can, to some extent, be objectively assessed by statistical measures. However, standard practice typically includes manual inspection of the fitted distributions. Hence, the final settings, and thus results, relies on the experience and preference of the metocean expert conducting the analysis ('engineering judgement'). The tail of the distributions (the values of long the return periods) can be particularly sensitive to the settings of the analysis.

13.6 Confidence limits

The confidence limits of extreme estimates are established from a bootstrap analysis or a Monte Carlo simulation.

The bootstrap analysis estimates the uncertainty due to sampling error. The bootstrap consists of the following steps:

1. Construct a new set of extreme events by sampling randomly with replacement from the original data set of extremes
2. Carry out an extreme value analysis on the new set to estimate T-year events

An empirical distribution of the T-year event is obtained by looping steps 1 and 2 many times. The percentiles are read from the resulting distribution.

In the Monte Carlo simulation, the uncertainty is estimated by randomly generating many samples that have the same statistical distribution as the observed sample.

The Monte Carlo simulation can be summarised in the following steps:

1. Randomly generating a sample consisting of N data points, using the estimated parameters of the original distribution. If the event selection is based on a fixed number of events, N is set equal to the size of original data set of extremes. If the event selection is based on a fixed threshold, the sample size N is assumed to be Poisson-distributed.
2. From the generated sample, the parameters of the distribution are estimated, and the T-year return estimates are established.

Steps 1 and 2 are looped numerous times, whereby an empirical distribution of the T-year event is obtained. The quartiles are read from the resulting distribution.

13.7 Joint probability analyses (JPA)

Values of other parameters conditioned on extremes of one variable are estimated using the methodology proposed in [30] (Heffernan & Tawn). This method consists in modelling the marginal distribution of each variable separately. The variables are transformed from physical space, X, to standard Gumbel space by the relationship:

$$Y = \mathrm{LN}\left(-\mathrm{LN}\left(F\left(X, \hat{\theta}\right)\right)\right) \tag{13.15}$$

where $F(X, \hat{\theta})$ denotes the distribution function of the variable, X, with estimated parameters, $\hat{\theta}$. No restriction is given on the marginal model of the variables. A combination of the empirical distribution for the bulk of events and a parametric extreme value distribution function fitted to the extreme tail of data was adopted here. For parameters which may have both a positive and a negative extreme such as the water level conditioned on wave height, both the positive and the negative extreme tail are modelled parametrically.

The dependence structure of the two variables is modelled in standard Gumbel distribution space, conditioning one variable by the other. The model takes the form:

$$(Y_2|Y_1 = y_1) = ay_1 + y_1^b Z \tag{13.16}$$

with Y_1 being the conditioning variable and Y_2 the conditioned. The residual, Z, is assumed to converge to a normal distribution, G, with increasing y_1. The parameters, $\hat{a}$ and $\hat{b}$, are found from regression and the parameters, $\hat{\mu}$ and $\hat{\sigma}$, of the normal distribution, G, estimated from the residuals, Z:

$$Z = \frac{y_2 - a \cdot y_1}{y_1^b} \tag{13.17}$$

Figure 13.2 shows an example of the modelled dependence structure for H_{m0} and water level in standard Gumbel space. Figure 13.3 shows the same in physical space. The model is clearly capable of describing the positive association between wave heights and water level for this condition and appears also to capture the relatively large spreading.

The applied joint probability model is event-based. This means that independent events of the conditioning parameter are extracted from the model data. The combined inter-event time and inter-event level criterion described in Section 13.1 is applied to isolate independent events of the conditioning parameter. The conditioned parameter is extracted from the model time series at the point in time of the peak of the conditioning parameter. Time averaging of the conditioned parameter is often carried out prior to data extraction to reduce the influence of phases in the analysis (the fact that the water level may not peak at the same time as the peak wave height for instance).

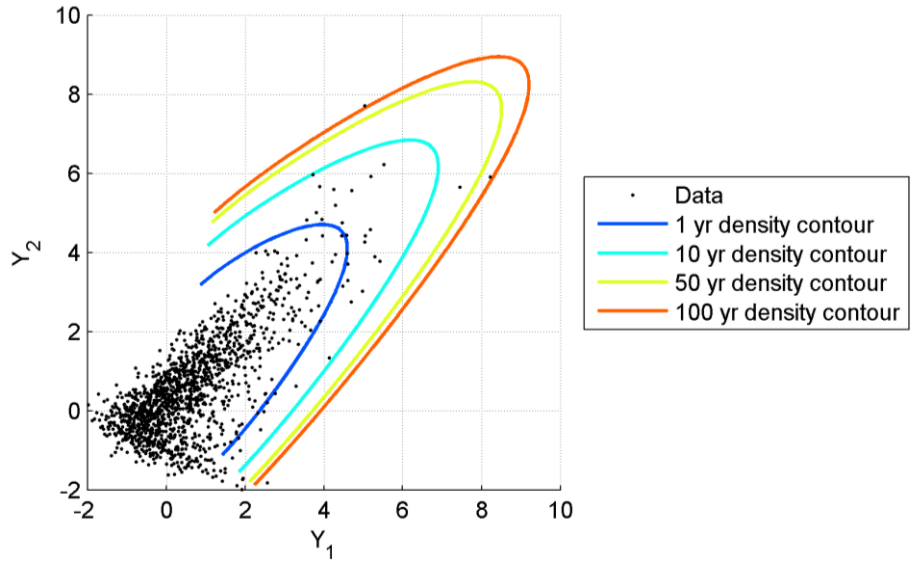

Figure 13.2 Dependence structure of H_{m0} and water level transformed into standard Gumbel space.

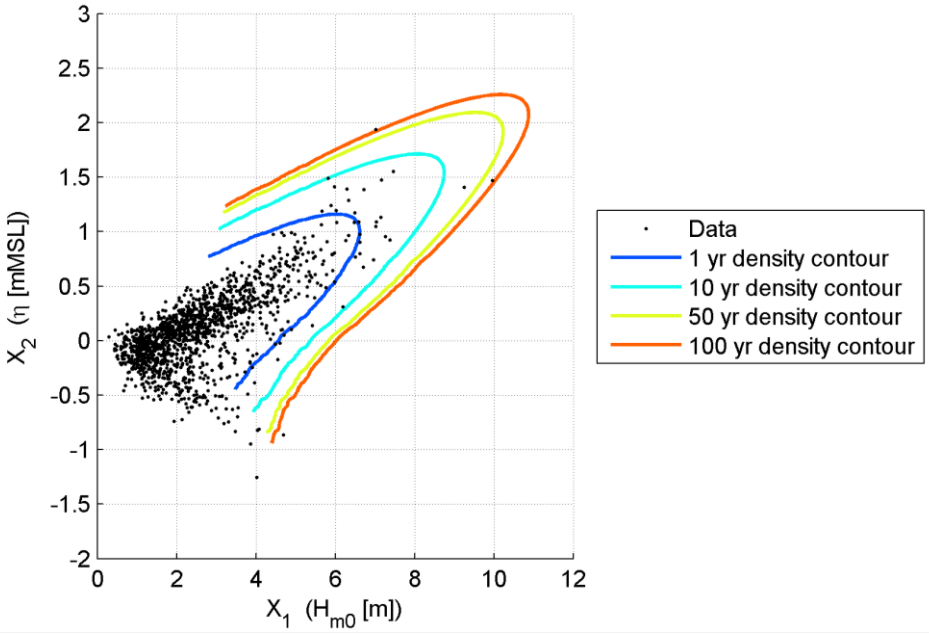

Figure 13.3 Dependence structure of H_{m0} and water level in physical space